Signatures de l'injection optique et électrique de charges dans des monocristaux de rubrene

Nripan Mathews

THESE DE DOCTORAT DE L'UNIVERSITE PARIS 6

Spécialité : **Chimie Moléculaire**

Présentée par
M. Nripan MATHEWS

Pour obtenir le grade de
DOCTEUR DE L'UNIVERSITE PARIS 6

Signatures of optically and electrically injected charges in rubrene single crystals

Soutenue le 19 septembre 2008

devant le jury composé de :

Dr Denis FICHOU	Directeur de thèse
Pr Max MALACRIA	Examinateur
Dr Dominique VUILLAUME	Rapporteur
Dr Alberto MORPURGO	Rapporteur
Pr Subodh MHAISALKAR	Examinateur
Pr Freddy BOEY	Examinateur

Thèse préparée au:
CEA Saclay, LRC Nanostructures et Semi-Conducteurs Organiques
CNRS-CEA-UPMC

Abstract

Organic single crystals are of particular fundamental interest as tools in probing the intrinsic electrical properties and the upper limit of performance for a given organic semiconducting molecule devoid of disorder. Rubrene single crystals are of particular interest in the field of organic electronics due to the high levels of charge carrier mobilities measured in transistors constructed of the same. In this thesis, we explore the properties of rubrene single crystal transistors.

The photocurrent properties of rubrene single crystals are measured in 'air-gap' transistors whose unique structure allows the measurement of photocarrier dynamics without the influence of a dielectric that can act as a source for traps. This structure has allowed us to identify phenomenon like persistent photoconductivity associated with the creation of oxygen related traps on the rubrene surface. Transient studies of the photocurrent reveal the presence of bimolecular recombination of the charge carriers. In addition, we have also performed optical spectroscopy studies including Raman spectra measurements which revealed the presence of endoperoxide related signature on the surface of the crystal while also confirming the low levels of intermolecular coupling present between the molecules.

We have also explored the extrinsic factors that determine the surface conductivity of the rubrene crystal, particularly the presence of oxide related compounds on the surface of the crystal using XPS and photoluminescence measurements. The impact of photo-oxidation of the rubrene crystal on the surface conductivities were evaluated by a novel experiment involving the gradual photo-oxidation of the rubrene surface using a focussed laser. The creation of a deep acceptor state that can trap electrons indicates that the electrical properties of the rubrene surface like high unipolar p-type

conductivity and photoconductivity may be modulated by the presence of these oxygen induced states.

Acknowledgements

The past three years spent in pursuing a PhD has taught me many valuable lessons and brought me in contact with many people who have been a pleasure to work with and who have affected my life in many ways. It is my great pleasure to acknowledge them here.

First of all, I would like to thank Dr Denis Fichou for having supervised my thesis at CEA-Saclay. Your perspective and knowledge of organic electronics, as well as your advice on how to manage research is greatly appreciated. I will remember your advice about always ‘putting things in the box’. I would also like to thank Prof Subodh Mhaisalkar for having co-supervised me. Your enthusiasm, ideas and energy during the past three years have been instrumental in ensuring the completion of this thesis. Your flexibility and patience was very helpful in trying to balance work between Singapore and France.

I also gratefully acknowledge the help and collaboration from Dr. Vitaly Podzorov and Dr. Etienne Menard. I am very thankful for the discussions and suggestions regarding my work. My gratitude also goes to Dr Tripathy and Mr Keke Zhang for help with the measurements for Raman spectra and gas sensing respectively.

My PhD journey would have been a lot harder if it was not for the support, help and sympathetic ears provided to me by my friends and colleagues in both France and Singapore. My heartfelt as well as ‘stomach felt’ appreciation go to Ludovic, Camille, Claudia, Odile, Alexandre, Giulia, Luc, Vadym, Vladymyr and Stephane. A special thank you also goes to Alexander Marchenko for his help during my time in France. Spending time in France has been a wonderful experience because of all you.

I am also grateful to all my friends in Singapore. At the polymer electronics group in Nanocluster, I would like to show gratitude to Wei Lin for being the sounding board for many of my ideas and for help with the experimentation, as well as Willy, Anup, Zong Bin, Tommy, Ju Nie, Phoebe, Vera and Victor. You all have been instrumental in creating a good fun filled environment to work in and for keeping my spirits high when things do not go well.

Last but definitely not the least; I would like to thank my family. I greatly acknowledge my parents who have supported me through all the decisions I have made and whose concern and love for me gives me hope and encouragement every day. Thank you my brother and sister-in-law for your patience and love as well.

Dedicated to my parents

Table of Contents

List of Figures

List of Tables

.

Chapter 1

General Introduction

The use of organic materials in electronics has been historically in the important role of photoresists that act as stencils in the lithography process for defining features on inorganic semiconductors like silicon and gallium arsenide or as encapsulates of the finished electronic devices. In the past decade or so, there has been a burst in research activities which explore the use of organic materials as the *active* component of the device. The interest in the field of organic electronics has been widely growing since the fabrication of the first field-effect transistors (FETs) based on polymer and small-molecule semiconductors [1-5]. The fabrication of the first all 'plastic' transistors were an important step in revealing the potential of organic electronics[6, 7].Other organic devices fabricated include light emitting diodes (OLEDs)[8-10], photovoltaic cells[11-13], waveguides[14] and organic lasers[15]. Organic transistors who are the workhorses of this field are especially interesting since they can serve as the main components in cheap and flexible electronic circuits with applications in displays, sensors and radio frequency identifications tags (RF-IDs) [16-29]. The main advantage of using organic semiconductors for electronics is their ability to be processed from solution at room temperatures making them ideal for low area, low cost, large volume manufacturing processes like printing as well as ink-jetting. Another important advantage of using organic materials is that their properties like ionization potential can be tailored by varying their molecular structure, either by changing the degree of conjugation in the polymer or by the introduction of electronically active substituents[30, 31].

In general, organic semiconductors consist of π conjugated structures which allows for delocalization of electrons along the length of the molecule. They are wide band gap

semiconductors with band gaps in the range of 2-3eV and can normally be classified into two families: polymers and small molecules. During the fabrication of active devices, small molecule organic semiconductors are thermally evaporated, forming a polycrystalline active layer whose properties are determined by surface treatment, temperature, material purity, as well as testing and deposition vacuum conditions[32-34].The changes caused in film growth and morphology like varying crystallinity, microstructure, molecular packing and alignment are manifested in the mobility values. Even for devices with the same organic active layer, reported results often vary over an order of magnitude. In addition to the inconsistency of basic performance parameters, variations in morphology and 'orientation averaging' will mask properties intrinsic to molecular arrangement, such as electrical anisotropy.

Crystals made of organic semiconductors play an important role in the study of the fundamental properties of the molecules[35-37]. Single crystals are a useful tool in probing the intrinsic electrical properties and perhaps the upper limit of performance for a given organic semiconducting molecule. In order to link molecular functionality and crystal microstructure to their optical and electrical properties, it is crucial that variation in both overall molecular order and device quality are minimized or eliminated. The use of a single crystal of organic material addresses this by providing near-perfect order over its entirety, which is often centimetres in size. In particular, they have developed from a tool useful for simply gauging the upper limit of thin-film performance into a powerful method for examining both device physics and the intrinsic transport properties of semiconductor materials. In addition, newly developed patterning techniques for single crystals – by both vapour and solution methods[38-40] – suggest that organic transistors based on single crystals may have potential as a viable method for hands-free circuit fabrication with the highest performance organic semiconductors available.

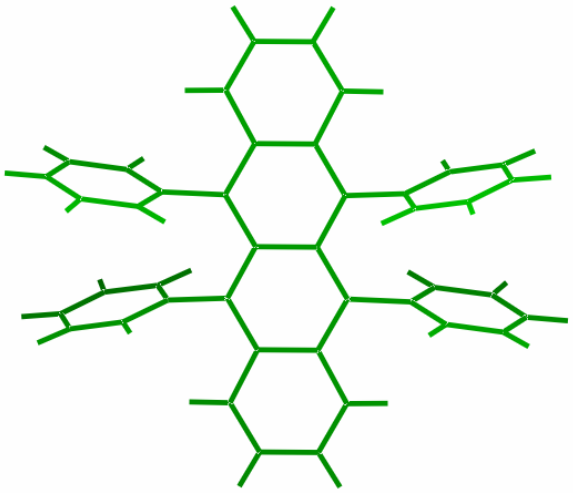

Figure 1.1: Molecular structure of rubrene showing the tetracene backbone and the four pendant phenyl rings in a twisted configuration

Among the various crystals prepared from small molecules, rubrene single crystals are of special interest. The rubrene molecule (5, 6, 11, 12-tetraphenyl tetracene) is a relatively small aromatic hydrocarbon consisting of a backbone of four fused benzene rings (tetracene) with four substituted phenyl rings as shown in Figure 1.1. Due to the bulky nature of the sidegroups, there is a large torsion angle [41]between the phenyl rings and the tetracene backbone in rubrene (85°), which strongly reduces any mixing of the molecular orbitals between the backbone and the side groups. This in turn implies that the HOMO and LUMO levels of the rubrene and tetracene molecules are similar[42]. Rubrene single crystals are of particular interest in the field of organic electronics due to the high hole mobilities recorded in this material[43]. The development of various fabrication techniques particularly the "air-gap" technique allows a non invasive study of the semiconductor crystal surface due to the absence of the semiconductor-dielectric interface[44]. Our group observed unipolar conduction of holes under illumination through scanning tunneling studies on the surface of rubrene crystals.

In this thesis, we report the characteristics of rubrene single crystal field-effect transistors (SCFETs) fabricated using the "air-gap" technique. In addition, we explore photocurrent measurements in the steady state and in the transient state in this conformation. The "air-gap" technique allows us to study the direct photocurrent response of the rubrene crystal transistors

without the influence of a dielectric. The source of the electronic properties of rubrene is explored by the characterization of the single crystal by photoluminescence as well as by Raman scattering measurements. Finally, extrinsic factors that influence the surface conductivity of rubrene single crystals are explored.

1.1 Thesis overview

The following chapter introduces the reader to the various concepts regarding organic semiconductors and molecular crystals. The electronic properties of the crystals will be explored including the influence of the molecular structure and the intermolecular interactions. The charge transport characteristics of molecular crystals are explored and concepts relating to band like transport and polaron transport are introduced.

Chapter 3 deals with the fabrication and electrical characteristics of free-space dielectric transistors as well as the details of the physical vapor transport growth process of the organic crystals. The general principles behind the working of a field effect transistor are described as well. Contact effects and their dependence on the apparent mobility values measured in the transistors are briefly explored through temperature dependent measurements.

The steady-state and transient photocurrents measured in rubrene crystals in the transistor configuration are described in Chapter 4. The steady state measurements have revealed oxygen induced trap states on the surface of the rubrene crystal as evidenced by the observation of persistent photoconductivity in these samples. Transient photocurrents on the other hand has shown bimolecular recombination of the induced charge carriers which can be modulated by increased carrier densities induced by optical power as well as gate electric field.

Chapter 5 delves in to the various optical and vibrational characterizations performed on the rubrene crystal in order to explain the electrical properties of rubrene crystal. Raman

measurements on the surface of the crystal have not been able to detect intermolecular coupling, but may have revealed the presence of rubrene peroxide on the surface.

Finally chapter 6 explores the extrinsic factors influencing surface conductivities of rubrene crystals. This chapter details the various experiments performed to detect the presence of rubrene endoperoxide on the surface of the crystal as well as its influence on the charge transport properties of the rubrene crystal surface.

1.3 References

1. F. Ebisawa, T. Kurokawa and S. Nara, *Journal of Applied Physics*, 1983, **54**, 3255-3259.
2. A. Tsumura, H. Koezuka and T. Ando, *Applied Physics Letters*, 1986, **49**, 1210-1212.
3. A. Assadi, C. Svensson, M. Willander and O. Ingana?s, *Applied Physics Letters*, 1988, **53**, 195-197.
4. K. Kudo, M. Yamashina and T. Moriizumi, *Jpn. J. Appl. Phys.*, 1984, **23**, 130-130.
5. G. Horowitz, D. Fichou, X. Peng, Z. Xu and F. Garnier, *Solid State Communications*, 1989, **72**, 381-384.
6. F. Garnier, G. Horowitz, X. Peng and D. Fichou, *Advanced Materials*, 1990, **2**, 592-594.
7. X. Peng, G. Horowitz, D. Fichou and F. Garnier, *Applied Physics Letters*, 1990, **57**, 2013-2015.
8. T. W. Kelley, P. F. Baude, C. Gerlach, D. E. Ender, D. Muyres, M. A. Haase, D. E. Vogel and S. D. Theiss, *Chemistry of Materials*, 2004, **16**, 4413-4422.
9. L. S. Hung and C. H. Chen, *Materials Science and Engineering R: Reports*, 2002, **39**.
10. B. W. D'Andrade and S. R. Forrest, *Advanced Materials*, 2004, **16**, 1585-1595.
11. P. Peumans, A. Yakimov and S. R. Forrest, *Journal of Applied Physics*, 2003, **93**, 3693-3723.
12. C. W. Tang, *Applied Physics Letters*, 1986, **48**, 183-185.
13. G. Yu, J. Gao, J. C. Hummelen, F. Wudl and A. J. Heeger, *Science*, 1995, **270**, 1789-1791.
14. W. Geis, R. Sinta, W. Mowers, S. J. Deneault, M. F. Marchant, K. E. Krohn, S. J. Spector, D. R. Calawa and T. M. Lyszczarz, *Applied Physics Letters*, 2004, **84**, 3729-3731.
15. M. A. Baldo, R. J. Holmes and S. R. Forrest, *Physical Review B - Condensed Matter and Materials Physics*, 2002, **66**, 353211-3532116.
16. H. Klauk, D. J. Gundlach, J. A. Nichols and T. N. Jackson, *IEEE Transactions on Electron Devices*, 1999, **46**, 1258-1263.
17. J. A. Rogers, Z. Bao, K. Baldwin, A. Dodabalapur, B. Crone, V. R. Raju, V. Kuck, H. Katz, K. Amundson, J. Ewing and P. Drzaic, *Proceedings of the National Academy of Sciences of the United States of America*, 2001, **98**, 4835-4840.

18. H. Sirringhaus, T. Kawase and R. H. Friend, *MRS Bulletin*, 2001, **26**, 539-543.
19. C. D. Dimitrakopoulos and P. R. L. Malenfant, *Advanced Materials*, 2002, **14**, 99-117.
20. H. E. A. Huitema, G. H. Gelinck, J. B. P. H. Van Der Putten, K. E. Kuijk, C. M. Hart, E. Cantatore and D. M. De Leeuw, *Advanced Materials*, 2002, **14**.
21. P. F. Baude, D. A. Ender, M. A. Haase, T. W. Kelley, D. V. Muyres and S. D. Theiss, *Applied Physics Letters*, 2003, **82**, 3964-3966.
22. M. Kitamura, T. Imada and Y. Arakawa, *Japanese Journal of Applied Physics, Part 1: Regular Papers and Short Notes and Review Papers*, 2003, **42**, 2483-2487.
23. G. H. Gelinck, H. E. A. Huitema, E. V. Veenendaal, E. Cantatore, L. Schrijnemakers, J. B. P. H. Van Der Putten, T. C. T. Geuns, M. Beenhakkers, J. B. Giesbers, B. H. Huisman, E. J. Meijer, E. M. Benito, F. J. Touwslager, A. W. Marsman, B. J. E. Van Rens and D. M. De Leeuw, *Nature Materials*, 2004, **3**, 106-110.
24. V. Subramanian, P. C. Chang, J. B. Lee, S. E. Molesa and S. K. Volkman, *IEEE Transactions on Components and Packaging Technologies*, 2005, **28**, 742-747.
25. L. Torsi and A. Dodabalapur, *Analytical Chemistry*, 2005, **77**.
26. S. Lee, B. Koo, J. G. Park, H. Moon, J. Hahn and J. M. Kim, *MRS Bulletin*, 2006, **31**, 455-459.
27. M. Muccini, *Nature Materials*, 2006, **5**, 605-613.
28. R. Rotzoll, S. Mohapatra, V. Olariu, R. Wenz, M. Grigas, K. Dimmler, O. Shchekin and A. Dodabalapur, *Appl. Phys. Lett*, 2006, **88**, 123502.
29. L. S. Zhou, A. Wanga, S. C. Wu, J. Sun, S. Park and T. N. Jackson, *Appl. Phys. Lett*, 2006, **88**, 083502.
30. G. Padmanaban and S. Ramakrishnan, *Journal of the American Chemical Society*, 2000, **122**, 2244-2251.
31. P. F. Van Hutten, V. V. Krasnikov and G. Hadziioannou, *Accounts of Chemical Research*, 1999, **32**, 257-265.
32. Z. T. Zhu, J. T. Mason, R. Dieckmann and G. G. Malliaras, *Applied Physics Letters*, 2002, **81**, 4643-4645.
33. M. M. Ling and Z. Bao, *Chemistry of Materials*, 2004, **16**, 4824-4840.
34. D. Li, E. J. Borkent, R. Nortrup, H. Moon, H. Katz and Z. Bao, *Applied Physics Letters*, 2005, **86**.
35. M. Pope and C. E. Swenberg, *Electronic Processes in Organic Crystals and Polymers*, 2nd edn., Oxford University Press, New York, 1999.

36. C. Reese and Z. Bao, *Materials Today*, 2007, **10**, 20-27.

37. E. A. Silinsh, *Organic Molecular Crystals: their Electronic States*, 1st edn., Springer-Verlag, Berlin, 1980.

38. A. L. Briseno, J. Aizenberg, Y. J. Han, R. A. Penkala, H. Moon, A. J. Lovinger, C. Kloc and Z. Bao, *Journal of the American Chemical Society*, 2005, **127**, 12164-12165.

39. A. L. Briseno, S. C. B. Mannsfeld, M. M. Ling, S. Liu, R. J. Tseng, C. Reese, M. E. Roberts, Y. Yang, F. Wudl and Z. Bao, *Nature*, 2006, **444**, 913-917.

40. A. L. Briseno, R. J. Tseng, M. M. Ling, E. H. L. Falcao, Y. Yang, F. Wudl and Z. Bao, *Advanced Materials*, 2006, **18**, 2320-2324.

41. I. Bulgarovskaya, V. Vozzhennikov, S. Aleksandrov and V. Belsky, *Latv. PSR Zinat. Akad. Vestis, Khim. Ser.*, 1983, 53.

42. D. A. Da Silva Filho, E. G. Kim and J. L. Bre?das, *Advanced Materials*, 2005, **17**, 1072-1076.

43. V. Podzorov, E. Menard, A. Borissov, V. Kiryukhin, J. A. Rogers and M. E. Gershenson, *Physical Review Letters*, 2004, **93**, 086602-086601-086602-086604.

44. E. Menard, V. Podzorov, S. H. Hur, A. Gaur, M. E. Gershenson and J. A. Rogers, *Advanced Materials*, 2004, **16**, 2097-2101.

Chapter 2

Electronic properties of molecular crystals

Organic semiconductor molecules can be broadly classified into two families: polymers and small molecules. Polymeric molecules typically have high molecular weights and are relatively easy to process from solution and are present as amorphous or partially crystalline in the solid-state. Among the many polymers in this category, thiophene based polymers are notable for their higher electrical performance. Polymers like, Poly (3-hexylthiophene) (P3HT)[1-5] , polyquarterthiophenes (PQT)[6] , poly(9,9-dioctylfluorene-co-bithiophene) (F8T2)[7] and poly(2,5-bis(3-alkylthiophen-2-yl)thieno[3,2-b]thiophenes) (PTTT) [8]fall into this category of compounds.

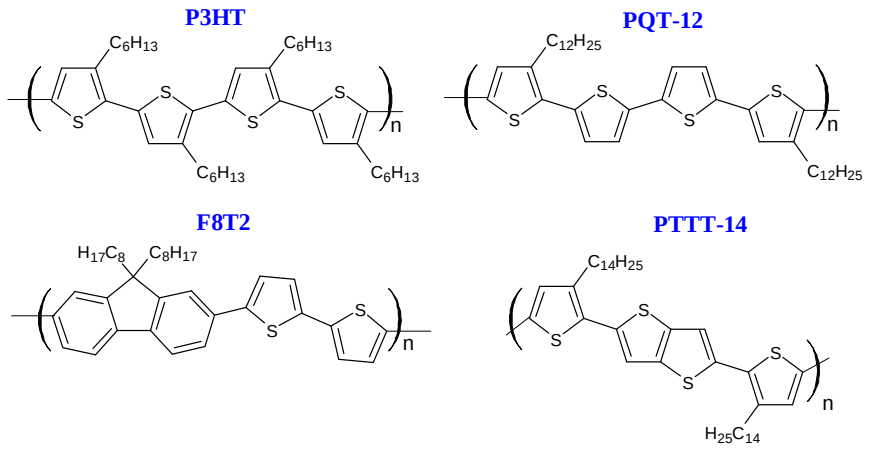

Figure 2.1: Chemical structure of some widely used semiconducting organic polymers

Small molecules on the other hand have low molecular weights and are normally deposited by thermal evaporation. They normally consist of acenes like pentacene, tetracene, anthracene[9-17] as well as oligomers like quarterthiophene, sexithiophene[18-22].

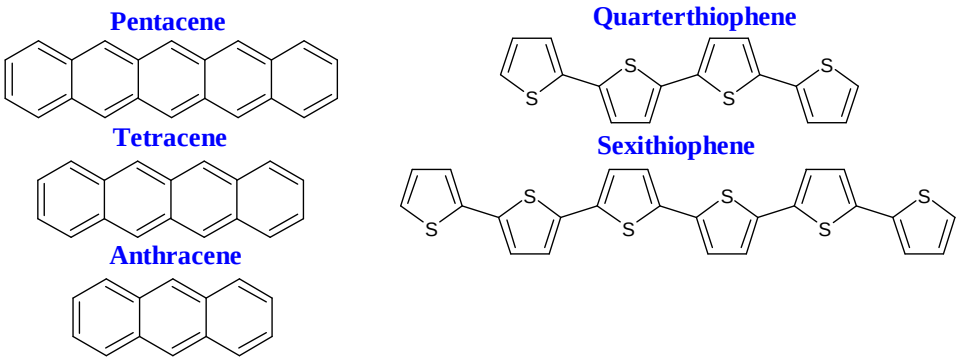

Figure 2.2: Chemical structure of some well known small molecule semiconductors

The charge transport properties of the molecules and polymers mentioned above are determined by the individual energy levels of these molecules as well as the level of interaction between them which is mediated by intermolecular distances and the extent of the electron cloud overlap. Sections 2.1 and 2.2 introduce the molecular and intermolecular determinants of charge conducting behaviour in organic devices.

2.1 Organic semiconducting molecules

In order to discuss the electrical properties of these semiconducting molecules, it is appropriate to first focus on the building blocks of these organic molecules-the carbon atoms. The carbon atom in the ground state has six electrons in which four of them are valence electrons with the atomic configuration $1s^2 2s^2 2p^2$. The orbitals of these electrons may mix, under creation of four chemical bonds, to form four equivalent degenerate orbitals referred to as sp^3 hybrid orbitals in a tetrahedral orientation around the carbon atom like in diamond. In saturated polymers, the valence electrons of the carbon atom are hybridized in the sp^3 configuration and every carbon is bonded to four neighbouring atoms and therefore the orbitals are fully saturated[23]. This is the case of polyethylene in which carbon is σ bonded to two neighbouring carbon atoms and two hydrogen atoms. Conjugated polymers on the other hand differ from saturated polymers in that each carbon in the main chain is bonded to only three other atoms. The orbitals are sp^2 hybridized and three electrons from each carbon atom

reside in the three σ-bonding orbitals, forming covalent bonds with the other atoms. The remaining unpaired electron remains in the delocalized $2p_z$ orbital with its charge density lobes perpendicular to the plane defined by the σ-bonds. These p_z orbitals can then overlap to form delocalized π bands which make the conjugated polymers metals or semiconductors depending on whether the bands are filled or partially filled.

The π-electrons are delocalized over several carbon atoms in the polymeric chain to form π-bands. The presence of an energy gap between the filled and empty bands imparts a semiconducting nature to the polymer instead of a metallic one. The delocalized π-electrons are primarily responsible for the electrical and optical properties in these systems. Equivalently the π bonding and antibonding orbitals can be visualized to form a continuum of energy states rather than a discreet one. The resultant continuum of antibonding and bonding orbitals are referred to as lowest unoccupied molecular orbital (LUMO) and highest occupied molecular orbital (HOMO) respectively. The HOMO and LUMO with an energy gap between them is analogous to the valence and conduction bands in any inorganic semiconductor.

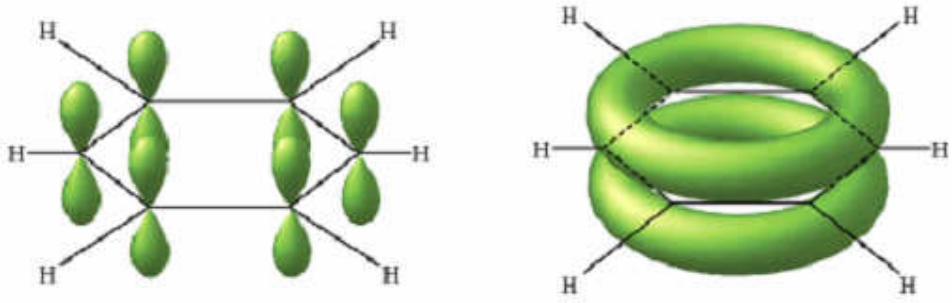

Figure 2.3: Creation of delocalized π electron system in a benzene molecule-the building block of the acene group

In the case of small molecule semiconductors like acenes with the benzene ring as the basic unit, the π bonds become delocalized and form a π system that extends throughout the system (Figure 2.3). The gap between occupied and unoccupied states in this π system becomes lesser with increased delocalization in the system. Thus

pentacene with its 5 aromatic rings acts a semiconductor, while benzene remains an electrical insulator (Figure 2.4). Charge carriers can easily move along a conjugated molecule because of the presence of the delocalised molecular orbitals. For example, in oligomers with well defined chain lengths, it has been shown that the primary gap excitations are delocalized over the entire molecule and that the corresponding excitons scale with the length of the molecule[24]. In contrast, the charge carriers move with greater difficulty between different molecules due to the fact that conjugated semiconductors in their thin film form are disordered materials with a low degree of crystallinity.

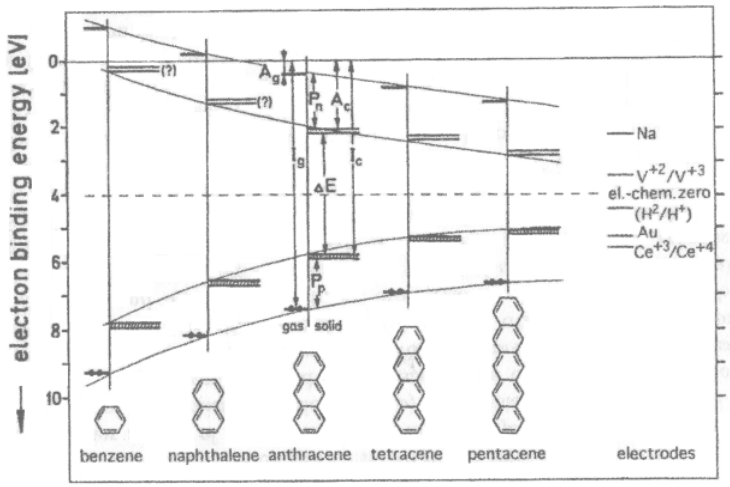

Figure 2.4: Energy levels of (single) ionic states of the acenes from benzene to pentacene for the free molecule in the gas (g) state (*left,* solid lines), and for the crystal (c) (*right,* double lines), defined by the electron-binding energy relative to the vacuum level. I_g and I_c stand for ionization energies for gas phase and crystalline phase, A_g and A_c for electron affinities for gas and solid phases, P_e and P_h for electron and hole polarization energies respectively.

2.2 Intermolecular interaction

Efficient charge transport requires that the charges be able to move from molecule to molecule and not be trapped or scattered. Thus charge carrier mobilities are influenced by many factors including molecular packing, disorder and the presence of impurities. In molecular crystals, the molecules are held together in a lattice by weak forces. These forces (primarily van der Waals interaction) are much weaker than the

intramolecular covalent bonds such that the molecular properties are hardly affected by the intermolecular interactions. The weakness of the intermolecular forces in molecular crystals is expressed in the low mechanical strengths of these crystals as well as their propensity to form polymorphs. For example in pentacene, four polymorphs have been detected by Mattheus et al[25-27], all of which are layered herringbone structures. These polymorphs can have different charge transport properties caused due to the difference in the bandwidths of the conduction and valence bands.[28]

The van der Waals force comes from the interaction of a fluctuating dipole moment on a molecule, induced by the electron motion within the molecule, with the induced dipole moment on a neighbouring molecule. In aromatic and heterocyclic molecular crystals, the weakly bound and therefore easily polarisable π electrons provide van der Waals interactions. The van der Waals force of interaction favours face to face orientation of planar molecules in the lattice in order to maximise the interaction energy. This co facial structure is not commonly seen in most organic crystals due to the contribution of quadrupole-quadrupole interactions in π conjugated systems[29, 30].

Due to the delocalization of the π electrons above and below the plane of the molecule and the net positive charge in the plane of the molecule, the molecule resembles two dipoles oriented head to head. This results in a quadrupolar field around the molecule that provides a considerable share of the total intermolecular interaction. The repulsion induced by the quadrupolar interaction is strongest in a co facial arrangement due to the repulsion induced by the closest approaching π electron clouds. Thus the interplay between the van der Waals forces and quadrupolar interaction results determines the final order. Desiraju et al.[31] defined four possible packing types for polynuclear aromatic hydrocarbons : herringbone structure (naphthalene, anthracene, tetracene[32], pentacene[33] and rubrene[34, 35]), sandwich herringbone structure (pyrene, perylene), γ structure (benzopyrene, coronene) and β structure (trybenzopy-

rene, tetrabenzoperylene). Important work by Anthony et al[28, 36] has shown that the different types of packing are possible by varying the nature, size and position of substituent groups on the pentacene backbone. Similar variations have been illustrated in chloro and bromo substituted tetracene[12] derivatives where the stacking structure which enhances the π orbital overlap between the molecules (as compared to the herringbone motif) results in an enhanced charge carrier mobility.

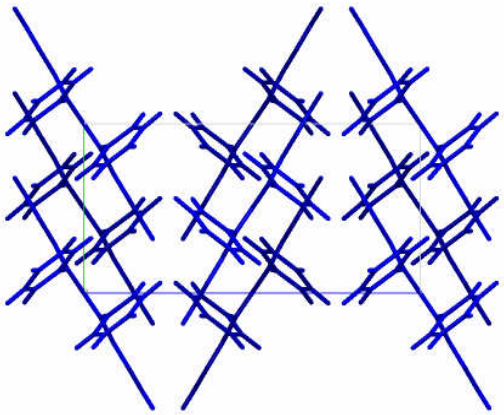

Figure 2.5: A top view of the ab- plane crystal structure of rubrene. The herringbone configuration is apparent.

Locally, charge transport in conjugated materials is determined by the charge transfer from one neighbouring molecule to another and is therefore very sensitive to orientation of the molecules with respect to each other. The electronic coupling between adjacent molecules, quantified by the transfer integral t, is modulated by the molecular arrangement and directly associated with the electronic mobility [37-39]. In the framework of these calculations, the amplitude of the electronic coupling is influenced by the intermolecular separation distance, the molecular overlap, the length of the molecule, and, in the case of herringbone structures, the rotation of molecular planes[38, 40-43].Thus transfer integrals between the adjacent molecules in these crystals vary significantly depending on the crystallographic direction[39, 41, 44]. One apparent implication is that the charge carrier mobility within a molecular plane (ab plane in

rubrene) is much more efficient in comparison to charge carrier transport between layers (c direction). This strong anisotropy of transport properties of organic crystals has been well documented in the TOF experiments[45]. The conductivity anisotropy within the ab-plane is anticipated to be less pronounced. However, prior to the development of single-crystal OFETs, the anisotropy had never been observed in the field-induced transport on the surface of organic semiconductors. Several types of single-crystal OFETs based on rubrene demonstrate anisotropy of surface conductivity [46-48] . In rubrene devices based on PDMS stamps, the mobility along the crystallographic ***b*** axis exceeds the mobility along the ***a*** axis by a factor of ~ 3 (Figure 2.6). Similar anisotropies have been observed for rubrene transistors with parylene gate dielectrics as well. A clear correlation between the mobility and molecular packing has also been found recently in a family of tetrathiafulvalene derivatives[49] and in air-gap transistors built on tetracene crystals[50]. Recently, non-destructive probing techniques have been developed that allow the exploration of these anisotropies at high angular resolution without having to move the fragile crystals around.[51]

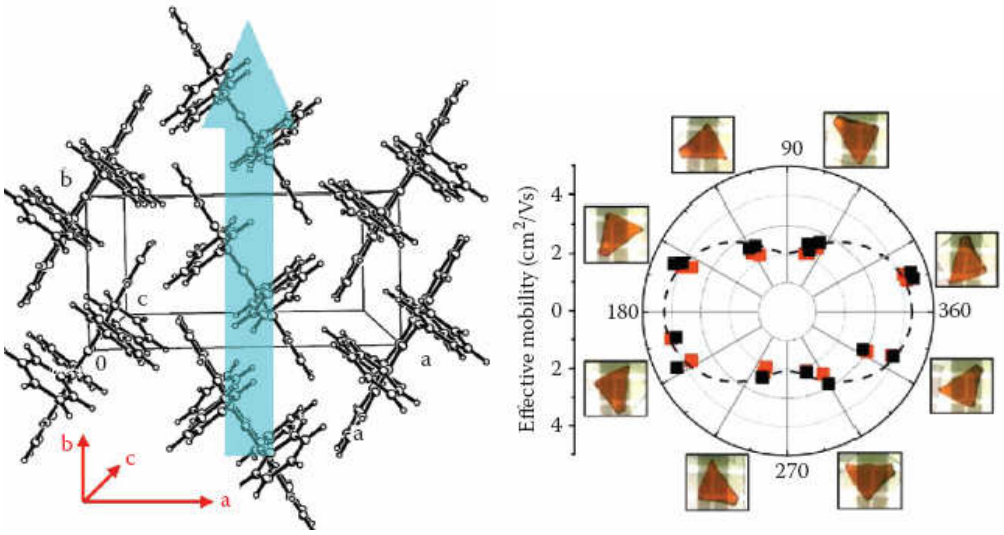

Figure 2.6: (Left) Molecular packing in the rubrene crystal. Blue arrow indicates the direction of highest mobility (Right) Charge carrier mobility anisotropy on the surface of rubrene crystal[46]

2.3 Charge transport characteristics of organic single crystals

Due to the weak van der Waals bonding between the individual organic molecules, many electronic properties of these organic solids are determined by the property of the molecule itself- specifically the energy gap between the highest occupied and lowest occupied molecular orbitals (HOMO and LUMO). The transport mechanism is usually understood with respect to the limiting cases of small polaron transport and bandlike transport corresponding to the extreme localization or delocalization of the charge carriers.

2.3.1 Band like transport

The classical work performed by N. Karl and coworkers on highly purified naphthalene and perylene single crystals revealed the first proof of band transport in organic molecular crystals[52-54].Mobilities as high as 400 cm^2/Vs were obtained at 10K and 3kV/cm by the time-of –flight method (Figure 2.7) in extremely pure naphthalene crystals. These TOF velocities could not be explained by charge hopping models.

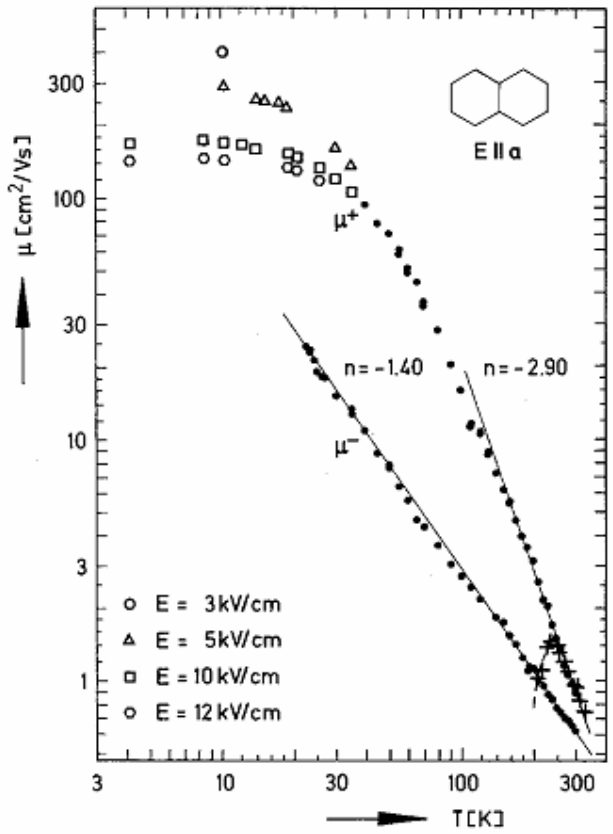

Figure 2.7: Electron and hole mobilities in the a-direction of highly purified naphthalene crystals for different field strengths. Adapted from [53]

In addition, the sub-linear velocity-field relation at high fields observed in these samples could be explained by the Schottky model of acoustic deformation potential scattering by hot charge carriers, a model which is based on band transport. Thus the authors[53] proposed that the charge carrier transport in pure and perfect low molecular weight aromatic organic photoconductor crystals at low temperature can be described by coherent transport in bands. Space charge limited current measurements on ultrapure pentacene [55] as well as in tetracene [56] single crystals have shown intrinsic band like transport. Picosecond transient photoconductivity measurements conducted on a variety of organic crystals including rubrene support the band picture as well [57-59].

It is conceivable that in organic crystals where the molecules are in an ordered arrangement, each molecular π system can interact with the π systems of the adjacent

molecules resulting in the formation of energy bands in the crystal. The crystal valence bands originate from the overlapping HOMO's of the individual molecules, whereas the conduction band is formed by the overlapping of the LUMOs. The organic semiconductors are normally characterized by wide bandgaps and small bandwidths. The molecular crystal's bandwidth is related to the orbital overlap strength of the HOMOs and the LUMOs. Calculations have shown that the bandwidths are in the range of 0.1 -0.5 eV [60-62]. This compares unfavourably with the values in inorganic semiconductors like silicon (10 eV) and could explain the huge difference in the mobilities.

2.3.2 Influence of traps

Since organic crystals possess a better crystalline order and reduced concentration of defects, they are expected to have a very low concentration of electrical traps. The reduced number of defects still creates localized electrical states in the HOMO-LUMO gap. The impact of these traps on the electrical transport properties depends on their location in the energy gap. In the case of p-type carriers, if the traps exist near the edge of HOMO, separated by energy of a few k_BT, they act as shallow traps. If the energy of the localized state is separated from the mobility edge by more than a few k_BT, they are characterized as deep traps. Once a charge is trapped in a deep state, it cannot be released by thermal energy alone. For the pristine surface of rubrene single crystals at room temperature, for instance, the density of deep traps can be as low as 10^{10} cm^{-2}.Shallow traps on the other hand are characterized by a finite trapping time. After being trapped for a characteristic time τ_{tr}, a polaron can be thermally activated and released to the band. The effect of shallow traps on charge transport is normally described in terms of the multiple trap and release (MTR)[63, 64] model. According to this model, not all the charges induced in the transistor on application of a voltage V_G above the threshold voltage V_{th} contributes to the current. A fraction of the mobile charge can be momentarily trapped by shallow traps-the fraction being determined by

the number of traps and the temperature (which determines the τ_{tr}). This idea can be represented in two ways- either by assuming that all the carriers induced above the threshold flow, but with a lower effective mobility than the intrinsic mobility or by assuming that the number of carriers moving at any time is limited, but they travel at the intrinsic trap free mobility. The first approach can be described by:

$$\mu_{eff} = \mu_0(T)\frac{\tau(T)}{\tau(T)+\tau_{tr}(T)}$$

Here $\tau_{tr}(T)$ is the average trapping time on shallow traps while $\tau(T)$ is the average time that a polaron spends diffusively travelling between the consecutive trapping events. Thus the intrinsic mobility is only realised when the τ is much more than τ_{tr} which happens when there is a low concentration of defects or when the temperature is high enough to ensure rapid detrapping. This regime allows the exploration of the intrinsic properties of the crystal surface like mobility anisotropy.

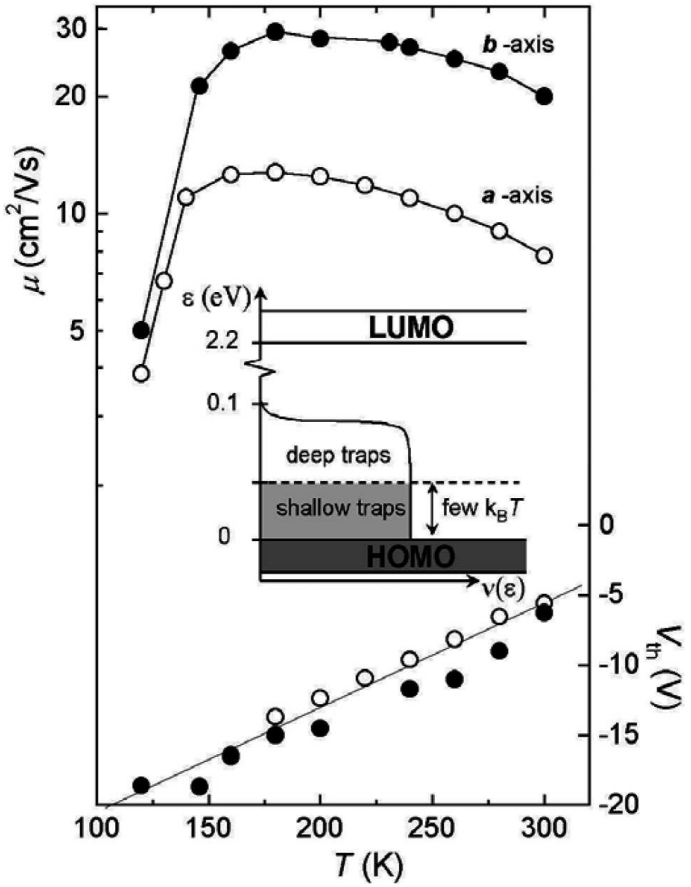

Figure 2.8: Temperature dependent conductivity measurements on the rubrene transistor showing the trap limited regime at low temperatures and intrinsic regime at higher temperatures

Figure 2.8 reveals the two regimes at play in the temperature dependent characteristics of rubrene single crystal transistors. At higher temperatures (above 150K), the intrinsic properties like the pronounced anisotropy difference for conductivity along the b-axis and the a-axis. As the temperature is lowered, the charges localized in the shallow traps are released after a much longer timescale. This is indicated by the rapid fall in mobility values below 150K where the traps dominate. This transition temperature would be strongly dependent on the concentration of the traps with a higher concentration shifting this threshold to a higher temperature. The classical work performed by N.Karl and co-workers on ultrapure crystals of naphthalene and perylene revealed similar results with an increase in the mobility (up to 400 cm^2/Vs)

with the lowering of temperature (intrinsic regime) until the shallow traps become active and result in a reduction of the effective mobility.[47, 53]

The high-quality TOF data of Karl et al implies that coherent transport characterizes the intrinsic charge transport in ultra-pure organic single crystals. However the calculation of the charge carrier's mean free path from experimental evidence indicates that they are smaller than the intermolecular distance[62]. This of course violates the assumption of charge delocalization necessary for the band model. In narrow-band molecular solids, polarization effects favor localization of charge carriers and narrow the bandwidth even further. This results in self-trapped electronic states called polarons which differ in their behavior from nearly free electrons (necessary for band-type behavior) and strongly localized electrons (which can lead to hopping behavior). The next section discusses polaron formation and transport

2.3.3 Polaron transport

Polarons are quasiparticles composed of a charge carrier accompanying its polarization field. The polarization field causes a distortion in the local lattice. As the charge moves through the crystal, the electron carries the lattice distortion with it. The resulting lattice polarization acts as a potential well that hinders the movements of the charge, thus decreasing the mobility. In an organic molecular crystal, the polarization associated with the charge include the polarization of the electronic orbitals on molecules surrounding the excess charge which is caused due to the interaction of the charge with the induced dipole moments and quadrupole moments of the surrounding molecules.

The term of polaron owes its origin to that it was considered for the case of polar crystals, where interactions between electrons and optical polarizations are

particularly strong, so that an excess carrier creates a local distortion of the lattice in which it is self-trapped. The indications for polaron-formation in organic molecular crystals can be seen in photo-emission experiments.[62] Photoemission data from single crystals generally show lines that are broadened and shifted in energy relative to the corresponding gas phase spectral lines. The broadening is suggested to originate from fluctuations in the intermolecular electronic polarization while the spectral line shift can be explained by the increased binding energy of a charge due to polarizations in the local crystal environment. Pioneering theoretical work in this area was done by Holstein[65], who introduced the concept of small-polaron bands for a local (on-site) electron –phonon coupling. A small polaron is one whose linear dimensions are of the order of one lattice spacing. The main prediction of his theory is that the mobilities initially decrease with rising temperature T due to bandwidth narrowing but increase again for higher T due to phonon-assisted hopping.

Interestingly electron mobility values of naphthalene single crystals below 100K follows a power law (proportional to $T^{-1.5}$) consistent with the band model. However, between 100K and 300K the electron mobility along the crystallographic c direction remains constant [45]. This constant region has been described as the superposition of two independent carrier mechanisms. According to Silinsh et al[66] the first mechanism is described using the concept of an adiabatic, nearly small molecular polaron (MP),in which the carriers are treated as heavy polaron-type quasiparticles, which are formed as a result of the interaction of the carriers with intramolecular vibrations of the local lattice environment, and move coherently via tunneling. The second mechanism involves a small lattice polaron (LP), which moves by thermally activated hopping and thus exhibits a typical exponential dependence of mobility on temperature. This polaronic hopping-type temperature dependence has also been measured for the electron mobility in pyrene and for the hole mobility in perylene[45]. Kenkre et al[67] were also able to fit the measured electron mobilities reasonably well to Holstein's model assuming directionally dependent local-coupling constants.

Despite the success of such fitting procedures, there was a need for a first-principles description of charge-carrier mobilities in organic crystals that could explain the different behavior of electrons and holes, the microscopic origin of the crystallographic anisotropy in the temperature dependence and the influence of nonlocal (Peierls-type) couplings. This has been compensated by the proposal of a Holstein-Peierls model by Hannewald et al[68, 69] which is based on Holstein's original concept of small-polaron bands but generalized with respect to the inclusion of nonlocal electron-phonon coupling. Using this model and microscopic parameters derived from ab-initio calculations, the authors were able to reproduce the experimental data in naphthalene[69]. The model, however, only accounts for the intermolecular optical modes and neglects the contribution from intra-molecular vibrations and the coupling to acoustic modes that play a significant role in charge transport.[70]

The polaron theories described above are mostly applicable to charge conduction in the bulk of the crystal for a low density of charge carriers (as is the case in TOF experiments). On the surface of rubrene single crystal transistors where the density of charge carriers is much higher due to its proximity to a polar dielectric, conduction has been proposed to occur through the motion of Fröhlich polarons[71] In common inorganic semiconductors, the effective strength of the interactions that create Fröhlich polarons are weak due to both the low ionic polarizabilities and the low band masses of these materials. This is not the case in organic transistors where the band masses are high due to the weak van der Waals bonding while using gate dielectrics with increasing ionic polarizabilities permits the strength of interaction to be tuned from weak to the strong coupling regimes.

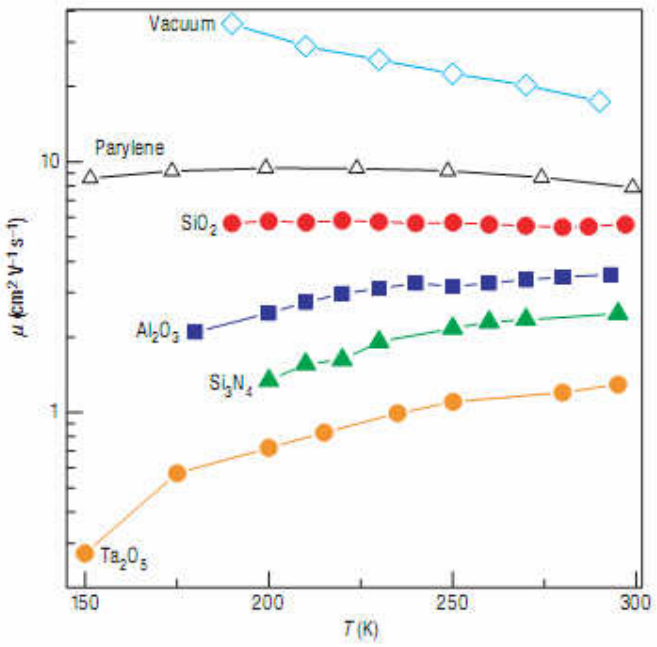

Figure 2.9: Temperature dependence of the carrier mobility for six different gate dielectrics. The temperature dependence evolves from metallic-like to insulator-like, as the dielectric constant is increased.

The gate modulated electrostatic 'doping' of charge carriers in organic single crystal transistors allows the observation and study of new phenomena. For example, the use of highly polarizable Ta_2O_5 gate dielectrics allows a high carrier density regime (0.1 carrier per molecule) which enables observation of coulombic repulsion in the Fröhlich polarons and drain current saturation in transistors.[72]

Recently, Troisi [73]et al have proposed in a recent computational paper that, at room temperature, the transfer integral between close molecules is strongly modulated by thermal motions. Since the amplitude of this modulation is of the same order of magnitude as the average transfer integral, the translational symmetry of the electronic Hamiltonian is completely lost and the overall electronic structure of the crystal resembles that of an amorphous material. The sensitivity of the transfer integral to small nuclear displacements (discussed previously in this chapter) was recognized by these authors as the crucial difference between transport mechanisms in

organic and inorganic semiconductors. A minimalist model Hamiltonian[37] that neglects the effect of reorganization energy and considers only the fluctuation of the transfer integral has been used to explain the temperature dependence of the charge mobility of organic semiconductors and has been applied to predict the absolute charge mobility of rubrene.[74]

In conclusion, this chapter has discussed the basic theory of charge transport in organic crystals including the origin of semiconducting behaviour in organic molecules. The intermolecular interactions that shape the order and arrangement of organic molecules in lattices have been described. The position and orientation of the molecules modulate the intermolecular transfer integral which determines the charge transfer properties of these molecules. The band model which is commonly used to discuss the charge transport in single crystals was also introduced here along with the characteristics of polaron transport in these materials. The widespread interest in unraveling the underlying factors determining the charge transport is spurring the development of new theories which consider local and non-local interactions between the charge carrier and its environment.

2.4 References

1. A. Assadi, C. Svensson, M. Willander and O. Ingana?s, *Applied Physics Letters*, 1988, **53**, 195-197.
2. Z. Bao, A. Dodabalapur and A. J. Lovinger, *Applied Physics Letters*, 1996, **69**, 4108-4110.
3. R. J. Kline, M. D. McGehee, E. N. Kadnikova, J. Liu, J. M. J. Fre?chet and M. F. Toney, *Macromolecules*, 2005, **38**, 3312-3319.
4. J. Paloheimo, H. Stubb, P. Yli-Lahti and P. Kuivalainen, *Synthetic Metals*, 1991, **41**, 563-566.
5. A. Tsumura, H. Koezuka and T. Ando, *Applied Physics Letters*, 1986, **49**, 1210-1212.
6. B. S. Ong, Y. Wu, P. Liu and S. Gardner, *Journal of the American Chemical Society*, 2004, **126**, 3378-3379.
7. E. Lim, Y. M. I. Kim, J. I. K. Lee, B. J. Jung, N. S. Cho, J. Lee, D. O. Lee-Mi and H. K. Shim, *Journal of Polymer Science, Part A: Polymer Chemistry*, 2006, **44**, 4709-4721.
8. H. Sirringhaus, R. J. Wilson, R. H. Friend, M. Inbasekaran, W. Wu, E. P. Woo, M. Grell and D. D. C. Bradley, *Applied Physics Letters*, 2000, **77**, 406-408.
9. J. G. Laquindanum, H. E. Katz, A. J. Lovinger and A. Dodabalapur, *Chemistry of Materials*, 1996, **8**, 2542-2544.
10. Y. Y. Lin, D. J. Gundlach and T. N. Jackson, Annual Device Research Conference Digest, 1996.
11. Y. Y. Lin, D. J. Gundlach, S. F. Nelson and T. N. Jackson, *IEEE Electron Device Letters*, 1997, **18**, 606-608.
12. H. Moon, R. Zeis, E. J. Borkent, C. Besnard, A. J. Lovinger, T. Siegrist, C. Kloc and Z. Bao, *Journal of the American Chemical Society*, 2004, **126**, 15322-15323.
13. M. L. Tang, A. D. Reichardt, N. Miyaki, R. M. Stoltenberg and Z. Bao, *Journal of the American Chemical Society*, 2008, **130**, 6064-6065.
14. C. D. Dimitrakopoulos, A. R. Brown and A. Pomp, *Journal of Applied Physics*, 1996, **80**, 2501-2508.
15. C. D. Dimitrakopoulos, S. Purushothaman, J. Kymissis, A. Callegari and J. M. Shaw, *Science*, 1999, **283**, 822-824.

16. H. Klauk, M. Halik, U. Zschieschang, G. Schmid, W. Radlik and W. Weber, *Journal of Applied Physics*, 2002, **92**, 5259.
17. S. F. Nelson, Y. Y. Lin, D. J. Gundlach and T. N. Jackson, *Applied Physics Letters*, 1998, **72**, 1854-1856.
18. F. Garnier, G. Horowitz and D. Fichou, *Synthetic Metals*, 1989, **28**, 705-714.
19. F. Garnier, G. Horowitz, D. Fichou and A. Yassar, *Synthetic Metals*, 1996, **81**, 163-171.
20. F. Garnier, G. Horowitz, X. Peng and D. Fichou, *Advanced Materials*, 1990, **2**, 592-594.
21. F. Garnier, G. Horowitz, X. Z. Peng and D. Fichou, *Synthetic Metals*, 1991, **45**, 163-171.
22. G. Horowitz, D. Fichou, X. Peng, Z. Xu and F. Garnier, *Solid State Communications*, 1989, **72**, 381-384.
23. J. March, *Advanced Organic Chemistry*, John Wiley & Sons, New York, 1985.
24. M. Knupfer, J. Fink, E. Zojer, G. Leising and D. Fichou, *Chemical Physics Letters*, 2000, **318**, 585-589.
25. C. C. Mattheus, A. B. Dros, J. Baas, A. Meetsma, J. L. De Boer and T. T. M. Palstra, *Acta Crystallographica Section C: Crystal Structure Communications*, 2001, **57**, 939-941.
26. C. C. Mattheus, G. A. De Wijs, R. A. De Groot and T. T. M. Palstra, *Journal of the American Chemical Society*, 2003, **125**, 6323-6330.
27. C. C. Mattheus, A. B. Dros, J. Baas, G. T. Oostergetel, A. Meetsma, J. L. De Boer and T. T. M. Palstra, *Synthetic Metals*, 2003, **138**, 475-481.
28. R. C. Haddon, X. Chi, M. E. Itkis, J. E. Anthony, D. L. Eaton, T. Siegrist, C. C. Mattheus and T. T. M. Palstra, *Journal of Physical Chemistry B*, 2002, **106**, 8288-8292.
29. M. D. Curtis, J. Cao and J. W. Kampf, *J. Am. Chem. Soc.*, 2004, **126**, 4318-4328.
30. C. A. Hunter and J. K. M. Sanders, *Journal of the American Chemical Society*, 1990, **112**, 5525-5534.
31. G. R. Desiraju and A. Gavezzotti, *Journal of the Chemical Society, Chemical Communications*, 1989, 621-623.
32. A. M. Pivovar, J. E. Curtis, J. B. Leao, R. J. Chesterfield and C. D. Frisbie, *Chemical Physics*, 2006, **325**, 138-151.

33. R. B. Campbell, J. M. Robertson and J. Trotter, *Acta Crystallogr.*, 1962, **15**, 289-290.

34. O. D. Jurchescu, A. Meetsma and T. T. M. Palstra, *Acta Crystallographica Section B*, 2006, **62**, 330-334.

35. D. E. Henn, W. G. Williams and D. J. Gibbons, *Journal of Applied Crystallography*, 1971, **4**, 256.

36. J. E. Anthony, D. L. Eaton and S. R. Parkin, *Organic Letters*, 2002, **4**, 15-18.

37. A. Troisi and G. Orlandi, *Physical Review Letters*, 2006, **96**, 086601-086604.

38. J. Cornil, D. Beljonne, J. P. Calbert and J. L. Bre?das, *Advanced Materials*, 2001, **13**, 1053-1067.

39. Y. C. Cheng, R. J. Silbey, D. A. Da Silva Filho, J. P. Calbert, J. Cornil and J. L. Bre'das, *Journal of Chemical Physics*, 2003, **118**, 3764.

40. J. L. Bre'das, D. Beljonne, V. Coropceanu and J. Cornil, *Chemical Reviews*, 2004, **104**, 4971-5003.

41. J. L. Bre'das, J. P. Calbert, D. A. Da Silva Filho and J. Cornil, *Proceedings of the National Academy of Sciences of the United States of America*, 2002, **99**, 5804-5809.

42. O. Kwon, V. Coropceanu, N. E. Gruhn, J. C. Durivage, J. G. Laquindanum, H. E. Katz, J. Cornil and J. L. Bre?das, *Journal of Chemical Physics*, 2004, **120**, 8186-8194.

43. V. Lemaur, D. A. Da Silva Filho, V. Coropceanu, M. Lehmann, Y. Geerts, J. Piris, M. G. Debije, A. M. Van De Craats, K. Senthilkumar, L. D. A. Siebbeles, J. M. Warman, J. L. Bre?das and J. Cornil, *Journal of the American Chemical Society*, 2004, **126**, 3271-3279.

44. G. A. De Wijs, C. C. Mattheus, R. A. De Groot and T. T. M. Palstra, *Synthetic Metals*, 2003, **139**, 109.

45. N. Karl, in *Organic electronic materials*, eds. R. Farchioni and G. Grosso, Springer-Verlag, Berlin, Editon edn., 2001.

46. V. C. Sundar, J. Zaumseil, V. Podzorov, E. Menard, R. L. Willett, T. Someya, M. E. Gershenson and J. A. Rogers, *Science*, 2004, **303**, 1644.

47. V. Podzorov, E. Menard, A. Borissov, V. Kiryukhin, J. A. Rogers and M. E. Gershenson, *Physical Review Letters*, 2004, **93**, 086602.

48. R. Zeis, C. Besnard, T. Siegrist, C. Schlockermann, X. Chi and C. Kloc, *Chemistry of Materials*, 2006, **18**, 244.

49. M. Mas-Torrent, P. Hadley, S. T. Bromley, X. Ribas, J. Tarre?s, M. Mas, E. Molins, J. Veciana and C. Rovira, *Journal of the American Chemical Society*, 2004, **126**, 8546.
50. X. Yu, V. Kalihari, C. D. Frisbie, N. K. Oh and J. A. Rogers, *Applied Physics Letters*, 2007, **90**, 162106.
51. M. M. Ling, C. Reese, A. L. Briseno and Z. Bao, *Synthetic Metals*, 2007, **157**, 257.
52. N. Karl, J. Marktanner, R. Stehle and W. Warta, *Synthetic Metals*, 1991, **42**, 2473-2481.
53. W. Warta, R. Stehle and N. Karl, *Applied Physics A Solids and Surfaces*, 1985, **36**, 163.
54. W. Warta and N. Karl, *Physical Review B*, 1985, **32**, 1172-1182.
55. O. D. Jurchescu, J. Baas and T. T. M. Palstra, *Applied Physics Letters*, 2004, **84**, 3061-3063.
56. R. W. I. de Boer, M. Jochemsen, T. M. Klapwijk, A. F. Morpurgo, J. Niemax, A. K. Tripathi and J. Pflaum, *Journal of Applied Physics*, 2004, **95**, 1196-1202.
57. V. K. Thorsmolle, R. D. Averitt, X. Chi, D. J. Hilton, D. L. Smith, A. P. Ramirez and A. J. Taylor, *Applied Physics Letters*, 2004, **84**, 891-893.
58. O. Ostroverkhova, D. G. Cooke, S. Shcherbyna, R. F. Egerton, F. A. Hegmann, R. R. Tykwinski and J. E. Anthony, *Physical Review B - Condensed Matter and Materials Physics*, 2005, **71**, 1-6.
59. O. Ostroverkhova, D. G. Cooke, F. A. Hegmann, J. E. Anthony, V. Podzorov, M. E. Gershenson, O. D. Jurchescu and T. T. M. Palstra, *Applied Physics Letters*, 2006, **88**, 162101-162103.
60. G. Brocks, J. van den Brink and A. F. Morpurgo, *Physical Review Letters*, 2004, **93**, 146405.
61. R. Silbey, J. Jortner, S. A. Rice and J. M. T. Vala, *The Journal of Chemical Physics*, 1965, **42**, 733-737.
62. M. Pope and C. E. Swenberg, *Electronic Processes in Organic Crystals and Polymers*, 1999.
63. G. Horowitz, *Journal of Materials Research*, 2004, **19**, 1946.
64. G. Horowitz and M. E. Hajlaoui, *Advanced Materials*, 2000, **12**, 1046.
65. T. Holstein, *Annals of Physics*, 1959, **8**, 343.

66. E. A. Silinsh, A. Klimkans, S. Larsson and V. Cápek, *Chemical Physics*, 1995, **198**, 311-331.

67. V. M. Kenkre, J. D. Andersen, D. H. Dunlap and C. B. Duke, *Physical Review Letters*, 1989, **62**, 1165-1168.

68. K. Hannewald, V. M. Stojanovic, J. M. T. Schellekens, P. A. Bobbert, G. Kresse and J. Hafner, *Physical Review B - Condensed Matter and Materials Physics*, 2004, **69**, 752111-752117.

69. K. Hannewald and P. A. Bobbert, *Applied Physics Letters*, 2004, **85**, 1535-1537.

70. V. Coropceanu, J. Cornil, D. A. da Silva Filho, Y. Olivier, R. Silbey and J. L. Brédas, *Chemical Reviews*, 2007, **107**, 926-952.

71. I. N. Hulea, S. Fratini, H. Xie, C. L. Mulder, N. N. Iossad, G. Rastelli, S. Ciuchi and A. F. Morpurgo, *Nature Materials*, 2006, **5**, 982-986.

72. S. Fratini, H. Xie, I. N. Hulea, S. Ciuchi and A. F. Morpurgo, *New Journal of Physics*, 2008, **10**, 033031.

73. A. Troisi and G. Orlandi, *Journal of Physical Chemistry A*, 2006, **110**, 4065-4070.

74. A. Troisi, *Advanced Materials*, 2007, **19**, 2000-2004.

Chapter 3

Free-space dielectric field effect transistors

This chapter introduces the various fabrication techniques used in the construction of organic single crystal transistors with a strong emphasis on free-space dielectric field effect transistors. This was the configuration employed throughout the construction and testing of rubrene single crystal transistors described in this thesis. General characteristics of organic single crystal field effect transistors are described as well as the influence of contacts on electrical characteristics extracted from the transistors.

Molecular crystals are of importance in the field of organic electronics due to the opportunity that they allow for the exploration of fundamental properties without the influence of disorder. Molecular crystals due to their rigid order and tendency to form two dimensional crystallites are normally very fragile and difficult to handle. The purity of the crystals makes it very sensitive to defects and contamination introduced while fabricating devices. Traditionally, anthracene has been studied as a model organic semiconductor and photoconductor with initial work on anthracene crystals going as far back as 1906 [1]. The development of efficient purification methods[2, 3] allowed the exploration of fundamental properties of anthracene such as its intrinsic energy levels and its charge carrier transport properties[4, 5]. Since the explorations of the properties of these molecules are possible only in high quality crystals, it is relevant to begin the chapter with a brief discussion on the techniques used to prepare the crystals.

3.1 Single crystal growth

The most common way of growing organic crystals is in horizontal reactors in the vapor phase in a stream of transport gas. In this Physical Vapor Transport (PVT) method, the starting material is placed on the hottest region of the reactor and the crystal is grown on the colder parts of the reactor. Heavy impurities (with a vapor pressure lower than that of the pure organic compound) remain at the position of the source material. Light impurities (with a vapor pressure higher than that of the pure organic compound) condense at a lower temperature, i.e. at a different position from where the crystals grow. Therefore, the crystal growth process also results in the purification of the material. The characteristics of the crystal depends on the carrier transport gas used (Argon is best for tetracene while hydrogen is best for rubrene) although the mechanism is not clear. Good crystal growth involves very careful tuning of parameters and precautions to prevent the creation of photoinduced oxidation defects. Details of the physical vapour transport process have been described exhaustively by a series of papers by Laudise and Kloc[6, 7].

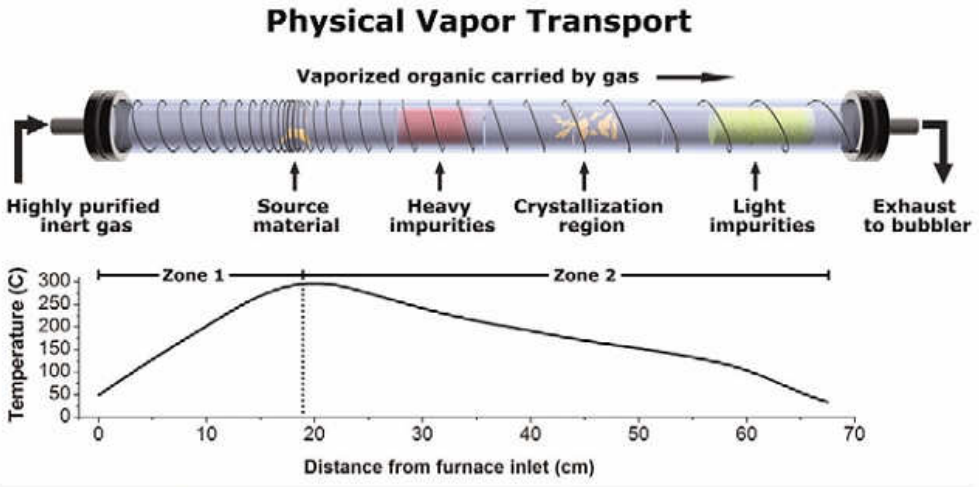

Figure 3.1: Schematic of the PVT crystal growth apparatus[8]

Starting material is loaded into the source zone and maintained at a temperature T_{source}, where sublimation takes place, and molecules are carried by the gas stream into the region of lower temperature. For a given concentration of evaporated molecules, defined by the temperature T_{source}, there is a point located downstream at a lower temperature, growth, where crystallization occurs. At this point, the crystallization rate (proportional to the density of molecular vapor) becomes slightly greater than the rate of sublimation from crystal facets kept at temperature T_{crys}. Although both crystallization and sublimation occur at a facet simultaneously, the growth is favoured and free-standing crystals grow. In the region to the left of the growth zone, sublimation prevails and no growth occurs; in the region to the right (downstream), the density of molecular vapor decreases and crystallization also does not occur. In this region, only smaller molecular weight impurities condense. If the temperature of the starting material is kept very close to the sublimation point, the heavier molecular impurities do not sublime and remain in the source zone. Thus crystal growth by PVT results in purification at the same time.

The crystals which are obtained after the PVT process (conducted over several tens of hours) are normally in the form of platelets or needles. The crystal shape is controlled by the anisotropy of intermolecular interactions: For many materials, the largest crystal dimension corresponds to the direction of the strongest interactions and, presumably, the strongest overlap of π-orbitals of adjacent molecules. For this reason, the direction of the fastest growth of elongated rubrene crystals (***b*** axis) coincides with the direction of the highest mobility of field-induced carriers. In platelet-like crystals, the largest natural facet typically corresponds to the ***a–b*** plane.

In some molecular crystals (eg. Anthracene), impurities have been shown to strongly influence the electrical as well as the optical properties. This is similar to the case of inorganic semiconductors like silicon where the impurity levels are kept below the ppm range. Tetracene in ppm traces form shallow electron and hole traps at room

temperature in anthracene single crystals. Introduction of an impurity with a smaller ionization energy and/or larger electron affinity than the host molecules will form trap levels in the energy gaps between the transport levels. Additional effects can also be caused due to the excess strain induced by the inclusion of the impurity in the matrix. This highlights the importance of starting the growth with pure organic powder. This especially becomes important in the case of higher melting point hydrocarbons where purification methods like zone-melting are not feasible [2]. The rubrene crystals used in this thesis have been prepared by Dr. Vitaly Podzorov at the Rutgers University using hydrogen as a carrier gas. As the crystal growth process also results in the chemical purification of the material, several re-growth cycles may be required for improving the field-effect mobility, with the grown crystals used as the starting materials for the subsequent regrowth.

3.2 Organic single crystal transistors

Broadly, single crystal transistors can be classified in two categories- top contact and bottom contact. The top-contact SCFET configuration involves the fabrication of a transistor structure directly on top of the organic single crystal and is at most times a top-gate structure with the semiconductor crystal acting as the substrate. This architecture requires that source and drain electrodes and dielectric are deposited onto the surface of the single crystal. This is a very critical step in the fabrication of the transistor. The commonly used methods include the application of conducting paste and Ag epoxy [9, 10]or direct shadow mask deposition[11] onto the crystal surface. While each of these methods is relatively straightforward and has been employed successfully, both have been implicated in the formation of defects at the critical semiconductor/electrode interface. During the application of the silver paste, the solvents in the mixture will attack the surface of the organic crystal. Another disadvantage of the manual application of electrodes is the difficulty in preparing small and well shaped contacts. The direct deposition of electrodes on top of the

crystal also results in damage due to the kinetic energy of the hot gold atoms arriving from the source.

In addition, the manual application of electrodes and the limitation of shadow-mask feature sizes necessitate large crystals and limits device density. Another critical step is the deposition of a dielectric layer on top of the crystal which has proven even more problematic. Attempts at sputtering Al_2O_3 and other dielectrics on the crystal resulted in a very high density of traps and a prohibitively high field-effect threshold[12]. This problem has been addressed with the introduction of a conformal evaporated parylene dielectric film [11]. With a very simple homemade reactor, an inert, pinhole-free, conformal film can be controllably deposited onto the crystal surface without apparently damaging it. A gate electrode deposited on this film completes the top-contact, top-gate structure. Introduced by Podzorov et al., the technique has resulted in high mobility being recorded in a variety of organic crystals and has been instrumental in the investigation of intrinsic properties of the rubrene single crystal [13-17].

The bottom-contact SCFETs take advantage of photolithography to pattern source and drain electrodes as well as the dielectric on a substrate containing a gate electrode on to which the crystal is placed or grown. The use of photolithography allows for the patterning of features at length scales and densities impossible with top-contact geometries. The 'electrostatic bonding' technique, in which a thin single crystal adheres to the dielectric surface by simply being brought into contact, has been performed on thermally grown SiO_2 substrates [18-23] as well as other high k-dielectrics deposited through sputtering.

3.2.1 Elastomeric transistor stamps

The elastomeric technique developed by E. Menard et al also involved the prefabrication of source/drain/ gate electrodes on a flexible elastomeric substrate. The elastomeric technique, however, compares favorably with the Si-based technique in two important aspects. Firstly, in contrast to Si-based substrates that require very thin (~1 µm) and bendable crystals (which are prone to strain-induced defects), the elastomeric stamps are compatible with much thicker (up to a few mm) and rigid crystals: the flexible elastomeric surface and the ductile Au contacts adjust easily to the crystal shape. Secondly, the elastomeric stamp technique is non-destructive and reversible: the contact between the stamp and organic crystals can be re-established many times without affecting the transistor characteristics. This experimental capability was used to explore the dependence of the field effect mobility on the orientation of the transistor channel relative to the crystallographic axes, and observed for the first time a strong anisotropy of the field-effect mobility within the a-b plane of single crystals of rubrene[8, 24] (Chapter 2, Figure 2.6).

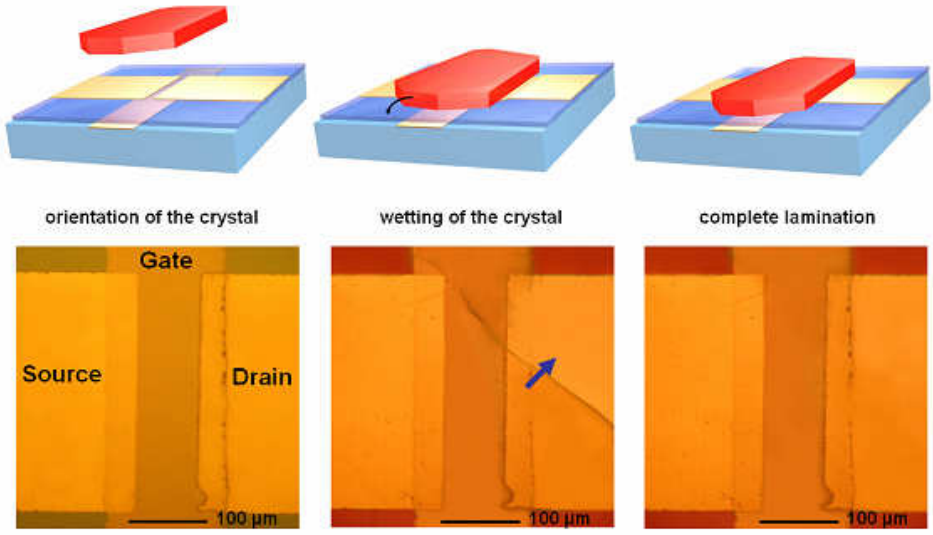

Figure 3.2: Transistor fabrication by lamination of an organic crystal against the transistor stamp. Initiating contact between the two surfaces results in a wetting front that progresses across the semiconductor-stamp interface until the entire crystal is in intimate contact with the stamp[24]

3.3 Air-gap stamps

As mentioned previously, organic field effect transistors (OFETs) that facilitate studies on the electrical characteristics of organic semiconductors are complex structures whose properties depend on interactions between the semiconductor, gate dielectric and electrodes. Carrier trapping, charge doping, molecular reorientation, dipole formation and a range of possible chemical interactions are among the many phenomena that can occur at the semiconductor/dielectric interface to degrade device performance. [10, 11, 25-27].

E. Menard et al[28] proposed an unusual device design that avoids these effects entirely by replacing the standard solid dielectric layer with a thin free space gap that can be filled with air, nitrogen, other gases or even vacuum. When combined with high-quality organic crystals, this design reveals the ultimate in OFET performance, determined solely by the intrinsic (not limited by disorder) polaronic transport on the pristine surface of the crystals. Unlike the effects associated with electrical contacts, which can be subtracted from the device response by four point probing or channel length scaling analysis, it is difficult or impossible to predict or account for interactions between a semiconductor and a conventional material dielectric[23, 29]. The free space dielectric simply eliminates these effects by eliminating the dielectric insulating material. It is uniquely well suited to the study of organic semiconductors, which do not possess the types of dangling bonds or surface states that are present in many inorganic materials. The advantages of this technique were demonstrated in the construction of TCNQ single crystal transistors with high intrinsic carrier mobilities of 1.6 cm^2/Vs.[28] It must be noted that transistors which were constructed using the elastomeric stamp technique as well as with parylene as the dielectric showed much lower mobilities.

3.3.1 Fabrication of air-gap stamps

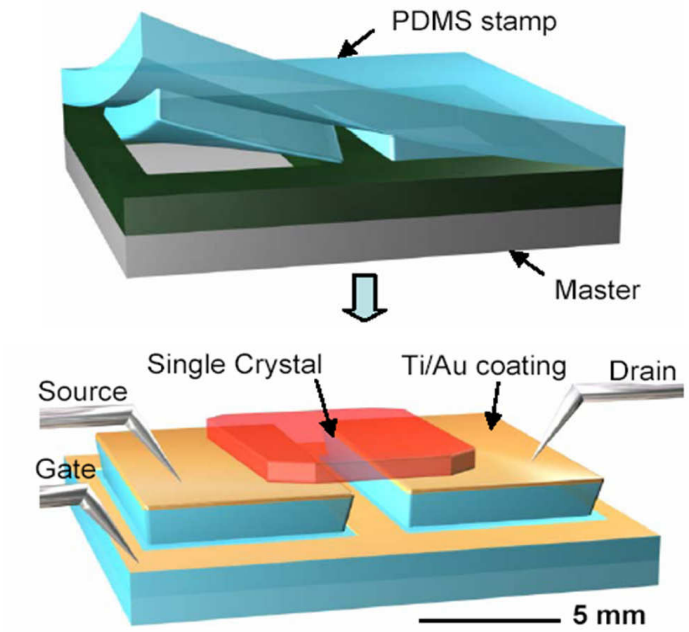

Figure 3.3: Schematic illustration of the construction of organic single crystal transistors with free space gate dielectrics.

Figure 3.3 schematically illustrates the steps for building these devices. The stamp is fabricated by casting a pre-polymer of poly (dimethylsiloxane) (PDMS; Sylgard 184, Dow Corning Corp.) against a pattern of photoresist (SU8) on a silicon wafer defines an elastomeric element with relief features in the geometry of the resist. The PDMS can also be casted on top of a master with relief features. The casted feature is left in low vacuum to degas the mixture of PDMS and curing agent. After heating, the PDMS hardens and can be carefully removed from the pattern. Coating this element with a collimated flux of metal generates electrically isolated electrodes on the raised and recessed regions. This single processing step defines source and drain (raised regions) electrodes together with a self-aligned gate (recessed region) electrode. The size of the electrodes and their separation are limited only by the resolution of soft lithographic casting and curing procedures: dimensions as small as a few tens of nanometers are possible[30].

Gently placing a single crystal sample on the surface of such an element leads to soft, van der Waals contacts to the source/drain electrodes. The crystal itself forms a free standing bridge that spans the gap between these electrodes. The thin space between the bottom surface of the crystal and the gate electrode plays the role of the gate dielectric. This space can be filled with any gas (e.g. air) or by vacuum, depending on the experimental conditions. The standard spacing between the crystal and gate electrodes of the stamps utilized in this thesis is 2 microns. The electrical breakdown fields for air gaps which are much narrower than the mean free path of air molecule can be exceptionally high due to the suppression of the avalanche phenomena that generate discharges.[31]

3.4 Working principle of field effect transistors

The basic idea of a field effect transistor is to modulate the current that flows between two ohmic contacts (source and drain electrodes) by applying a voltage to a third contact (the gate electrode). The semiconductor film and the gate electrode are capacitively coupled such that the application of a bias on the gate induces charge in the semiconductor film. The inorganic Metal Insulator Field Effect Transistor (MISFETs) normally operate in the inversion mode where the electric field applied at the gate electrode is enough to induce minority carriers at the semiconductor-dielectric interface. In the case of organic materials with the low density of charge carriers, the preferred regime of operation is in the accumulation mode.

For a transistor based on a p-type semiconductor, the accumulation regime is induced on the application of a sufficiently high negative gate voltage. The application of a negative bias causes the HOMO and LUMO levels to shift up such that the HOMO becomes resonant with the Fermi energy level of the contact. This allows the

injection of holes from the contacts (or spilling of electrons from the semiconductor to the contacts). The injected holes can then move under the application of an applied drain electric field. In the case of an n-type transistor, the application of a positive gate voltage results in the HOMO and LUMO levels shifting down so that the LUMO levels align with the Fermi level of the electrode, allowing injection of electrons into the semiconductor. In the following section, the general electrical features of a p-type channel FET will be described.

Figure 3.4 shows the biasing conditions of the p-type transistors. Being a three terminal device, the gate voltage modulates the current flowing between the source and drain. In a p-type device, the threshold voltage V_{th} is normally negative. Thus for the transistor to work, a more negative voltage V_G than the threshold voltage should be applied. By convention, the source electrode acts as the source of the carrier flowing in the transistor. During the normal testing of a p-type transistor, the source is grounded (V_S=0V) while negative gate voltages (V_{GS}<0V) and drain voltages (V_{DS}<0V) are applied.

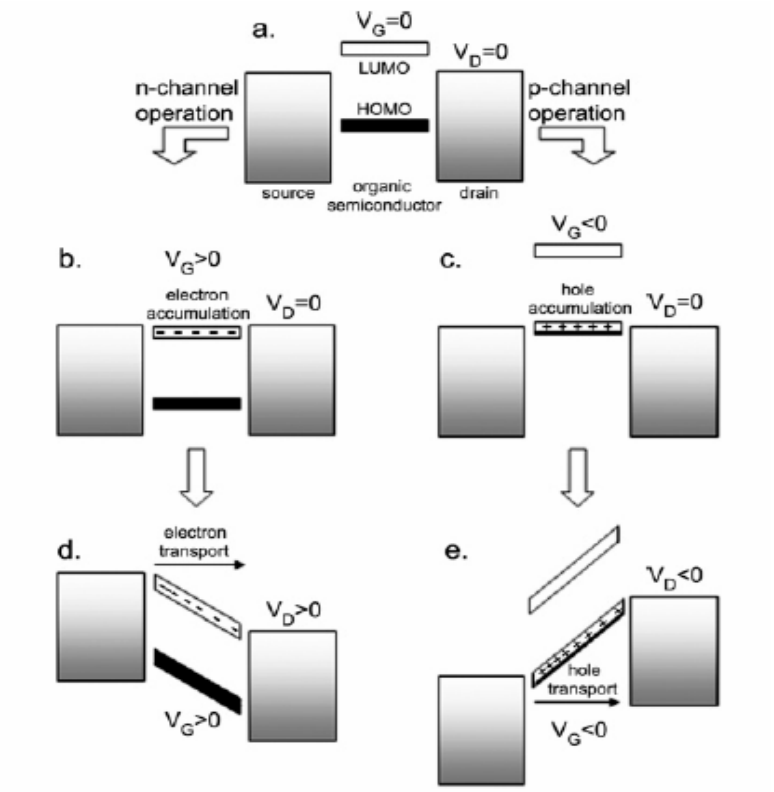

Figure 3.4:a) Idealized energy level diagram of an organic TFT at V_G = 0 and V_D = 0. (b-e) Demonstrate the principle of field effect transistor operation for the case of (b) electron accumulation, (d) transport, (c) hole accumulation, and (e) transport.[32]

In the channel, the two dimensional current density Jp flowing due to the holes is given by:

$$J_p = qpv_p \tag{3.1}$$

where q is the elementary charge, p is the hole density and v_p is the hole drift velocity. Thus the expression for the drain current which flows in an opposite direction to the hole current is given by:

$$I_d = -Wqpv_p \tag{3.2}$$

The charge density of the carriers and the drift velocity of the holes can be dependent on the spatial position in the channel. For the case of drift velocity, the dependence is as follows:

$$v_p = \mu_p E(x) = -\mu_p \frac{d\phi(x)}{dx} \tag{3.3}$$

In the above expression, μ_p is the hole mobility, $E(x)$ is the electric field directed from the source to the drain and $\phi(x)$ is the potential along the channel, at position x. The charge density generated in the channel region is independent of the position in the channel when there is no applied drain voltage. The formation of a conducting channel creates a capacitor structure with the gate electrode and the channel acting as the plates of a capacitor with the dielectric sandwiched in between.

Thus the total charge at the interface (Q) on the application of a gate voltage V_{GS} is give by:

$$Q = qp = -C(V_{GS} - V_{th}) \tag{3.4}$$

where C is the capacitance of the insulator. The negative sign in the above expression compensates for the negative gate voltages. Thus under the absence of the drain voltage, the concentration of charge carriers (p) is linearly dependent on the gate voltage. On the application of a potential between the source and the drain electrodes, the charge density becomes position dependent. Thus Equation 4 becomes:

$$qp = -C(V_{GS} - V_{th} - \phi(x) \tag{3.5}$$

Thus equation 3.2 can be rewritten as:

$$I_d = WC(V_{GS} - V_{th} - \phi(x))v_p \tag{3.6}$$

which when combined with equation (3.3) yields:

$$I_d = -\mu_p WC(V_{GS} - V_{th} - \phi(x))\frac{d\phi(x)}{dx} \tag{3.7}$$

On integrating the above expression over the length of the channel L, $0<x<L$ and $V_S< \phi(x) <V_D$ yields

$$I_d = -\mu_p \frac{W}{L} C\left[(V_{GS} - V_{th})V_{DS} - \frac{V_{DS}^2}{2}) \right] \quad (3.8)$$

This is the general equation for the drain current flowing in a p channel transistor. Depending on the magnitudes of the voltage V_{DS} and V_{GS}, the transistor could be said to be working either in the linear regime or the saturation regime. For a p-type channel FET, the linear regime corresponds to the range at which the absolute value of the drain-source voltage remains small compared to the absolute value of the difference between the gate-source voltage and the threshold voltage (i.e. $V_{DS} >> V_{GS} - V_{th}$, where all the quantities are negative). Under these conditions, the quadratic part of equation 8 can be ignored and thus the drain current becomes:

$$I_d = -\mu_p \frac{W}{L} C\left[(V_{GS} - V_{th})V_{DS}) \right] \quad (3.9)$$

Now, for a constant gate-source voltage ($V_{GS} = V_G - V_S = V_G$), a more negative voltage can be applied to the drain electrode, making the drain-source voltage become more negative ($V_{DS} = V_D - V_S = V_D$). If this is done while V_G remains constant then the absolute value of the difference between the gate and the drain voltage decreases (i.e. the gate-drain voltage, $V_{GD} = V_G - V_D$, becomes less negative). When the difference between the gate voltage and the drain voltage becomes equal to the threshold voltage ($V_{GD}=V_G-V_D = V_{th}$), the transistor enters the saturation regime. In this case equation 8 becomes

$$I_d = -\mu_p \frac{W}{L} \frac{C(V_{GS} - V_{th})^2}{2} \quad (3.10)$$

When the transistor enters the saturation mode, the voltage next to the drain electrode is smaller than the threshold voltage and the local electric field cannot accumulate enough charge at the surface of the semiconductor. Under this condition, a depletion region in which the charge carrier concentration is zero is formed at the drain side of the channel and the channel is said to be pinched-off. From this point on, any further

increase of the drain-source voltage has no consequence on the current flowing from drain to source and a current is maintained because the holes at the pinch-off position are swept away from the edge of the channel into the drain by the high electric field.

3.5 Contact effects in transistors

During the discussion regarding the electrical characteristics of field effect transistors, one of the inherent assumptions was the ohmic nature of the charge injecting contacts. This assumption is not completely valid in the vast majority of the organic transistor devices reported in the literature[33-39]. With considerable improvements in the material control of organic thin films and crystals, FETs with high mobility values are possible. A consequence of realizing high field-effect mobility is that the parasitic contact effects in OTFTs have become more pronounced and are now posing limits to the performance of the organic transistors.

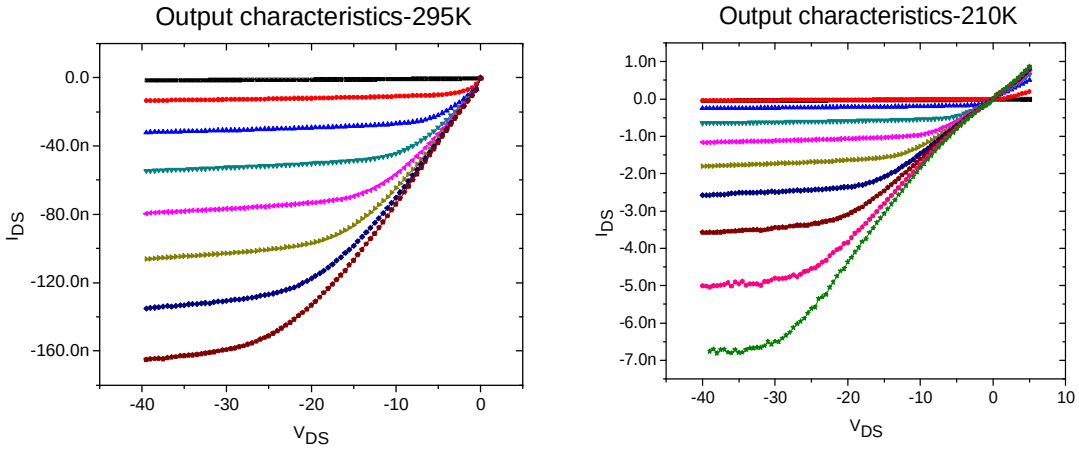

Figure 3.5: Output characteristics of a rubrene air-gap transistor (L=300 µm, W=1000µm) measured at 295K and 210K illustrating contact effects.

Figure 3.5 displays the output characteristics of a rubrene single crystal transistor constructed in the air-gap configuration as described in the previous section. The effect of contact resistance is clearly visible from the bunching of the output characteristics at the lower V_{DS} values. A cursory comparison of the output characteristics at 210 K reveals that the effects of the contact are more prominent at this lower temperature. In an organic FET there might be two possible contact effects, either contact resistance [34, 35, 39-43]or contact Schottky barriers[44-48]. The first might be caused by the formation of a high resistive area in the vicinity of the drain and source electrodes. This can impede carrier injection. Extraction of contact resistance in organic transistors is done usually be measuring device resistance for devices of varying channel lengths and then extrapolating them to zero. This treatment is valid normally for thin film transistors where the morphology of thermally grown thin films differs in the regions near bottom electrodes or when thermal evaporation of top electrodes creates defects on the organic thin films. Due to the design of the air-gap transistor, these effects are normally avoided.

On the other hand, when a metal is brought into intimate contact with a semiconductor, usually a depletion layer is formed at the interface[49]. When the respective work functions are different, a Schottky barrier results that limits the charge carrier injection. To a first approximation, both the source/rubrene contact and the drain/rubrene contact can be considered to be Schottky contacts so that the rubrene single crystal field effect transistor can be described as a pair of back-to-back, gate modulated diodes. A negative voltage on the drain (the situation during normal operation) results in a forward biased drain/rubrene junction and a reverse-biased source/rubrene junction. The resistance of the device is thus also determined by the reverse-biased source/rubrene contact.

The general form of the Schottky diode equation is[49]

$$J = J_o\left[\exp\left(\frac{qV}{kT}\right) - 1\right] \tag{3.11}$$

where J is the current density, J_o is the reverse saturation current (metal to semiconductor) and V is the applied bias. The expression for Jo depends on the relevant transport mechanism. Transport is typically limited by either thermionic emission of carriers over φ_B (the charge injection barrier) or subsequent drift/diffusion of carriers in the depletion region. The drift/diffusion limited injection pertains more to injection into low mobility semiconductors[49] and can hence be neglected for rubrene single crystal transistors. The term J_o for the thermionic emission is given by:

$$J_o = qN_v v_r \exp\left(\frac{-\phi_B}{kT}\right) \tag{3.12}$$

where q is the elementary charge, v_r is the recombination velocity of carriers crossing the metal/semiconductor interface, N_v is the effective density of valence band states and φ_B is the charge injection barrier.

Recent work [50-52]investigating the contacts between rubrene and a wide variety of metals (Ni, Co, Cu, Au and Pt) has shown that the reproducibility in the values of contact resistance strongly depends on the metal, with Ni showing a strong reproducibility as opposed to Au whose contact resistance varied by three orders of magnitude. The reproducibility of their devices with Cu electrodes (with a CuO_x surface layer) has allowed the systematic study of the barriers at the surface. Following the same formalism described above, Molinari et al have modified the conventional theory for Schottky diodes to include voltage-induced Schottky barrier lowering and the field-induced change in the dipole due to electrons occupying surface states.

The effect of the Schottky contacts on the performance of the rubrene single crystal transistors is more apparent at low V_{DS} values. This implies that the mobility values

extracted from the linear regime of the transistors are much more affected by contact effects as compared to saturation level mobilities. The difference in the values between the mobilities in the linear regime and that extracted from the saturated regime are normally much more significant as the channel length decreases[39]. This result is because the linear regime is more strongly affected by interface properties and contacts than the saturation regime. Any voltage drop across the electrode/semiconductor interfaces will lower the effective voltage across the channel and the currents that are used to compute the linear mobility. In the saturation regime, this same voltage drop has only a relatively small effect since the source drain current is already independent of the source-drain voltage.

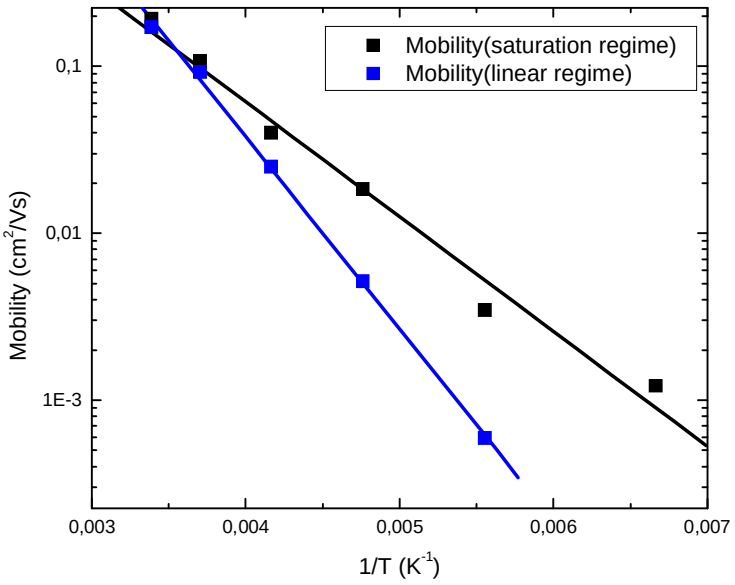

Figure 3.6: Mobility dependence on temperature for saturation and linear regime indicating the influence of the contacts. Activation energy extracted using simple Arrhenius dependence shows E_a=0.059eV for saturation regime, 0.1eV for linear regime

Figure 3.6 shows the mobility dependence of a contact affected rubrene transistor with temperature. The rapid increase of the Schottky barrier effect with reduction in temperature conceals the temperature dependent characteristics of the charge carrier

mobility of the rubrene crystal itself. The temperature dependence is well approximated as thermal activation, with the activation energy values of 0.1eV for linear mobilities and 0.059eV for saturation level mobilities. Since these devices were not completely contact limited, the temperature dependency is a convolution of the contact temperature dependence as well as the channel (rubrene) temperature dependence. As discussed previously, the effect of the contacts is more visible in linear mobility which decreases much more rapidly with reducing temperature.

The channel dimensions of the transistors measured during this thesis are large enough such that they do not result in the formation of completely contact limited devices. This has prevented a systematic study of the contact resistances for rubrene single crystal transistors. Similar to the results of Molinari et al, transistors prepared with the gold covered stamps showed variations in the output characteristics indicative of a wide range of contact effects. Thus for the photocurrent measurements described in the next chapter, samples with negligible contact effects were chosen.

This chapter has described the fabrication of the rubrene single crystal transistors beginning from the growth of an organic crystal to the lamination of the crystal on to the gold coated stamps. The working principle of the transistor has also been described as well as the influence of the electrode contacts to the semiconductor. After this introduction to the measurement configuration, the next chapter will detail the photocurrent properties measured in the rubrene crystal.

3.6 References

1. A. Pochettino, *Atti Accad. Naz. Lincei, Cl. Sci. Fis. Mat. Nat. Rend.*, 1906, **15**, 355.
2. W. G. Pfann, *Chemical and Engineering News*, 1956, **34**, 1440-1443.
3. W. G. Pfann, K. E. Benson and D. W. Hagelbarger, *Journal of Applied Physics*, 1959, **30**, 454-455.
4. K. H. Probst and N. Karl, *Physica Status Solidi (A) Applied Research*, 1975, **27**, 499-508.
5. N. Karl and J. Marktanner, *Molecular Crystals and Liquid Crystals Science and Technology, Section A: Molecular Crystals and Liquid Crystals*, 2001, **355**, 149-173.
6. C. Kloc, P. G. Simpkins, T. Siegrist and R. A. Laudise, *Journal of Crystal Growth*, 1997, **182**, 416.
7. R. A. Laudise, C. Kloc, P. G. Simpkins and T. Siegrist, *Journal of Crystal Growth*, 1998, **187**, 449.
8. C. Reese and Z. Bao, *Materials Today*, 2007, **10**, 20-27.
9. V. Y. Butko, X. Chi, D. V. Lang and A. P. Ramirez, *Applied Physics Letters*, 2003, **83**, 4773-4775.
10. R. W. I. De Boer, M. Jochemsen, T. M. Klapwijk, A. F. Morpurgo, J. Niemax, A. K. Tripathi and J. Pflaum, *Journal of Applied Physics*, 2004, **95**, 1196-1202.
11. V. Podzorov, V. M. Pudalov and M. E. Gershenson, *Applied Physics Letters*, 2003, **82**, 1739-1741.
12. R. W. I. De Boer, M. E. Gershenson, A. F. Morpurgo and V. Podzorov, *Physica Status Solidi (A) Applied Research*, 2004, **201**, 1302-1331.
13. V. Y. Butko, J. C. Lashley and A. P. Ramirez, *Phys. Rev. B*, 2005, **72**, 081312.
14. M. Kotani, K. Kakinuma, M. Yoshimura, K. Ishii, S. Yamazaki, T. Kobori, H. Okuyama, H. Kobayashi and H. Tada, *Chemical Physics*, 2006, **325**, 160-169.
15. H. Moon, R. Zeis, E. J. Borkent, C. Besnard, A. J. Lovinger, T. Siegrist, C. Kloc and Z. Bao, *Journal of the American Chemical Society*, 2004, **126**, 15322-15323.
16. K. Yamada, J. Takeya, K. Shigeto, K. Tsukagoshi, Y. Aoyagi and Y. Iwasa, *Appl. Phys. Lett.*, 2006, **88**, 122110.

17. V. Podzorov, E. Menard, J. A. Rogers and M. E. Gershenson, *Phys. Rev. Lett.*, 2005, **95**, 226601.
18. R. W. De Boer, N. N. Iosad, A. F. Stassen, T. M. Klapwijk and A. F. Morpurgo, *Appl. Phys. Lett.*, 2005, **86**, 032103.
19. R. W. I. De Boer, T. M. Klapwijk and A. F. Morpurgo, *Applied Physics Letters*, 2003, **83**, 4345-4347.
20. C. Goldmann, S. Haas, C. Krellner, K. P. Pernstlch, D. J. Gundlach and B. Batlogg, *Journal of Applied Physics*, 2004, **96**, 2080-2086.
21. C. R. Newman, R. J. Chesterfield, J. A. Merlo and C. D. Frisbie, *Applied Physics Letters*, 2004, **85**, 422-424.
22. A. F. Stassen, R. W. I. De Boer, N. N. Losad and A. F. Morpurgo, *Applied Physics Letters*, 2004, **85**, 3899-3901.
23. J. Takeya, C. Goldmann, S. Haas, K. P. Pernstich, B. Ketterer and B. Batlogg, *Journal of Applied Physics*, 2003, **94**, 5800-5804.
24. V. C. Sundar, J. Zaumseil, V. Podzorov, E. Menard, R. L. Willett, T. Someya, M. E. Gershenson and J. A. Rogers, *Science*, 2004, **303**, 1644-1646.
25. V. Podzorov, S. E. Sysoev, E. Loginova, V. M. Pudalov and M. E. Gershenson, *Applied Physics Letters*, 2003, **83**, 3504-3506.
26. Z. Bao, N. Kuck, J. Rogers and M. Paczkowski, *Advanced Functional Materials*, 2002, **12**, 526-531.
27. H. E. Katz and Z. Bao, *J. Phys. Chem. B*, 2000, **104**, 671-678.
28. E. Menard, V. Podzorov, S. H. Hur, A. Gaur, M. E. Gershenson and J. A. Rogers, *Advanced Materials*, 2004, **16**, 2097-2101.
29. C. D. Dimitrakopoulos, S. Purushothaman, J. Kymissis, A. Callegari and J. M. Shaw, *Science*, 1999, **283**, 822-824.
30. Y. N. Xia, J. A. Rogers, K. E. Paul and G. M. Whitesides, *Chemical Reviews*, 1999, **99**, 1823-1848.
31. T. Ono, D. Y. Sim and M. Esashi, *Journal of Micromechanics and Microengineering*, 2000, **10**, 445-451.
32. C. R. Newman, C. D. Frisbie, D. A. daSilvaFilho, J. L. Bredas, P. C. Ewbank and K. R. Mann, *Chem. Mater.*, 2004, **16**, 4436-4451.
33. A. B. Chwang and C. Daniel Frisbie, *Journal of Physical Chemistry B*, 2000, **104**, 12202-12209.

34. H. Klauk, G. Schmid, W. Radlik, W. Weber, L. Zhou, C. D. Sheraw, J. A. Nichols and T. N. Jackson, *Solid-State Electronics*, 2003, **47**, 297-301.
35. P. V. Necliudov, M. S. Shur, D. J. Gundlach and T. N. Jackson, *Solid-State Electronics*, 2003, **47**, 259-262.
36. K. Seshadri and C. D. Frisbie, *Applied Physics Letters*, 2001, **78**, 993-995.
37. R. A. Street and A. Salleo, *Applied Physics Letters*, 2002, **81**, 2887.
38. N. Stutzmann, R. H. Friend and H. Sirringhaus, *Science*, 2003, **299**, 1881-1884.
39. J. Zaumseil, K. W. Baldwin and J. A. Rogers, *Journal of Applied Physics*, 2003, **93**, 6117-6124.
40. B. H. Hamadani and D. Natelson, *Applied Physics Letters*, 2004, **84**, 443-445.
41. B. H. Hamadani and D. Natelson, *Proceedings of the IEEE*, 2005, **93**, 1306-1311.
42. J. A. Majewski, R. Schroeder and M. Grell, *Applied Physics Letters*, 2004, **85**, 3620-3622.
43. E. J. Meijer, G. H. Gelinck, E. Van Veenendaal, B. H. Huisman, D. M. De Leeuw and T. M. Klapwijk, *Applied Physics Letters*, 2003, **82**, 4576-4578.
44. R. Schroeder, L. A. Majewski and M. Grell, *Applied Physics Letters*, 2004, **84**, 1004-1006.
45. A. Bolognesi, A. Di Carlo and P. Lugli, *Applied Physics Letters*, 2002, **81**, 4646-4648.
46. M. Kawasaki, S. Imazeki, M. Ando and M. Ohe, Proceedings - Electrochemical Society, 2005.
47. G. C. R. Lloyd, N. Sedghi, M. Raja, R. Di Lucrezia, S. Higgins and W. Eccleston, Materials Research Society Symposium - Proceedings, 2002.
48. Y. Y. Zhang, Y. Shi, F. Chen, S. G. Mhaisalkar, L. J. Li, B. S. Ong and Y. Wu, *Applied Physics Letters*, 2007, **91**.
49. S. M. Sze, *Physics of Semiconductor Devices*, Wiley, New York, 1981.
50. A. S. Molinari, I. Guti?rrez Lezama, P. Parisse, T. Takenobu, Y. Iwasa and A. F. Morpurgo, *Applied Physics Letters*, 2008, **92**.
51. A. Molinari, I. Guti?rrez, I. N. Hulea, S. Russo and A. F. Morpurgo, *Applied Physics Letters*, 2007, **90**.

52. I. N. Hulea, S. Russo, A. Molinari and A. F. Morpurgo, *Applied Physics Letters*, 2006, **88**.

Chapter 4

Photoconductivity in rubrene single crystals

This chapter examines one of the most fundamental properties of an organic crystal- the photoconductivity. The creation of charge carriers under the excitation of incident illumination reveals many fundamental properties regarding the molecular and intermolecular processes at play in an organic crystal. There still exists a lot of controversy in the field regarding the fundamental process behind the formation of photogeneration of charge carriers in organics, with both direct photogeneration of carriers as well as exciton creation being observed. In addition to probing fundamental processes, photoconductivity is of practical use as well with applications in photodiodes and sensors. Despite the high level of interest in organic semiconductors, photocurrent studies in transistor configurations have been very few in number and primarily limited to thin-film configuration[1-6].

In this chapter, we report an investigation of the steady-state and transient photocurrents in rubrene single crystal field-effect transistors (SCFET) fabricated using the "air-gap" technique. The particular configuration used in this study allows us to modulate the density of the charge carriers at the surface of the rubrene crystal under pristine conditions in the absence of traps at the semiconductor-dielectric interface. This configuration is ideally suited for the study of the intrinsic photoelectrical properties of the rubrene semiconductor in FETs. Before proceeding to the photocurrent properties of the rubrene crystal transistors, it is instructive to look at the photoexcitation picture in organic materials.

4.1 **Photoexcitation picture in organic molecular crystals**

The nature of photoexcitation and charge carrier generation in organic molecular crystals as well as conjugated polymers has not been clearly understood despite the extensive research on the subject for the past few decades[7, 8]. A large number of excitations have been used to describe the various phenomena observed. These excitations include excitons, polarons and bipolarons. Two principal models which have emerged describing the nature of photoexcitation and carrier generation are the semiconductor band model and the molecular exciton model. The semiconductor band model has been used to describe the properties of inorganic semiconductors successfully. Akin to the creation of a valence band and a conduction band in semiconductors like Silicon and Germanium, the overlap of the bonding and the antibonding orbitals of organic molecules could lead to the formation of bands. In this case, the primary photoexcitations are mobile electrons and holes created by the absorption of photons with energies above the bandgap of the material. Accordingly, the onset of optical absorption at the band gap energy in the semiconductor coincides with the onset of photoconductivity. This has been observed in PPV thin films where the optical absorption edge and the onset in photoconductivity coincide at 2.3eV [9].

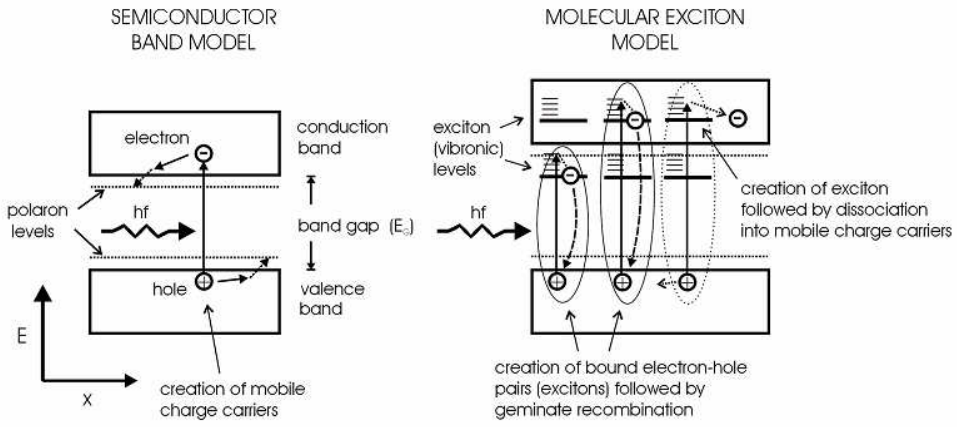

Figure 4.1: Energy band diagrams of photoexcitations in organic semiconductors according to semiconductor band model (left) and molecular exciton model (right).[10]

In other cases, the onset of photoconductivity occurs at energies much higher than the absorption edge. These cases are thus best described in terms of a molecular exciton model. In such cases, the primary species created during photoexcitation are strongly bound electron hole pairs (excitons) with binding energies as high as 0.5eV. The molecular exciton dissociates into photocarriers by various mechanisms including external electric fields, defects or thermal dissociation (Onsager model). Both the models are illustrated in Figure 4.1. At this point an introduction to excitons may be deemed appropriate

4.2 Excitons

Let us consider a transition of an electron from the valence band to the conduction band of a semiconductor induced by the absorption of a photon. The excited electron leaves behind a hole in the valence band, which behaves as a positive charge carrier. The electron interacts with the hole through a screened Coulomb potential and may therefore form bound states. The resulting bound electron–hole pairs are known as excitons. The presence of excitons induces strong effects in the optical properties of semiconductors. They manifest themselves as resonant peaks in the absorption, reflection and luminescence spectra corresponding to transitions to or from discrete bound states, and as shifts of the main spectral features due to the electron–hole interaction[11]. Excitons generated in inorganic semiconductors show a very small binding energy (5 to 30 meV) which is normally overcome by thermal energy. When a molecule is part of an extended molecular solid, its energetic processes are determined by the interaction with its neighbours. In the case of strong intermolecular interaction, the exciton can be delocalized over a number of molecules. Depending on the degree of delocalization the excitons are identified as Frenkel, charge-transfer or Wannier-Mott[7].

4.2.1 Frenkel excitons

The Frenkel exciton corresponds to a correlated electron-hole pair localized on a single molecule. Its radius is comparable to the size of a molecule or is smaller than the intermolecular distance (<5A°). A Frenkel exciton has no degrees of freedom and hence has no internal quantum numbers. It is considered a neutral particle that can diffuse from site to site. The local electric field of the exciton will polarize the surrounding lattice, and its motion can generate polaron-type quasi-particles. The Frenkel exciton is normally created in materials with low dielectric constant due to the strong coulombic interaction between the electron and hole.

4.2.2 Wannier-Mott excitons

The Wannier-Mott excitons in contrast to Frenkel excitons are normally seen in crystalline materials with strong intermolecular interactions. A significant potential overlap between the neighboring atoms reduces the Coulombic interaction between the electron and the hole of the exciton. This results in a large exciton radius (40-100A°) which is much bigger than the lattice constant. Wannier-Mott excitons are normally seen in inorganic crystals.

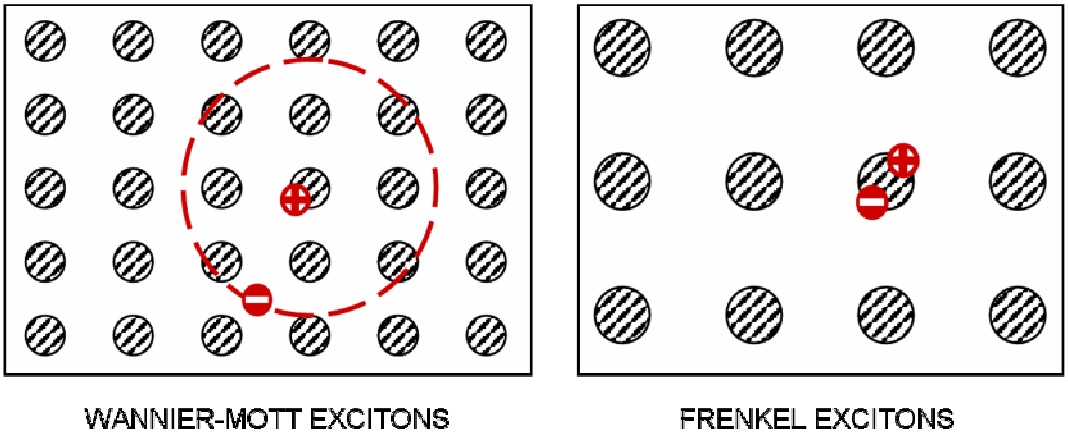

Figure 4.2: Illustration of the charge delocalization in Wannier-Mott and Frenkel excitons

4.2.3 Charge-Transfer excitons

The Charge-transfer exciton is of an intermediate size, neither very extended nor tightly bound at a single molecular site. Its theoretical formulation has proven difficult as it requires the reconciliation between the localized and extended character of the two aforementioned cases. A charge-transfer exciton can be considered as an unrelaxed polaron pair with the positive and negative polarons located on adjacent molecules[8]. But this picture is only true if each molecule forms a deep potential well in which charges are confined. Such a localized potential would be expected for a molecular crystal with weak intermolecular interactions and small overlap between the neighbouring orbitals.

In many of the organic molecular crystals, the primary photoexcitations are tightly bound Frenkel excitons[7-9, 12-14]. This is supported by the fact that the optical absorption spectrum of an organic molecular crystal is very similar to the absorption spectrum of the isolated molecule. This is due to the weak van der Waals bonding between molecules which preserve much of the original spectroscopic character of the molecule. One model for the origin of photoconductivity is described in Figure 4.3.

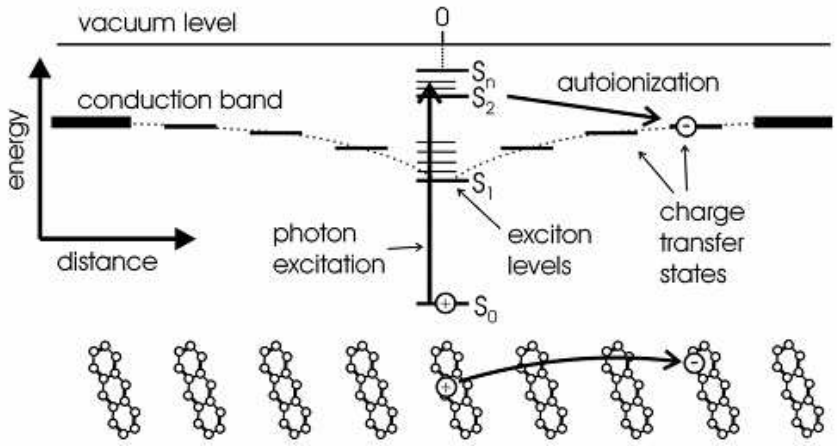

Figure 4.3: Descriptions of photoexcitations in organic molecular crystals. Adapted from [12]

Absorption of light causes a primary Frenkel exciton that is tightly bound and has a high probability for geminate recombination. The quantum yield for charge carriers close to the threshold for photoconductivity is, therefore quite low (10^{-4}). Given enough energy, the exciton may autoionize into charge transfer states on neighbouring molecules or dissociate completely into separated charge carriers (or polarons) at larger intermolecular spacings. Splitting of the exciton is also possible at interfaces, traps and at the application of an electrical field.

Next we introduce some basic concepts of photoconductivity. Since photoconductivity deals with the flow of charges, the equations that determine the current contributions deal with free carriers without taking into consideration the actual process of creation of charge carriers (through direct photoexcitation or through splitting of excitons). Subsequent retrapping of the photogenerated carriers is important especially while monitoring the transient nature of the photocurrent.

4.3 Basic concepts of photoconductivity

Photoconductivity was first noted in 1843 as a decrease in the resistance of amorphous selenium by shining light on it[15]. Since then, many publications and in depth analyses of the photoconductive properties of semiconductors have been published[16, 17]. The phenomenon of photoconductivity includes several processes which include (but are not limited to) light absorption, photogeneration of excitons, charge carrier generation and their subsequent transport, trapping, detrapping and recombination. The magnitude of the photocurrent response is linked to the quantum efficiency of forming charge carriers (which is the number of charge carriers produced on the absorption of one photon) as well as the mobility of the charge carriers. Studying the time evolution of photoconductivity on the other hand, reveals other properties of the semiconductor such as the lifetime of excited intermediate states (if any) as well as the lifetime of the charge carriers and the time required for them to encounter a trap. The knowledge of photoconductivity effects is much more important for organic semiconductors since the primary applications intended for these materials are in active matrix display applications.

The simplest photoconductivity experiment uses a constant monochromatic light source to generate equal excess densities of free electrons and holes, $\Delta n=\Delta p$, that lead to a change in the conductivity by

$$\Delta\sigma = \sigma_{ph} = e(\mu_n \Delta n + \mu_p \Delta p) \qquad (4.1)$$

where e is the electrical charge, μ_n and μ_p are the electron and hole mobility respectively. The basic experimental arrangement is illustrated in Figure 4.4 where *L* ands *A* are the length and cross-sectional area of the sample and the photocurrent *I*ph corresponds to $\sigma_{ph}AF$, with $F = V/L$ being the applied electric field.

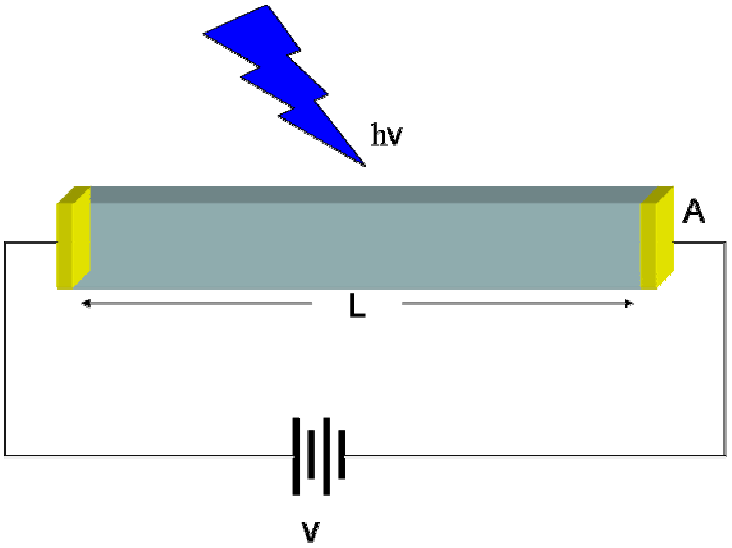

Figure 4.4: Simplest setup for measuring photoconductivity

In the experiments done during the extent of this thesis, coplanar electrodes are used which limit the study to the surface of the crystal. In many materials, a fraction of the photogenerated carriers becomes immobilized by trapping at various defects and traps such that not every part of Δn and Δp contributes equally to the photoconductivity in Equation 4.1. In fact, for a significant number of materials with widespread practical applications, either $\mu_n \Delta n$ or $\mu_p \Delta p$ product turns out to be much larger than the other one because of strongly unequal carrier mobilities. For instance, in intrinsic silicon the electron term dominates, while the photocurrent in chalcogenide glasses is carried by holes. In those instances, Equation 4.1 effectively reduces to a one-carrier equation. In the case of rubrene single crystals, the electron mobility (in the few cases it has been measured) is far exceeded by the hole mobility rendering the photoconductivity to be determined by the photogenerated holes.

The steady state nonequilibrium charge carrier density can also be written in the form of the product of the number of carriers liberated by light per unit time in unit volume

(G – the generation rate) and the average time of their existence in the band before recombination (τ). Thus equation 4.1 can be rewritten as

$$\Delta\sigma = \sigma_{ph} = e(\mu_n G\tau_n + \mu_p G\tau_p)$$
$$\Delta\sigma = eG(\mu_n\tau_n + \mu_p\tau_p) \tag{4.2}$$

This generation rate G is defined by

$$G = \eta(\frac{I_0}{h\nu})(1-R)\frac{(1-e^{(-\alpha d)})}{d} \tag{4.3}$$

where η is the quantum efficiency of the generation process, I_0 is the incident illumination intensity, hν the photon energy, R the reflection coefficient of the sample, α the optical absorption coefficient of the material and d is the thickness of the sample. In the case of photoexcitation configurations where the material has coplanar electrodes on them, the thickness effects can normally be neglected since only the carriers generated on the surface of the material contribute to the photocurrent.

4.4 Transient photoconductivity

If illumination begins at a certain moment, then the steady-state value of the equilibrium conductivity of a semiconductor is reached only after a finite time. Similarly, the nonequilibrium conductivity does not decay instantaneously when the illumination ceases. The rise or decay curves of the nonequilibrium conductivity are called the relaxation curves of the nonequilibrium conductivity. Since at any given time the electron and hole components of the nonequilibrium conductivity Δσ are proportional to the nonequilibrium densities Δn and Δp, studying the transient

photoconductivity in a system can reveal the dynamics of the photogenerated electrons and holes. The change in the number of carriers (electrons or holes) per unit time in unit volume is the difference between the number of carriers liberated (given by G) and the number of carriers that recombine. There are two special cases which can be considered, dependent on the recombination rates- monomolecular recombination (also called linear recombination) and bimolecular recombination (also called quadratic recombination).

4.4.1 Monomolecular recombination

Under monomolecular recombination, the rate of recombination or capture is proportional to the first power of the nonequilibrium carrier density. This case is realized, for example, when there are holes of only one type which recombine with the nonequilibrium electrons, and the density of these holes is very high and practically independent of illumination). In such a linear recombination case, the change in the nonequilibrium density of holes per unit time may be written in the form

$$\frac{d}{dt}(\Delta p) = G - \frac{\Delta p}{\tau} \tag{4.4}$$

Assuming constant intensity illumination beginning at t=0 and setting $\Delta p=0$ at t=0 as the initial condition, we obtain

$$\Delta p = G\tau\left(1 - e^{-\frac{t}{\tau}}\right) \tag{4.5}$$

Thus the relaxation of equilibrium density in the linear recombination case is exponential. If the sample is not illuminated, equation 4.4 can be rewritten as

$$\frac{d}{dt}(\Delta p) = -\frac{\Delta p}{\tau} \tag{4.6}$$

Considering that the illumination ceased at t=0, equation 4.6 can be solved to obtain,

$$\Delta p = G\tau e^{\frac{-t}{\tau}} \tag{4.7}$$

Thus in the case of linear recombination, the rise and decay curves for the nonequilibrium conductivity are exponential in nature and has a time constant equal to the lifetime of the charge carriers.

4.4.2 Bimolecular recombination

In this case, the rate of recombination is proportional to the square of the nonequilibrium carrier density. Following the procedure set forth in the previous section, in the presence of illumination:

$$\frac{d}{dt}(\Delta p) = G - \gamma(\Delta p)^2 \tag{4.8}$$

γ is the recombination (capture coefficient) which in turn is a product of the capture cross section and the average relative velocity between the electrons and holes.
When the illumination ceases, equation 4.8 reduces to

$$\frac{d}{dt}(\Delta p) = -\gamma(\Delta p)^2 \tag{4.9}$$

Solving the above equations leads to the expression for the rise and decay curves.

For rise

$$\Delta p = \sqrt{\frac{G}{\gamma}} \tanh t\sqrt{G\gamma} \tag{4.10}$$

For decay

$$\Delta p = \sqrt{\frac{G}{\gamma}} \frac{1}{t\sqrt{G\gamma}+1} \tag{4.11}$$

4.5 Steady state photoconductivity measurements in rubrene transistors

Thick rubrene crystals with large flat surfaces were used in the construction of air-gap field effect transistors. These crystals were laminated on to the soft PDMS (poly-methyl disoloxane) stamps by applying a small pressure on to them. For the purpose of the photocurrent measurements, the probing pads with the largest spacing between them were used (normally 200 μm). This was done to reduce the effects of the illumination at the electrode/semiconductor interface. A 405 nm blue laser (Compass 405 from Spectra-Physics) was used as the illumination source for the majority of experiments. The laser was operated mainly in the continuous wave (CW) mode but could be forced to apply pulses by the application of a TTL signal. All the voltages and currents were measured using Keithley 2602 parametric analyzer in the ambient on a Cascade Micro-probestation. The setup is shown in Figure 4.5.

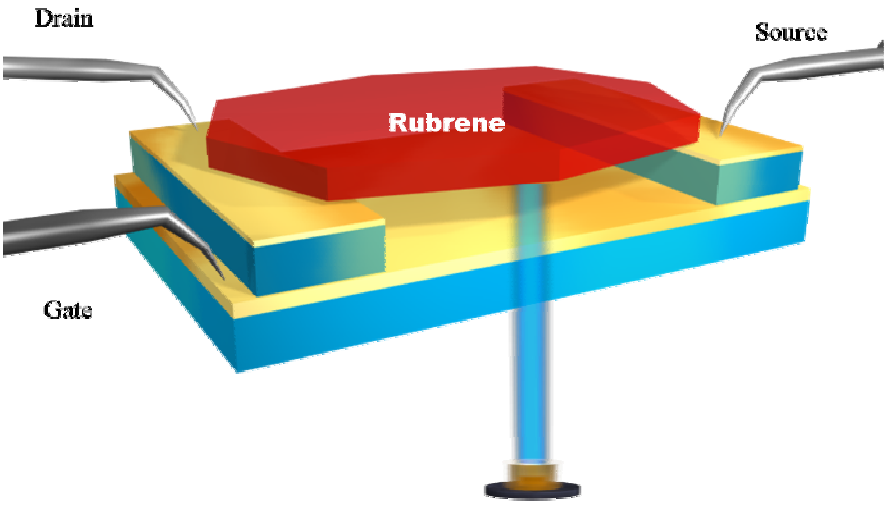

Figure 4.5: Illumination configuration during phototransistor measurements

Figure 4.6 shows the shows the output characteristics of a representative rubrene transistor measured in the dark and under 1.2mW illumination. . As is noted from the figure, the off current of the transistor (measured at V_{GS}=0V) has increased under the illumination and this extra contribution to the drain current is reflected in the output curves measured at other gate voltages[18].

$$I_{DS} = I_{dark} + I_{illum} \tag{4.12}$$

$$I_{DS} = \frac{\mu_h CW}{2L}\left[(V_{GS} - V_T)V_{DS} - \frac{V_{DS}^2}{2}\right] + \left(\frac{(Ne\mu_h WT)}{L}\right)V_{DS}$$

where C is the capacitance per unit area, W,L, and T are the channel width, channel length, and the thickness of the active material respectively and N is the charge density in the bulk. The charge density N is modulated by changing the incident optical power and a clear increase in the drain current with increasing optical density was observed in all the rubrene SCFETs tested.

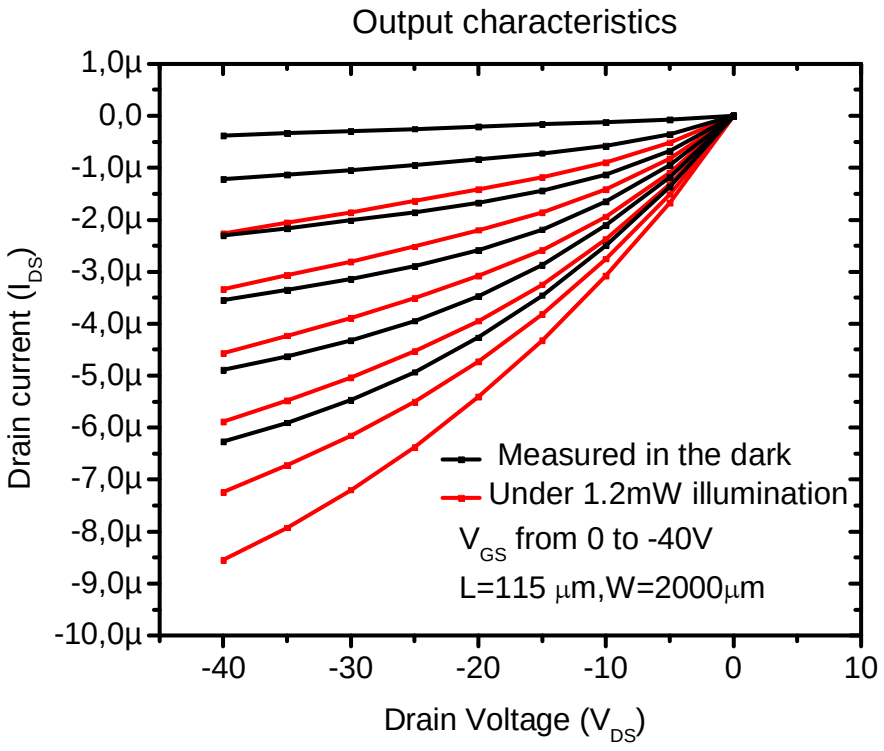

Figure 4.6: Output characteristics of a representative rubrene transistor in dark and under illumination showing clear photocurrent effects

The photosensitivity of the rubrene SCFETs defined as the ratio I_{illum}/I_{dark} shows higher magnitudes when the transistor is operating in a $V_{GS}<V_T$ regime. The highest photosensitivity measured was $2.65x10^{3}$ as measured in the off-state while the corresponding value under turn-on conditions was $2.6x10^{-1}$. This large difference (four orders of magnitude) is due to the high background dark current in the turn-on condition which reduces the effect of the photocurrent on the total current. This is supported by comparing the photocurrent measured in the on-state which is almost ten times higher than the photocurrent measured in the off-state.

The effect of the illumination can also be viewed through the transfer characteristics. The threshold voltages (used here to characterize the photocarrier concentration) were

obtained by plotting $(I_{DS})^{1/2}$ vs V_{GS} for the saturation regime. Figure 4.7 clearly shows that the threshold voltage V_T has shifted to more positive values with respect to the dark characteristics.

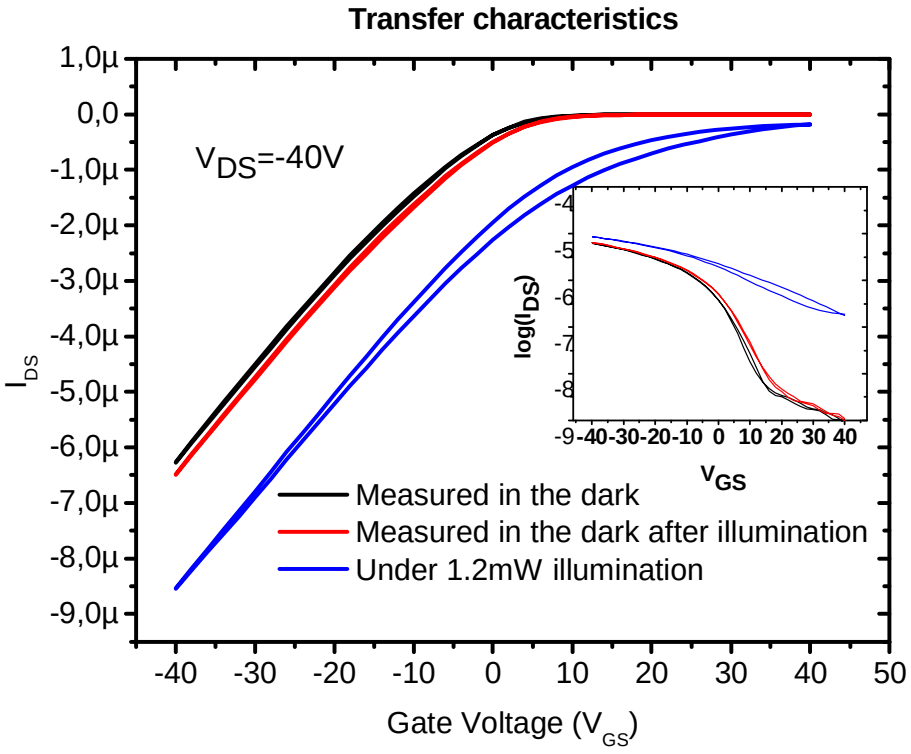

Figure 4.7: Excess carrier accumulation at the channel due to photogeneration expressed as a shift in threshold voltage

This V_T increase is as high as ~28 V, indicative of the intense photoresponse. Note that among the many SCFETs we tested the average increase of V_T is in the range of 20-22 V. The shift in the threshold voltage can be used to calculate the photocarrier concentration from the equation below:

$$\Delta n = \frac{C\Delta V_T}{e} \qquad (4.13)$$

where C is the dielectric capacitance per unit area =0.2nF/cm^2, ΔV_T is the threshold voltage shift under illumination and e is the elementary charge.

The average threshold voltage shift corresponds to a photocarrier concentration around of 2.5 x 10^{10}/cm^2. This concentration is comparable to the typical charge density created by the gate field in air-gap configuration and corresponds to 1.25 x 10^{-4} holes/molecule[19].An alternative way of looking at the threshold voltage shifts in the SCFET is by investigating the band-bending and energy level structure in the organic semiconductor in the direction normal to the channel of the device. This theory has been developed for TFTs based on amorphous silicon[20-22].

The non-equilibrium state of the illuminated device can be characterized by a splitting of the equilibrium Fermi level into two quasi-Fermi levels for each type of carriers[5, 6]. The splitting depends upon both the intensity and energy of the incident light. The band-bending (i.e. the effect the gate has on the accumulated carrier concentration in the channel), at a certain gate bias, is reduced in the illuminated device due to the increased density of charge carriers from photogeneration. A permanent threshold voltage shift in rubrene transistors with parylene dielectrics had been previously observed and attributed to charge transfer from the semiconductor to the dielectric under illumination[23]. In the case of the present SCFETs, the photocarriers generated at the interface are non-permanent due to the fact that there are fewer traps at the channel-dielectric interface to permanently immobilize them.

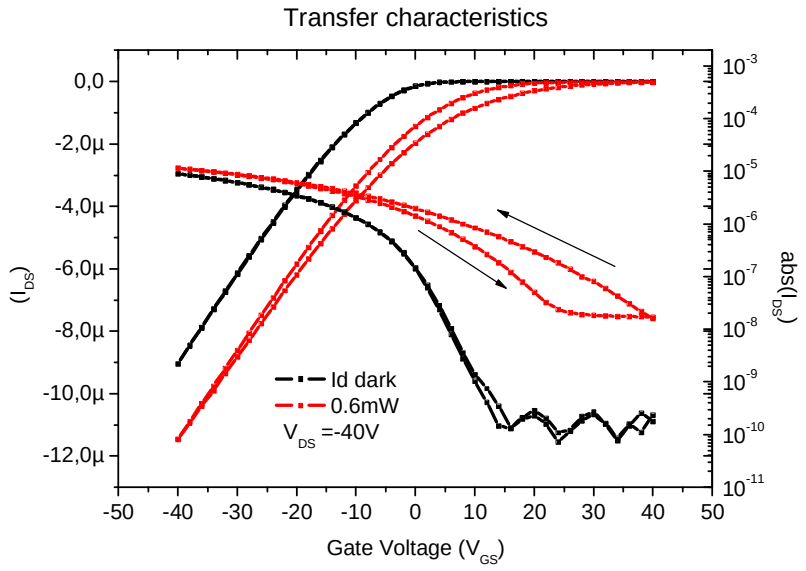

Figure 4.8:Hysteresis effects in the transfer characteristics caused due to illumination

The influence of photogenerated carriers is also visible by sweeping V_{GS} back and forth between +40 V and -40V (Figure 4.6). When performed in the dark, the $I_{DS}V_{GS}$ loop does not show any hysteresis. However, under light irradiation the transfer characteristics exhibit a hysteresis which can be explained by the effect of gate voltage on photocarriers. When the gate voltage is swept towards the negative voltages, the separation of charges as explained above occurs. The photoelectrons which move towards the bulk reduce the effective gate electric field applied at the channel, thus creating the hysteresis.

We have also measured the photocurrent transients in our setup. Figure 4.9 shows a typical time dependence of I_{DS} upon continuous illumination. The drain current I_{DS} measured at V_{GS}= -40V and V_{DS} = -40V increases initially and then saturates at a baseline value. Following I_{DS} saturation, the $I_{DS}V_{GS}$ transfer characteristics were measured. They were measured again after the light was turned off. The drain current decays gradually to the pre-illumination value over a period of 2 minutes. The measurement of the transfer curves displayed in Figure 4.7 is indicated on the graph.

It has to be noted that the gate and drain electric fields were not applied continuously through the whole time period, but at every 0.2s in order to minimize trapping at interfaces. This kind of persistent photoconductivity has been observed previously in organic polymeric thin film transistors of regio-regular poly(3-hexylthiophene) [24]and has been explained in terms of a model developed by Queisser et al[25]. Due to the presence of the gate voltage inducing a conductive channel, charge carrier separation would result with negative charges diffusing towards the semiconductor bulk and being trapped; meanwhile the photogenerated holes would move towards the channel region where the potential of positive charges is lowered. Both the fast and slow components of the decay are assumed to have an identical physical mechanism for recombination and vary only in the spatial separation of the photogenerated carriers. Thus the rate of recombination indirectly points to the spatial distribution of the electron traps in rubrene.

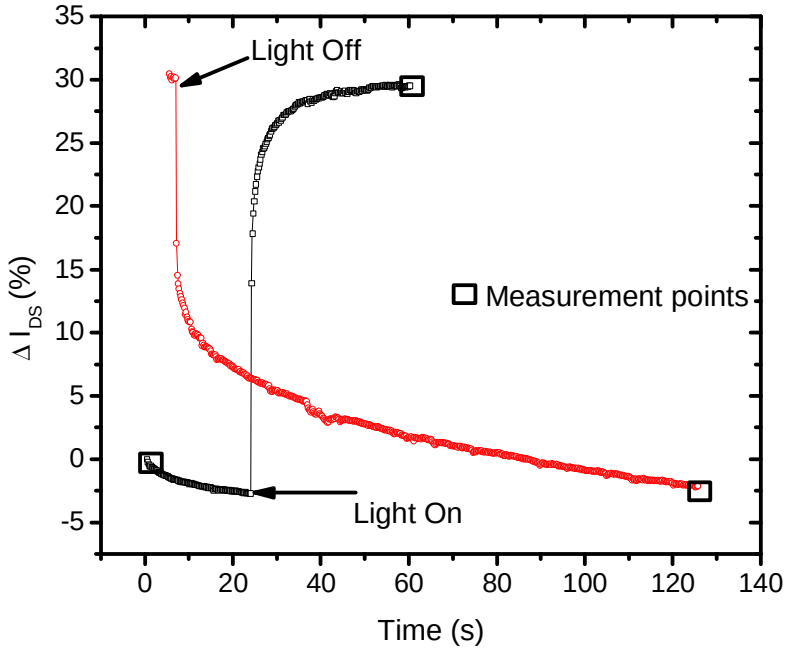

Figure 4.9: Persistent photoconductive effects created on illumination

Mitrofanov et al[26]. have recently proven the existence of an oxygen related deep acceptor band gap state in single crystal rubrene characterized by a photoluminescence band at 650nm. The details of the photoluminescence characteristics of rubrene and the influence of oxygen on it will be described in Chapter 5 and 6 respectively. Since all our experiments have been conducted in air and no special precautions have been used to prevent the oxidation of rubrene, it is reasonable to assume that these traps exist on the surface of the transistors tested in this experiment. We have conducted photoluminescence measurements on the surface of these crystals. The photoluminescence spectra were measured under excitation from a 488nm laser. They display a peak at 650 nm, indicative of the oxygen induced band states measured by Mitrofanov et al. (Figure 4.10)

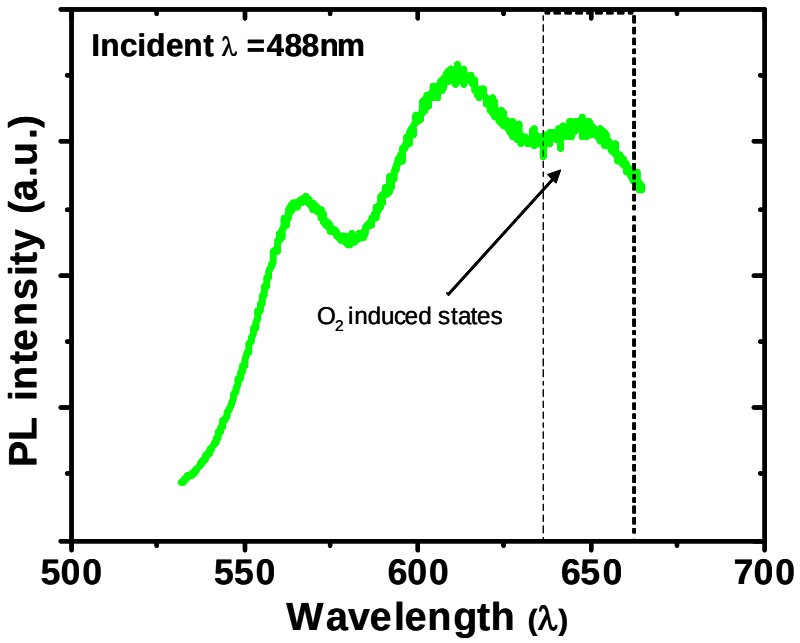

Figure 4.10: Photoluminescence spectra proving the presence of oxygen related band states on rubrene surface

In the case of optical excitation, the generated excitons could dissociate at these impurity sites with the electrons continuing to remain trapped while the holes drift towards the channel. Thus the presence of persistent photoconductivity can be explained by these oxygen generated traps.

This behavior is in stark contrast with the transient photocurrent measured on these samples (discussed in more detail in the later section). Figure 4.11 illustrates the photocurrent response when instead of steady state illumination; pulses of 600µs duration were applied to the crystal. The photocurrent response was recorded using a high speed probe (Picoprobe) and a 100 MHz TDS3014B oscilloscope.

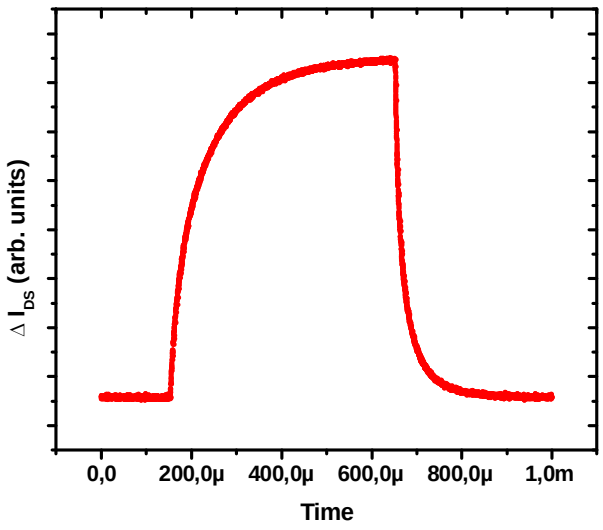

Figure 4.11: Representative photocurrent response under pulsed illumination

In contrast to the persistent photoconductivity clearly seen under continuous illumination, the photocurrent decays in about 100µs to its previous value. We believe that this difference arises from various spatial distributions of the electrons in the rubrene sample. The short pulse does not allow enough time for the photogenerated electrons to move into the bulk, thus resulting in immediate

recombination with the holes when the laser pulse is stopped. The general equation[25] for the rate of recombination of the electrons and holes R is

$$R = \left(\frac{\Delta n}{\tau_0}\right)\exp\left(\frac{-2x}{a}\right) \tag{4.14}$$

Where Δn is the persistent hole density and τ_0 is the lifetime for vanishing spatial separation, a is the Bohr radius and x is the distance between the electrons and the holes. This exponential dependence of the recombination on the distance between electrons and holes gives rise to the two different cases described above.

4.6 Photocurrent transients measured under pulsed illumination

As mentioned in the previous section, photocurrent transients were measured under pulsed illumination with the aid of an active electrical probe (GGB Industries, Picoprobe). Initial experiments had shown that the photocurrent transients being measured in the system were restricted by the impedance in the DC probes normally employed in common electrical measurements. The photoresponse is recorded with the aid of a TDS3014B oscilloscope (100MHz) with the aid of a program written in LABVIEW.

A representative photoresponse of the system has been previously displayed in Figure 4.11. It is to be noted that during the measurement of the transient photocurrent, the voltages in the transistors are applied first to create steady electric fields, before applying the laser pulses. The pulse widths are chosen so that the photogenerated current reaches a steady state. Photoconductivity is a complex phenomenon, as it involves various processes such as light absorption, charge photogeneration, charge transport, charge recombination and possible trapping and de-trapping from localized states. A transient photocurrent measured in a system can be either transport or

generation limited. The charge carrier mobility of holes measured in these rubrene single crystal transistors fall in the range of 10-20 cm^2/Vs. Assuming a lower bound value of 10 cm^2/Vs, the transit time for these carriers would be ~1µs. Since the width of the laser pulses applied to these samples greatly exceeds these transit times, it is safe to assume that the observed transient photocurrent is controlled by charge carrier generation processes rather than by transport[27]. We have also varied the horizontal electric field which determines the transit time of the charge carriers (by varying the drain voltage) and were not able to detect any significant change in the shape and form of the transients. This is indicative of the insensitivity of the photocurrent transients in the electric fields explored in this study.

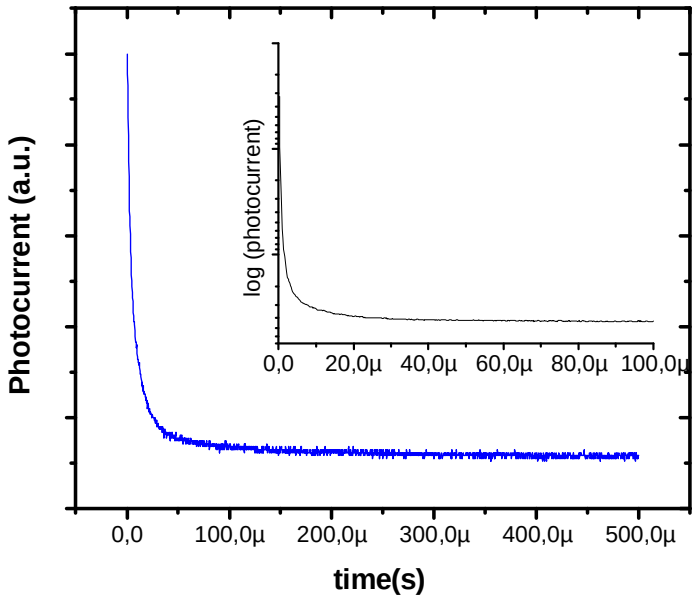

Figure 4.12: Non exponential behaviour of photocurrent decay eliminating monomolecular recombination at work

Figure 4.12 shows in detail the photocurrent decay which is non-exponential in nature. As discussed previously in this chapter, the non exponential nature of the photocurrent rules out monomolecular recombination as the decay process. We will therefore

model this decay by means of bimolecular recombination. For a Langevin type recombination process, carrier recombination is a random process and is kinetically bimolecular [28]. Such Langevin type recombination processes have been observed in anthracene [29] single crystals as well as octithiophene [30] and sexithiophene [31] single crystals. Under bimolecular recombination,

$$\frac{\delta p}{\delta t} = G - \gamma(p_0 + p)p \tag{4.15}$$

In Equation 4.15, G is the photogeneration rate; p_0 is the equilibrium density of charge carriers in rubrene while p corresponds to the number of photogenerated carriers and γ to the bimolecular recombination coefficient. The general solution of the above equation yields

$$p = p_0\left(\frac{p_0 + p(0)}{p(0)}\exp(\gamma p_0 t) - 1\right)^{-1} \tag{4.16}$$

where p(0) is the density of photocarriers at t=0.

At short time and under strong illumination, Equation 4.16 reduces to

$$\frac{1}{p} = \frac{1}{p(0)} + \gamma t \tag{4.17}$$

Our results are in agreement with the work of Najafov et.al [32]who have also identified a quadratic recombination process in rubrene single crystals between 510 and 420 nm wavelengths.

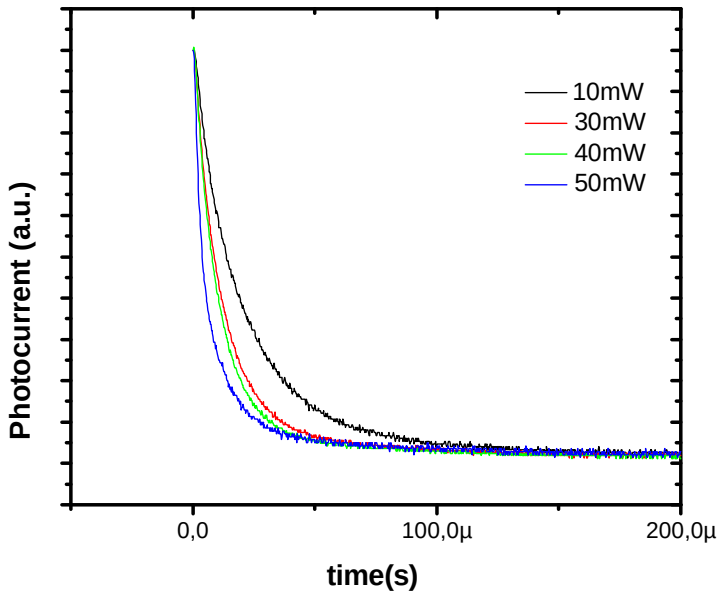

Figure 4.13: Optical power dependence on photocurrent transient

Figure 4.13 illustrates the normalized current decay curves at various incident optical powers. The Photoconductive decay waveform is found to be strongly dependent on excitation intensity; the higher is the intensity the faster is the decay rate. This is indeed expected from a bimolecular recombination process. The increase in the optical power leads to a higher density of photogenerated charge carriers which in turn increases the probability of recombination. This leads to the 'quicker' decay rates at high intensities

Another key factor to note in these decay curves is that the decay in the photocarriers is not immediate. The decay of the curves over a time scale extending into microseconds implies that there are other processes occurring as well. The appearance of such a long-lived photocurrent reveals the effect of localized states that significantly extend the carrier lifetime via a trapping and detrapping mechanism. Trap states in rubrene can arise from structural defects on the surface of the crystal or oxygen induced defects[33-35] .We had also measured the photoluminescence spectra on

the surface of the rubrene crystal which revealed a feature at 650 nm associated with the presence of oxygen induced defects. These traps are revealed to be spontaneously formed on the surface of the rubrene crystal on exposure to air. Models that consider the effects of charge localization in electrical traps have to take into consideration the rate equations for all the relevant impurity levels which lead to a set of non-linear differential equations. This approach, although complicated has been employed to inorganic semiconductors in a set of classical studies.[16, 17].

Thus photoexcitation in rubrene at 405 nm could be proposed to happen in two steps. First, the absorption of the photons result in the direct photogeneration of free charge carriers (as detected by pump probe experiments[36, 37]). The density of these free charge carriers subsequently fall due to bimolecular recombination as well as localization of the charge carriers in the trap states. The direct photogeneration of charge carriers present at 405nm need not be valid for other range of wavelengths where the photogeneration process could be complicated.[32]

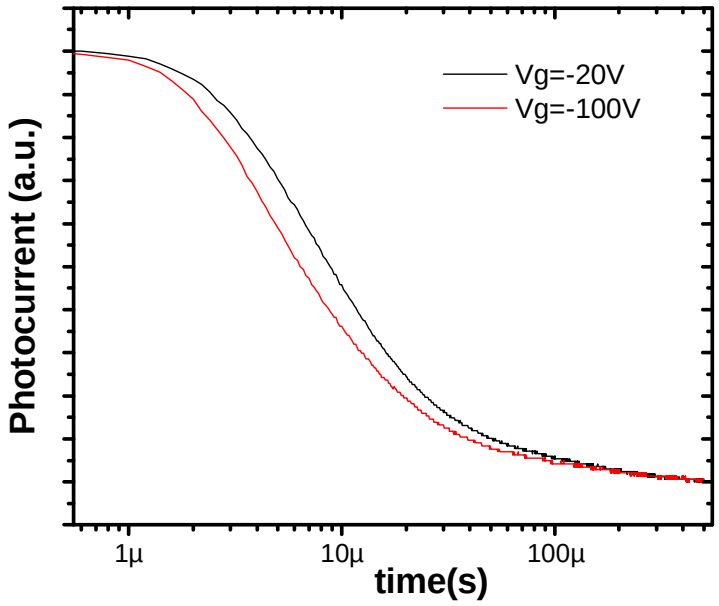

Figure 4.14: Gate voltage modulation of photocurrent transients

Figure 4.14 reveals the potential advantages of studying photocurrent dynamics in this air-gap transistor configuration. Due to the availability of a second vertical electric field (applied by the gate electrode), it is possible to study the photogeneration processes with varying concentrations of pre-excitation carrier density. In Figure 4.14, the application of a negative gate voltage induces holes to populate the surface before photo-excitation takes place. This results in an increased recombination probability of the photogenerated carriers, both due to the excess holes as well as because of increased carrier localization created by the gate electric field. In our current device configuration, the thickness of the air-gap is close to 4 micron, which limits the range of applied electric fields.

In summary, this chapter has looked at the steady state and transient photocurrent characteristics of rubrene single crystal studied in an air-gap transistor configuration. This has enabled the study of the rubrene crystal without the effects of a dielectric that can result in complications associated with trapping. Steady state characterization has revealed the generation of charge carriers with an areal density similar to that induced by the gate voltage during transistor operation. Persistent photoconductivity phenomenon has been observed associated with the trapping of photogenerated electrons on oxygen induced trap states. Transient photocurrents have revealed the presence of bimolecular recombination and other trap related dynamics at play.

4.7 References

1. M. Breban, D. B. Romero, S. Mezhenny, V. W. Ballarotto and E. D. Williams, *Appl. Phys. Lett.*, 2005, **87**, 203503.
2. K. S. Narayan and N. Kumar, *Applied Physics Letters*, 2001, **79**, 1891-1893.
3. Y. Y. Noh, J. Ghim, S. J. Kang, K. J. Baeg, D. Y. Kim and K. Yase, *J. Appl. Phys.*, 2006, **100**, 094501.
4. Y. Xu, P. R. Berger, J. N. Wilson and U. H. F. Bunz, *Applied Physics Letters*, 2004, **85**, 4219-4221.
5. M. C. Hamilton and J. Kanicki, *IEEE Journal on Selected Topics in Quantum Electronics*, 2004, **10**, 840-848.
6. M. C. Hamilton, S. Martin and J. Kanicki, *IEEE Transactions on Electron Devices*, 2004, **51**, 877-885.
7. M. Pope and C. E. Swenberg, *Electronic processes in Organic Crystals and Polymers*, Oxford University Press, New York, 1999.
8. E. A. Silinsh and V. Capek, *Organic Molecular Crystals: Interaction, Localization, and Transport Phenomena*, AIP Press, New York, 1994.
9. N. S. Sariciftci, ed., *Primary Photoexcitations in Conjugated Polymers: Molecular Exciton versus Semi-conductor band Model*, World Scientific, Singapore, 1997.
10. F. A. Hegmann, *La Physique au Canada*, 2003, **59**, 127-138.
11. G. H. Cocoletzi and W. L. Mochán, *Surface Science Reports*, 2005, **57**, 1-58.
12. R. Farchioni and G. Grosso, eds., *Organic Electronic Materials:Conjugated Polymers and Low Molecular weight Organic Solids*, Springer-Verlag, Berlin, 2001.
13. E. A. Silinsh, A. Klimkans, S. Larsson and V. Cápek, *Chemical Physics*, 1995, **198**, 311-331.
14. N. S. Sarciftci, ed., *Primary Photoexcitations in Conjugated Polymers: Molecular Exciton versus Semi-conductor Band Model*, World Scientific, Singapore, 1997.
15. W. Smith, *Nature*, 1873, **7**.
16. R. H. Bube, *Photoelectronic properties of semiconductors*, 1 edn., Cambridge University Press, Cambridge, 1992.

17. S. M. Ryvkin, *Photoelectric effects in semiconductors*, Consultants Bureau, New York, 1964.
18. F. Garnier, G. Horowitz, D. Fichou and X. Peng, in *Science and Application of Conducting Polymers*, eds. W. R. Salaneck, D. T. Clark and E. J. Samuelsen, Hilger, New York, Editon edn., 1991, p. 73.
19. E. Menard, V. Podzorov, S. H. Hur, A. Gaur, M. E. Gershenson, J. A. Rogers and Adv. Mater. 16, *Advanced Materials*, 2004, **16**.
20. A. O. Harm, R. E. I. Schropp and J. F. Verwey, *Philosophical Magazine B: Physics of Condensed Matter; Electronic, Optical and Magnetic Properties*, 1985, **52**, 59-70.
21. R. E. I. Schropp, A. O. Harm and J. F. Verwey, *Philosophical Magazine B: Physics of Condensed Matter; Electronic, Optical and Magnetic Properties*, 1986, **53**, 431-444.
22. C. Van Berkel and M. J. Powell, *Journal of Applied Physics*, 1986, **60**, 1521-1527.
23. V. Podzorov and M. E. Gershenson, *Physical Review Letters*, 2005, **95**, 016602-016604.
24. S. Dutta and K. S. Narayan, *Physical Review B*, 2003, **68**, 125208.
25. H. J. Queisser, *Physical Review Letters*, 1985, **54**, 234-236.
26. O. Mitrofanov, D. V. Lang, C. Kloc, J. M. Wikberg, T. Siegrist, W.-Y. So, M. A. Sergent and A. P. Ramirez, *Physical Review Letters*, 2006, **97**, 166601-166604.
27. M. Weiter, H. Bässler, V. Gulbinas and U. Scherf, *Chemical Physics Letters*, 2003, **379**, 177-182.
28. P. Langevin, *ACP*, 1903, **28**, 433-530.
29. N. Karl and G. Sommer, *Physica Status Solidi a-Applied Research*, 1971, **6**, 231.
30. D. Moses, J. Wang, A. Dogariu, D. Fichou and C. Videlot, *Physical Review B - Condensed Matter and Materials Physics*, 1999, **59**, 7715-7718.
31. G. Horowitz, F. Kouki, P. Valat, P. Delannoy and J. Roussel, *Physical Review B - Condensed Matter and Materials Physics*, 1999, **59**, 10651-10656.
32. H. Najafov, I. Biaggio, V. Podzorov, M. F. Calhoun and M. E. Gershenson, *Physical Review Letters*, 2006, **96**.

33. O. Mitrofanov, D. V. Lang, C. Kloc, T. Siegrist, W. Y. So, M. A. Sergent and A. P. Ramirez, Materials Research Society Symposium Proceedings, 2006.
34. O. Mitrofanov, D. V. Lang, C. Kloc, J. M. Wikberg, T. Siegrist, W. Y. So, M. A. Sergent and A. P. Ramirez, *Physical Review Letters*, 2006, **97**.
35. O. Mitrofanov, T. Siegrist, D. V. Lang, C. Kloc, W. Y. So, M. A. Sergent and A. P. Ramirez, Annual Proceedings - Reliability Physics (Symposium), 2007.
36. O. Ostroverkhova, D. G. Cooke, F. A. Hegmann, J. E. Anthony, V. Podzorov, M. E. Gershenson, O. D. Jurchescu and T. T. M. Palstra, *Applied Physics Letters*, 2006, **88**.
37. O. Ostroverkhova, D. G. Cooke, F. A. Hegmann, J. E. Anthony, V. Podzorov, M. E. Gershenson, O. D. Jurchescu and T. T. M. Palstra, Materials Research Society Symposium Proceedings, 2006.

Chapter 5

Optical Characterisation of rubrene crystals

Techniques using electromagnetic radiation are very useful in the probing of the properties of solids. The very short wavelengths of X-rays are essential in the study of atomic lattices which define crystalline solids while the wavelengths through the visible and infrared to the millimeter range provide valuable information as well. In the case of semiconductors, the electronic structure including the band gap is determined by the absorption spectra while the crystalline lattice and its quantized vibrations are studied through phonons. This chapter details the various optical spectroscopies performed on rubrene (either in the single crystalline form or in the form of a solution) to characterize the properties of this interesting molecule. The techniques detailed in this section include the absorption spectra, Photoluminescence, and UV- Raman Spectroscopy.

Absorption of light raises the molecule from the ground state to one of the upper electronically excited states. From the excited state, the molecule can return to the ground state in a variety of ways as indicated in Figure 5.1. It can return to the ground state with emission of fluorescence, through intersystem crossing (possibly followed by the emission of phosphorescence), through internal conversion (a direct return to ground state without fluorescence), intramolecular charge transfer and conformational change. The presence of other molecules near the photoexcited molecule (as is the case of organic solids as well as concentrated solutions) could lead to processes like electron transfer, proton transfer, energy transfer, excimer and exciplex formation. The processes of fluorescence and phosphorescence are grouped together under the title of photoluminescence.

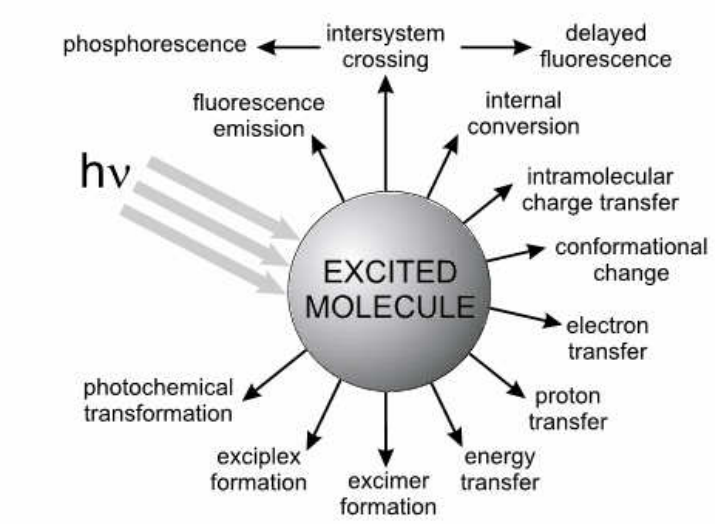

Figure 5.1: Possible de-excitation pathways of excited molecules

5.1 Absorption and luminescence in Rubrene

5.1.1 Theory

The emission of light is closely tied in with the absorption process and is described by Einstein's B coefficient. Einstein's coefficient A_{nm} describes the rate for spontaneous emission due to a transition from energy level n to m, while B_{nm} is the rate for either absorption or stimulated emission from level n to level m which Einstein has proved to be equal to B_{mn} (i.e. $B_{nm}=B_{mn}$).

Einstein's constant of absorption B appears as the transition rate per unit energy density of the radiation. The values of B for each absorption is dependent on the transition moment associated with the displacement of charges during the transition. On the other hand, in classical theory, the molecular absorption of light can be described by considering the molecule as a collection of damped oscillator states characterized by angular frequencies, damping constants and effective charges. The degree to which this maximum charge is realized is incorporated in a parameter *f*

called the oscillator strength of the transition. The oscillator strength f can be shown to be related to the square of the transition moment integral, thus bridging the gap between classical and quantum mechanical approaches. The concept of transition moment is especially important for all experiments carried out with polarized light. The transition moment can be drawn as a vector in the coordinate system defined by the location of the nuclei of the atoms and therefore the molecules whose absorption transition moments are parallel to the electric vector of the linearly polarized incident light are excited. The probability of excitation is proportional to the square of the scalar product of the transition moment and the electric vector. This probability is thus at its maximum when the two vectors are parallel and zero when they are perpendicular[2].

In addition, the absorption transitions that can occur in conjugated molecules are restricted by spin considerations. Transitions between states of different multiplicities are forbidden, i.e. singlet –singlet and triplet- triplet transitions are allowed, but singlet–triplet and triplet–singlet transitions are forbidden. However, there is always a weak interaction between the wavefunctions of different multiplicities via spin-orbit coupling. As a result, a wavefunction for the singlet state always contains a small fraction of a triplet (or singlet) wavefunction which leads to a small but non-negligible value of the intensity integral during a transition between a singlet state and a triplet state or vice versa

5.1.2 Absorption spectra of rubrene solution and crystals

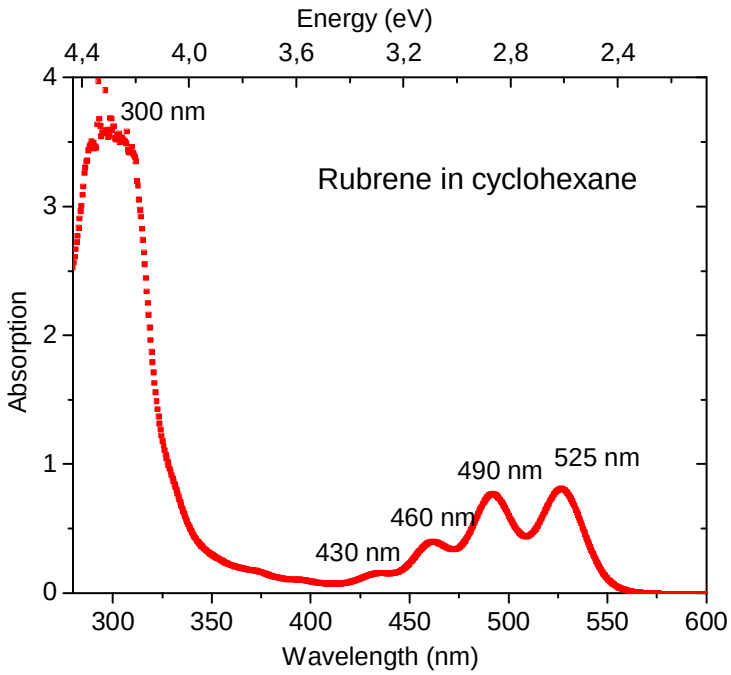

Figure 5.2: Absorption spectrum of rubrene solution in cyclohexane

The graph above shows the absorption spectra of rubrene powder (purchased from Aldrich) dissolved in cyclohexane. The spectra were collected on a Perkin Elmer Lambda 900 UV-Vis-NIR spectrophotometer. There are two main regions of absorption for rubrene. The first is a region of high intensity absorption at about 300nm and corresponds to the S_0-S_2 transition. This region has also been denoted as Group I absorption bands by Braude[3] . The second set of transitions (at 430nm -2.88 eV, 460nm -2.69 eV, 490nm-2.53 eV and 525nm-2.36 eV) corresponds to the vibronic bands of the ^1L_a-^1A transition[4-6]. The spectrum of rubrene resembles that of the parent hydrocarbon, tetracene very closely and this may be taken as evidence that the four phenyl groups are not coplanar with the central tetracene backbone, so that conjugation is markedly reduced[7-9].

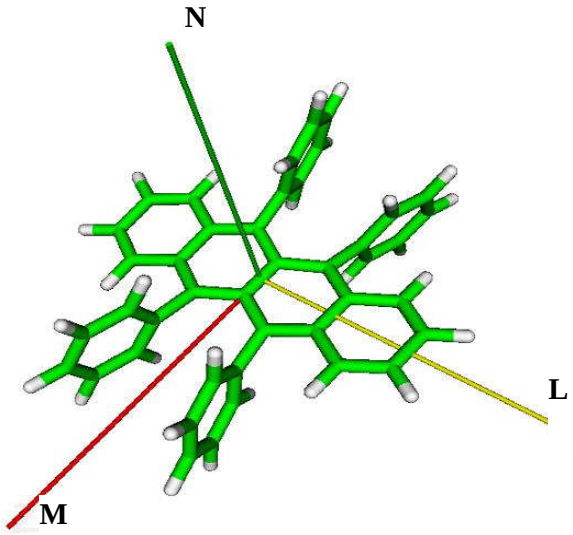

Figure 5.3: Rubrene molecule with the L, M, N molecular axes defined.

The rubrene molecule in figure 5.3 possesses C_{2h} symmetry with the twofold axis of rotation along the short backbone axis M. The molecular dipole-allowed excited states have symmetry either A_u or B_u with dipole moments along M and in the LN plane respectively where L is the long molecular axis and N the normal to the backbone plane (Figure 5.3).Theoretical simulations performed using INDO/SCI method to calculate the oscillator strength have shown that the first transition (measured here at 525 nm) is polarized along M axis while the other transitions are LN polarized[10-12].

The absorption spectra above can be compared to that of the rubrene crystal available in the literature[11, 13, 14]

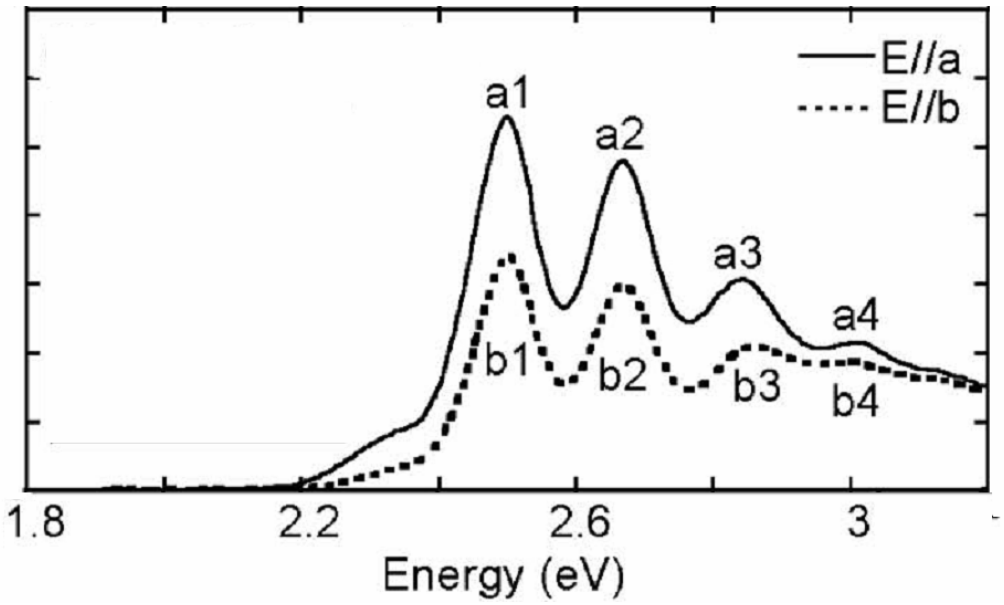

Figure 5.4: The absorption spectra of rubrene crystal. Adapted from[14]

Figure 5.4 shows the absorption spectra of the single crystal taken at normal incidence on the ab face with a and b polarized light showing vibronic progressions with main peaks at 2.50 eV, 2.67 eV, and 2.86 eV as well as a weak shoulder is detected centered at about 2.32 eV. In considering the absorption spectra of the crystal, it must be remembered that according to the definitions of the molecule axes above, the short axis M lies along the c direction of the crystal. The L axis lies along the ab plane at an angle of 31^0 to the a-axis. This implies that each A_u excited state (M polarized) gives rise to a dipole allowed excitonic state in the crystal with a c polarization. The B_u transitions polarized in the LN plane of the single molecule are split with polarizations along the a axis and b axis. The transitions marked a1,a2 and b1,b2 etc in Figure 5.4 are attributed to a and b polarized excitonic vibrations arising from the molecular transition at 3.09 eV with LN polarization. Due to the fact that the absorption spectra was measured at normal incidence, the lowest electronic transition which gives rise to a c polarized transition in the crystal is not detected and is only observed in the absorbance spectra measured at an oblique angle[14]. Another critical conclusion is the weak indication of Davydov splitting in the rubrene crystal spectrum which is apparent in the tetracene spectrum. This implies that the steric factors due to the side

phenyl groups diminish the crystalline forces in rubrene such that the environment may be said to resemble that of a solid solution rather than a crystalline array of identical molecules[15, 16].

5.2 Photoluminescence Spectroscopy

Photoluminescence is the direct emission of light from an excited medium under the photoexcitation of electrons. In photoluminescence, the excitation source is greater in energy than the energy gap of the material, in order to promote electrons to excited states. After a relaxation period, electrons that fall back to lower states through radiative recombinative pathways emit photons. Due to thermal relaxation whereby the excess energy of the excited electrons can be non-radiatively lost, the emitted photons have no correlation with the excitation process (wavelength used for excitation).

5.2.1 Theory

The Einstein coefficient A determines the rate for radiative transitions between two levels. If the upper level has a population N at time t, the radiative emission rate is

$$\left(\frac{dN}{dt}\right)_{radiative} = -A_{mn}N$$

Solving this to find the population of the upper state as a function of time yields:

$$N(t) = N(0)e^{-At} = N(0)e^{-t/\tau_R}$$

where $\tau_R = A^{-1}$ is the radiative lifetime of the transition.

Electrons can also relax through non-radiative pathways, for example by emitting phonons or getting trapped in defects and impurities. Taking both the radiative and non-radiative path into account, the total emission rate of the excited state is

$$\left(\frac{dN}{dt}\right)_{total} = -\frac{N}{\tau_R} - \frac{N}{\tau_{NR}} = -N\left(\frac{1}{\tau_R} + \frac{1}{\tau_{NR}}\right)$$

The photoluminescence efficiency is the ratio of the radiative emission rate to the total de-excitation rate. Thus,

$$\eta_R = \frac{\left(\frac{dN}{dt}\right)_{radiative}}{\left(\frac{dN}{dt}\right)_{total}} = \frac{AN}{N(1/\tau_R + 1/\tau_{NR})} = \frac{1}{1+\tau_R/\tau_{NR}}$$

5.2.2 Luminescence in conjugated systems

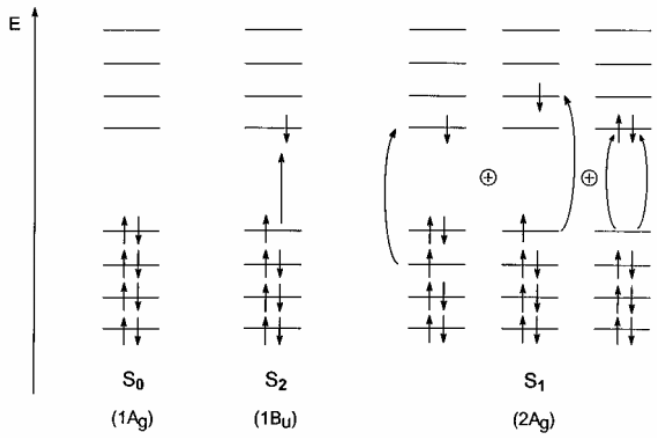

Figure 5.5: Schematic illustration of the main electronic configurations contributing to the ground state S_0 and the lowest singlet excited states S_1 and S_2 in the case of octatetraene. From [17]

Most fluorescent compounds are aromatic. The molecular structure of these compounds determine the nature of the lowest lying transition and hence the absorption and luminescent characteristics. In the case of π- conjugated systems, the excited state electronic structure is strongly dependent on the effective degree of bond-length alternation. This is most apparent when comparing conjugated polymers such as polyacetylenes who have purely polyenic backbones with poly (p-phenylene-vinylene) who have a mixed aromatic-polyenic backbone. In polyenes, the singly

excited HOMO to LUMO +1 and HOMO-1 to LUMO configurations and the doubly excited HOMO to LUMO configuration (illustrated in figure 5.5) strongly mix and result in the $2A_g$ state being located below the $1B_u$ state. In the $1B_u$ excited state, the π-bond densities are strongly modified and are characterized by a significant reduction in the C-C bond alternation. This means that in polyenes, the lowest excited singlet state, S_1 is one-photon forbidden vs. the ground state. The consequence is that polyenes and polyacetylenes do not luminesce. In the case of polymers with mixed aromatic character in the backbone (as in poly (p-phenylene-vinylene)) or a completely aromatic backbone (as in poly(p-phenylene) and poly(2,5-thienylene)), the $2A_g$ state becomes destabilized vs. the $1B_u$ state up to the point that $1B_u$ becomes the lowest singlet S_1 state. As a result, poly (p-phenylene-vinylene) and its derivatives are strongly luminescent[18].An increase in the extent of the pi-electron system leads to a shift in the absorption and fluorescent spectra to longer wavelengths and to an increase in the fluorescent quantum yield. This simple rule is illustrated by the series of linear aromatic hydrocarbons: naphthalene, anthracene, tetracene and pentacene emit fluorescence in the ultraviolet, blue, green and red respectively.

There are various radiative processes that occur in semiconductors that can give rise to photoluminescence. One of the primary processes occurring in semiconductors is the band-to-band transitions. This happens when an excited electron in the conduction band recombines with a hole in the valence band. If the semiconductor has a direct band gap and an allowed electric dipole transition; this recombination occurs with high probability. In indirect semiconductors, the recombination can only occur if it is mediated by a phonon. The simple band to band transitions mentioned above are valid only at high temperatures or at low trap densities. At low temperatures or high trap densities, the excited electrons can recombine radiatively with holes trapped on acceptor like impurities. The wavelength of the photons emitted thus, reveal the energetic location of the impurities. As mentioned in the previous chapter, excitons

are very commonly formed in organic molecular crystals due to the low dielectric constant which leads to a strong electron-hole interaction. If these excitons annihilate radiatively, a free-exciton peak will be present in the emission spectrum. Another critical factor that can determine the PL spectrum is the presence of environmental impurities that can act as exciton dissociation centers.

5.2.3 Luminescence in rubrene solutions and crystal

The luminescence spectra of both the crystal and solution were measured. Solution measurements were performed on a Shimadzu RF-5301 spectrafluorophotometer.

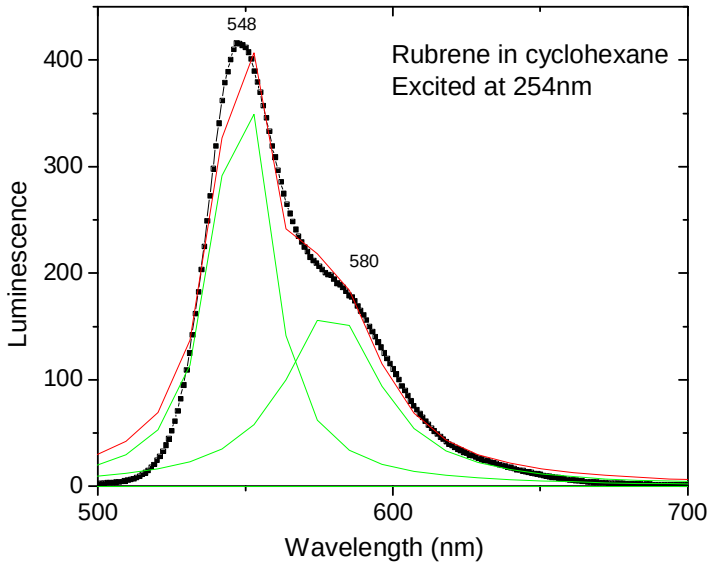

Figure 5.6: Luminescence spectra of rubrene solution(excited at 254 nm)

The luminescence shows two main peaks at 548 nm and 560 nm in agreement with previously published data[5, 15, 19-22]. In addition to direct photoexcitation, rubrene solutions have also been shown to display delayed fluorescence especially in the presence of sensitizers like anthracene. Delayed fluorescence of P-type acts through the interaction of two triplet states in the solution whose collision can provide enough energy to allow one of them to return to the singlet state. Rubrene is also able to self

sensitize although with a much lower efficiency due to the low yield of triplet states formed under direct photoexcitation of rubrene solutions. The efficiency of the delayed fluorescence in rubrene increases in the presence of oxygen in the solutions due to the propensity of the triplet states to react with it. This increased luminescence is in competition with the parallel photo-oxidation process which results in a final loss of luminescence[23].

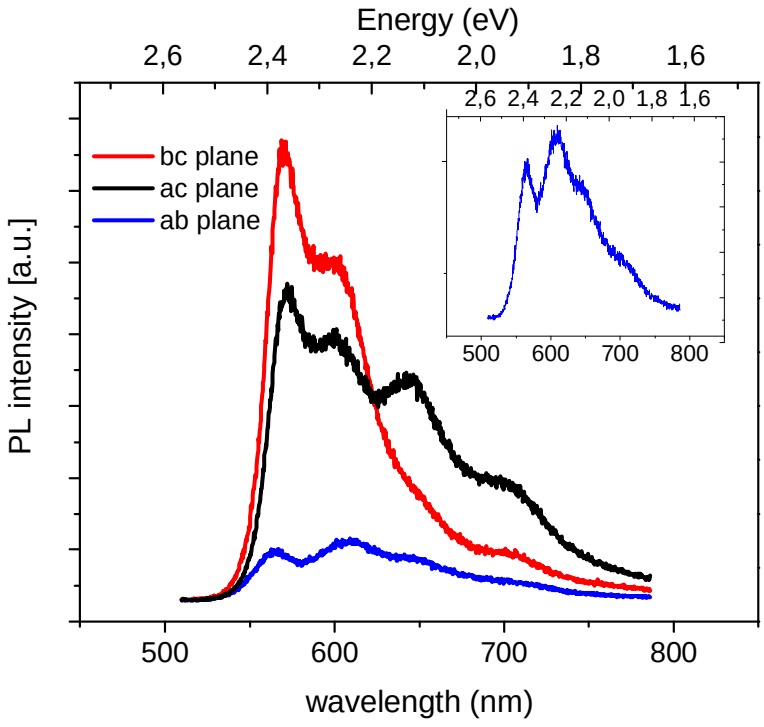

Figure 5.7: Photoluminescence spectra measured on the different facets of the rubrene crystal. Inset shows the ab plane result in more detail

The measurement of photoluminescence in rubrene crystal is complicated due to the wave guiding effects present in the crystal. Thus the measured photoluminescence spectra can depend on the incident angle of the excitation as well as the area addressed by the collection optics. The photoluminescence characteristics of the crystal were measured using a 488 nm laser focused through a 100X microscope lens (WITec CRM200). This allowed a very local measurement of the photoluminescence with reduced wave guiding effects.

Figure 5.7 displays the photoluminescence characteristics for the different facets of the crystal. The photoluminescence measurement on the ab plane reveals two main PL bands at 610 nm (2.03 eV) and 565 nm (2.19 eV) with the former peak stronger in comparison. In contrast, the PL band at 565 nm dominates the spectra measured on the ac plane and bc plane. This is a clear indication that the dipole moment of the corresponding optical transition that gives rise to the PL band at 565 nm is polarized along the c axis. As discussed previously, the molecular short axis M of the rubrene molecule lies in the plane of the c-axis. Thus it is logical to attribute this c-polarized band to the lowest M polarized transition in the rubrene molecule (indicated in the solution absorption spectra at 525 nm). It must be noted that the detection of the c-polarized emission at the ab surface was possible only because the emission is collected within a nonzero solid angle. The PL band at 610 nm on the other hand, can be attributed to L polarized transitions. The additional peaks present in the spectrum measured on the ac plane may be related to defects on the surface of the ac plane.

Important work done by Najafov et al[13] on the primary photoexcitations in rubrene have identified the species emitting the peak at 565 nm as a free exciton created by photoexcitation with incident energies above 2eV. This was evidenced by the difference in the excitation spectrum with respect to other PL bands. The authors attributed the band emitting at 620 nm to a self-trapped molecular exciton created by a transition from the free-exciton state in order to explain the observation that the transient photoluminescence arising from the molecular exciton has the same excitation spectrum as the free exciton. Pronounced molecular vibronic bands in the PL spectrum have been suggested as proof that photogenerated carriers are initially tightly bound in the form of molecular excitons that can couple to the molecular vibration. Mitrofanov et al [24] on the other hand have argued that the transient photoluminescence is an indication of oxide related defects on the surface of the rubrene crystal. However both the c transition of M origin and the a and b transitions

of LN origin contribute to the population of the emitting level, as deduced from the continuous-wave excitation spectrum by monitoring the PL at 620 nm[13].

5.3 Raman spectroscopy

In the context of semiclassical electron transfer[25-27] theory and its extensions, there are two major parameters that determine self-exchange electron-transfer rates and ultimately charge mobility: (i) the electronic coupling (transfer integral) between adjacent molecules, which needs to be maximized and (ii) the reorganization energy λ, which needs to be small for efficient transport. Measurement of the Raman spectra is an ideal tool to investigate the intermolecular interactions in a rubrene crystal as a source for the high mobilities.

5.3.1 Theory

During the course of the development of the quantum mechanical theory of light scattering at the beginning of the century, Smekal who was studying the scattering of light by a system with two quantized levels predicted that the radiation scattered from the molecules contains not only photons with the same frequency, but also some with a changed frequency[28]. The actual discovery of this inelastic scattering of light rose from the fascination of Sir Chandrasekhara Venkata Raman with the deep blue colour of the Mediterranean Sea. Sir C.V. Raman and his coworker K.S. Krishnan were finally able to observe Raman shift in liquids with much of the early work relying on visual inspection for the effect[29]. Since then, considerable progress has been made in Raman studies, with the invention of the laser and improvement in detection techniques allowing it to be widely used in the study of material composition and structure in molecular spectral analysis.

In Raman spectroscopy, the sample is irradiated by intense laser beams in the UV-visible region (with frequency υ_0) and the scattered light is observed in the direction perpendicular to the incident beam. The scattered light consists of two types: one, called Rayleigh scattering is strong and has the same frequency as the incident beam (υ_0). A very small concentration of the photons (1 in 10^5) undergoes inelastic scattering. This weak Raman scattering has frequencies ($\upsilon_0 \pm \upsilon_m$), where υ_m is the vibrational frequency of a molecule as well the type and strength of the bonds in the material which create phonons. The $\upsilon_0 - \upsilon_m$ and $\upsilon_0 + \upsilon_m$ lines are respectively called the Stokes and the anti-Stokes lines, respectively.

According to classical theory, Raman scattering can be explained as follows: The electric field strength (E) of the laser beam fluctuates with time (t) as show by:

$$E = E_0 \cos 2\pi \nu_0 t$$

where E_0 is the vibrational amplitude and υ_0 is the frequency of the laser. If a diatomic molecule is irradiated by this light, an electric dipole moment P is induced:

$$P = \alpha E = \alpha E_0 \cos 2\pi \nu_0 t$$

Here, α is a proportionality constant and is called polarizability. The polarizability of a molecule is usually anisotropic. The variation of the polarizability with direction can generally be given in the form of a polarizability tensor:

$$\alpha_{ij} = \begin{vmatrix} \alpha_{xx} & \alpha_{xy} & \alpha_{xz} \\ \alpha_{yx} & \alpha_{yy} & \alpha_{yz} \\ \alpha_{zx} & \alpha_{zy} & \alpha_{zz} \end{vmatrix}$$

If the molecule is vibrating with a frequency υ_m , the nuclear displacement q is written

$$q = q_0 \cos 2\pi \nu_m t$$

where q_0 is the vibrational amplitude. For small amplitude of vibration, the components of the polarizability tensor α_{ij} may be represented in the following approximate form

$$\alpha_{ij} = (\alpha_{ij})_0 + \left(\frac{\partial \alpha_{ij}}{\partial q}\right)_0 q_0 + ...$$

Here, $(\alpha_{ij})_0$ is the value of α_{ij} at the equilibrium position, and $\left(\partial \alpha_{ij} / \partial q\right)_0$ is the rate of change of α_{ij} in the course of the vibration, evaluated at the equilibrium position.

Combining the previous equations,

$$P = \alpha E_0 \cos 2\pi \nu_0 t$$

$$P = \alpha_0 E_0 \cos 2\pi \nu_0 t + \left(\frac{\partial \alpha}{\partial q}\right)_0 q E_0 \cos 2\pi \nu_0 t$$

$$P = \alpha_0 E_0 \cos 2\pi \nu_0 t + \left(\frac{\partial \alpha}{\partial q}\right)_0 q_0 E_0 \cos 2\pi \nu_0 t \cos 2\pi \nu_m t$$

$$P = \alpha_0 E_0 \cos 2\pi \nu_0 t + \frac{1}{2}\left(\frac{\partial \alpha}{\partial q}\right)_0 q_0 E_0 \left[\cos\{2\pi(\nu_0 + \nu_m)t\} + \cos\{2\pi(\nu_0 - \nu_m)t\}\right]$$

In the final expression above, the first term represents an oscillating dipole that radiates light of frequency υ_0 (corresponding to Rayleigh scattering), while the second term corresponds to the Raman scattering of frequency $\upsilon_0 + \upsilon_m$ (anti-Stokes) and $\upsilon_0 - \upsilon_m$ (Stokes). The expression also sets the condition for a vibration to be Raman active. If the $\left(\partial \alpha / \partial q\right)_0$ is zero, the vibration is not Raman-active. Thus to be Raman-active, the rate of change of polarizability with the vibration must not be zero.

5.3.2 Experimental

The UV micro-Raman measurements were carried out using the 325 nm line of a He-Cd laser as an excitation source. The scattered light was dispersed through a JYT64000 triple monochromator system attached to a liquid nitrogen cooled CCD

detector. The UV Raman spectra are recorded with a lateral and spectral resolution of 2.0 μm and 0.6 cm^{-1}, respectively. For variable temperature (78 – 500 K) Raman measurements, the samples were kept inside the liquid nitrogen cooled microscope cryostat (Oxford). The laser power on the sample surface was kept very low (<250 microwatt) to avoid laser heating of the organic crystal. The Raman spectral recording time on each sample spot was controlled to avoid prolonged UV light exposure. Rubrene crystals of various dimensions were tested throughout the extent of this study. Since rubrene crystal prefers to grow in the form of crystallites, the ab plane is the most accessible plane for the measurements. Gold electrodes were deposited on some of the samples through e-beam evaporation with a mean spacing of 200μm between the two electrodes. Very thin gold wires (50 μm in diameter) were attached to these gold pads using silver paste to enable the application of an electric field under the micro-Raman configuration.

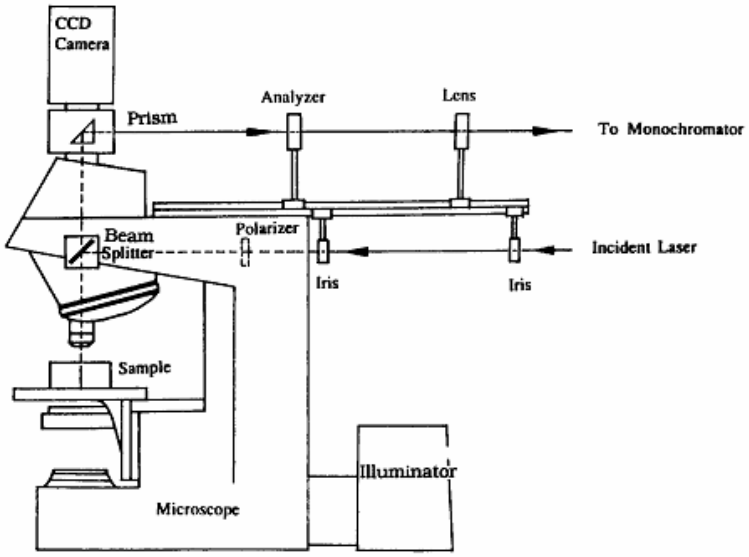

Figure 5.8: Schematic illustration of the Raman measurement setup utilised[30]

5.3.3 Rubrene Single Crystal Raman spectra

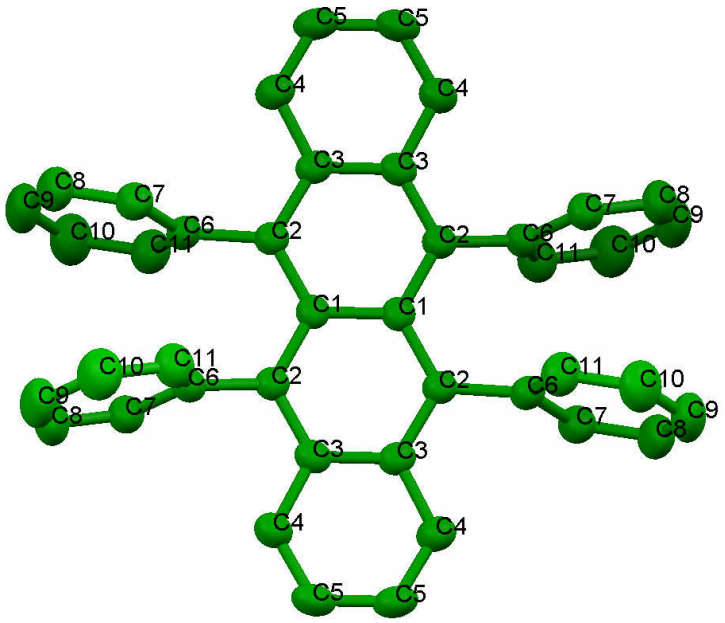

Figure 5.9: Geometrical structure of rubrene molecule extracted from single crystal diffraction[31]

Table 5.1 : Bond lengths and angles in rubrene molecule

Bond	Distance	Bond	Distance
C1-C1	1.453	C1-C2	1.428
C2-C3	1.405	C2-C6	1.494
C3-C4	1.435	C3-C3	1.428
C4-C5	1.354	C5-C5	1.391
C6-C7	1.386	C6-C11	1.388
C7-C8	1.373	C8-C9	1.371
C9-C10	1.370	C10-C11	1.378
Angles			
C4-C3-C2		121.83	
C3-C2-C6		116.01	
C1-C2-C6		123.36	
C2-C1-C2		121.72	

In Raman spectroscopy, the cross section for scattering depends in part on the scalar product of the incident light polarization, the Raman tensor for a particular mode as well as the polarization of the scattered light[32]. Thus the geometric arrangement of the experimental setup, the polarization of the incident and scattered light, and the symmetry of the crystal are therefore important parameters in determining the overall scattering cross section. Rubrene crystals have an orthorhombic structure with axes a=14.44 Å, b=7.18 Å, c=26.97 Å which crystallizes in the D_{2h}^{18} point group[33]. Consultation of the standard character tables [34]shows that this allows for vibrations of eight symmetry types: A_g, A_u, B_{1g}, B_{1u}, B_{2g}, B_{2u}, B_{3g}, and B_{3u}. This point group has a center of inversion and therefore only the gerade modes are Raman active. The Raman tensors for these allowed modes are[34]:

$$A_g = \begin{pmatrix} a & 0 & 0 \\ 0 & b & 0 \\ 0 & 0 & c \end{pmatrix} \qquad B_{1g} = \begin{pmatrix} 0 & d & 0 \\ d & 0 & 0 \\ 0 & 0 & 0 \end{pmatrix}$$

$$B_{2g} = \begin{pmatrix} 0 & 0 & e \\ 0 & 0 & 0 \\ e & 0 & 0 \end{pmatrix} \qquad B_{3g} = \begin{pmatrix} 0 & 0 & 0 \\ 0 & 0 & f \\ 0 & f & 0 \end{pmatrix}$$

In the backscattering configuration employed in this experiment, one can observe only the A_g and the B_{3g} modes. The relative intensities of the A_g and the B_{3g} mode should be dependent on the relative orientation of the crystal axes in the face of the crystallites and the incident polarization. In addition to the constraints posed by the D_{2h}^{18} symmetry of the rubrene crystal structure, the point group symmetry of the isolated rubrene molecule should also be taken into consideration. The isolated rubrene molecule has C_{2h} point group symmetry and also a point of inversion implying that the Raman active modes are the A_g and B_g modes[32].

During the course of our experiments, we have investigated polarization dependencies, studied the different facets of the rubrene crystal, temperature dependencies as well as explored the possible effects of application of an electric field. Figure 5.10 is a representative Raman spectrum obtained under ambient conditions.

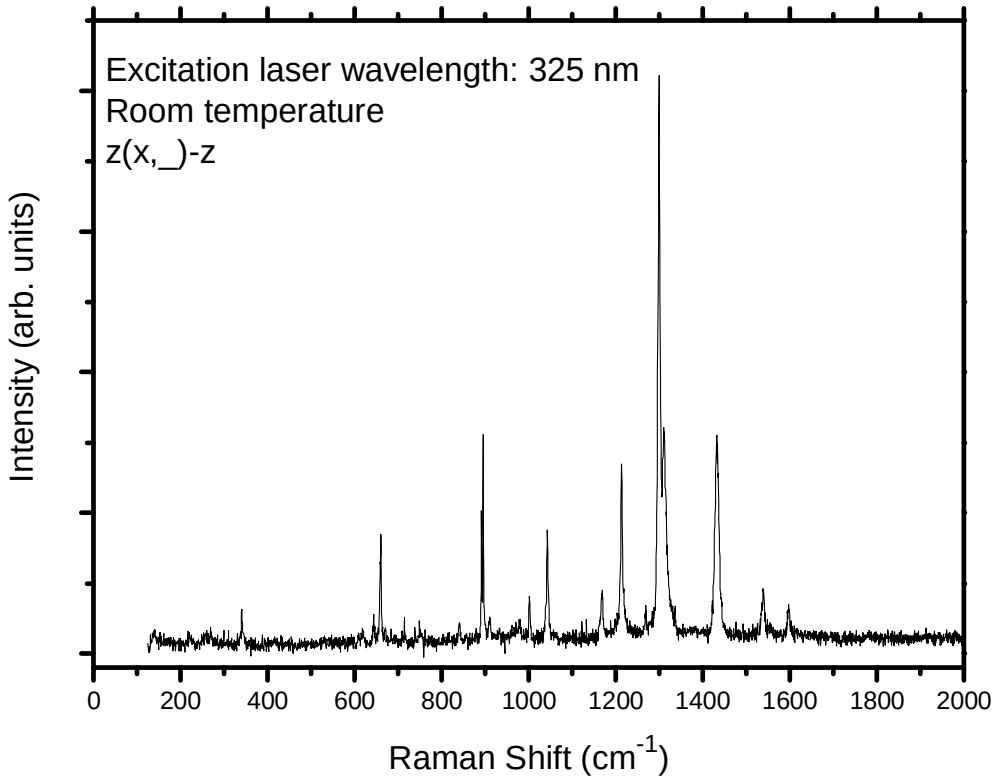

Figure 5.10: Representative room temperature Raman spectra measured on the surface of Rubrene crystals

A similar Raman study on the properties of the rubrene crystal has been performed by the group of Prof. Laurie McNeil at the University of North Carolina using resonant Raman techniques[35]. In this study, the authors were able to correlate all the observed Raman modes from the crystal to that originating from the molecule alone. This had enabled them to extend the hypothesis that the intermolecular coupling in rubrene

crystals is surprisingly weak. Our results are in general agreement with that obtained by the aforementioned group.

Table 2 compares the experimentally observed peaks with the theoretically calculated Raman modes of the rubrene molecule extracted from reference [35]. Hartree-Fock method was used for structural optimization and the density functional theory (DFT) B3LYP method was used to calculate the Raman frequencies. Since the current experiment employed a UV laser as the source of excitation, many of the modes predicted by the theoretical simulation were not detected during our experiment.

Table 5.2: Comparison of theoretically calculated Raman modes to experimentally measured Raman modes in this experiment and in the literature

Symmetry	Theory[35] cm^{-1}	Measured by Resonance Spectrsocopy[35] cm^{-1}	Measured in current experiment cm^{-1}	% Difference with theory
B_g	72.2	73.7	No	Undefined
B_g	80.3	85.7	No	Undefined
A_g	83.2	107	No	Undefined
B_g	96.5	120.3	No	Undefined
A_g	128.6	141.7	140	8.9%
A_g	205.3	204.4	No	Undefined
A_g	254.4	236.6	258	1.4%
A_g	326.4	342	341	4.5%
B_g	385.4	393	No	Undefined
B_g	467.7	470	No	Undefined
B_g	514.1	517	No	Undefined
B_g	575.3	613.7	No	Undefined
	Not predicted	Not measured	661	Undefined
A_g	872.8	896.3	895	2.6%
A_g	977.7	1003.09	1002	2.5%
A_g	1026.6	1046	1042	1.5%
A_g	1183.9	1163	1168	-1.2%

	Not predicted	Not measured	1213	Undefined
B_g	1251.1	1268.2	1268	1.3%
A_g	1295.1	1299.9	1300	0.3%
A_g	1307.1	1310.9	1311	0.3%
B_g	1330.5	1315.7	1336	0.4%
A_g	1420.8	1432.3	1431	0.7%
B_g	1487.7	1519.9	No	Undefined
A_g	1530.4	1539.9	1540	0.62%
A_g	1592.3	1616.8	1596	0.23%

In our experiments, we have been able to detect two new Raman signals at 1213 cm^{-1} and 661 cm^{-1} using the 325 nm Raman excitation which is not predicted by the theoretical calculations employed and were also not measured in the previous work by Weinberg et al[35]. The location of these modes at such high wavenumbers rules out the possibility that they are linked to intermolecular modes. At the time of writing this thesis, a DFT simulation on an isolated rubrene molecule with an experimentally determined geographical structure [31] is being pursued to probe the source of these Raman modes. Figure 5.9 and Table 5.1 display the starting geometry of the calculation. Another possibility for the origin of these modes could be the presence of rubrene peroxide on the surface of the crystal[36]. Due to the fact that a UV laser is employed in these measurements, the spectra recorded are very sensitive to the chemical species present on the top surface. The O-O stretching mode in endoperoxides ranges from 650 cm^{-1} to 800 cm^{-1} depending on the type of peroxides[37].An additional consequence of a measurement which utilises a UV laser is the possibility of photo-oxidation on the rubrene surface which would also increase the concentration of the rubrene peroxide species. More details on the presence of rubrene peroxide on the surface of the rubrene crystal and its consequences will be discussed in Chapter 6. The absence of these Raman modes in the work by Weinberg et al may be related to the fact that the wavelength employed in their experiment (653.55nm) primarily measured the rubrene crystal bulk

The dependence of polarization on the Raman spectra of Rubrene crystals were measured by changing the sample alignment on the ab plane. Only high wavenumbers were measured during this experiment due to the high noise to signal ratio at the low wavenumbers. Table 9 holds the normalized intensities of the dominant peaks of the Raman spectra for the three different sample alignments. The normalization was done with respect to the strongest peak in the spectrum (at 1295 cm^{-1}). As mentioned previously, the incident laser is vertically polarized and all the Raman measurements are carried out in the z(x_)-z back scattering configuration. We tried to perform polarization measurements such as z(xx)-z and z(xy)-z geometries but we did not detect any significant changes. The 45 degree rotation to make z(x, x+y)-z also did not result in any significant changes. The Raman modes with the A_g symmetry were insensitive to the changing of the polarization while the lone Raman mode with the B_g symmetry was more prominent along the b axis rather than the a axis.

Table 5.3: Normalised intensities for different incident polarization showing B_g variation.

Symmetry	Theory cm^{-1}	z(xx)-z (cm^{-1})	Rel. Intensity	z(xy)-z (cm^{-1})	Rel. Intensity	z(x,x+y)-z (cm^{-1})	Rel. Intensity
		660	0.093	660	0.12	660	0.095
A_g	872.8	894	0.36	894	0.38	894	0.38
A_g	977.7	1002	0.068	1000	0.086	1001	0.08
A_g	1026.6	1042	0.17	1042	0.21	1042	0.19
A_g	1183.9	1168	0.09	1164	0.10	1166	0.09
		1213	0.33	1213	0.36	1213	0.32
B_g	**1251.1**	**1268**	**0.082**	**1268**	**0.054**	**1268**	**0.061**
A_g	1295.1	1299	1	1299	1	1299	1
A_g	1307.1	1311	0.45	1311	0.47	1311	0.44
A_g	1420.8	1433	0.29	1431	0.24	1431	0.24
A_g	1530.4	1540	0.10	1540	0.08	1540	0.08
A_g	1592.3	1596	0.08	1597	0.066	1597	0.067

5.3.4 Raman spectra for the different facets of the crystal

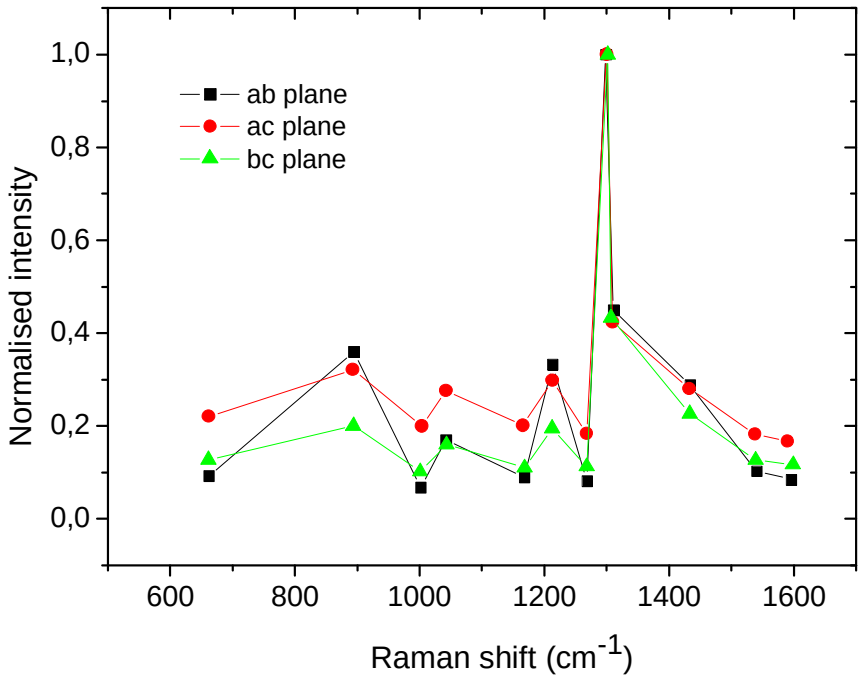

Figure 5.11: Exploration of the different facets of the rubrene crystal indicating no dependency on the Raman spectra

The different facets of the rubrene crystal were studied in order to explore the presence of the intermolecular modes completely. As mentioned before, Raman spectra are also determined by the symmetry of the crystal plane on which the excitation is incident. In this case, no new peaks were measured during the experiment.

5.3.5 Temperature dependency

Temperature will affect a crystal in two distinct manners, typically referred to as implicit and explicit temperature effects. The explicit temperature effect is related to the phonon occupation number that occurs with changes in temperature. The implicit

temperature effect quantifies the change in vibrational frequency due to thermal expansion and contraction of the crystal lattice with temperature. Normally lowering the temperature of a material will cause Raman lines both to narrow and to shift to higher frequency. Due to the higher sensitivity of weak van der Waals forces to the temperature rather than the stronger covalent bonds, the intermolecular modes will vary disproportionately when exposed to changes in temperature compared to intermolecular modes. During the course of the experiment, few Raman modes in the low wavenumbers were measured and thus the effect of temperature on these low modes could not be studied clearly.

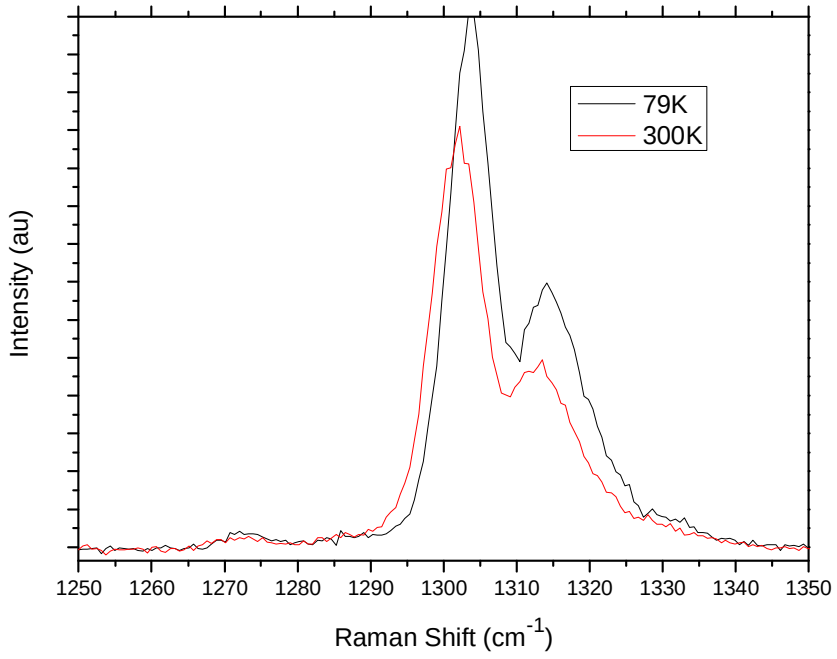

Figure 5.12: Raman intensities for the two strongest modes measured at 79K and 300K

Table 5.4: Peak positions for rubrene modes at 300K and 79K

Symmetry	Position (cm^{-1}) 300K	Position (cm^{-1}) 79K	Difference	% Difference
A_g	340.4	342	1.6	0.47
Unknown	661.79	662.87	1.08	0.16
A_g	896.08	897.63	1.55	0.17
A_g	1003	1005.19	2.19	0.22
A_g	1044	1046.7	2.7	0.26
A_g	1168	1169.8	1.8	0.15
Unknown	1215.54	1217	1.46	0.12
B_g	1271.54	1272.34	0.8	0.06
A_g	1301.8	1303.89	2.09	0.16
A_g	1313.14	1314.12	0.98	0.07
A_g	1434.3	1435.71	1.41	0.10
A_g	1539.8	1542.9	3.1	0.20
A_g	1599.26	1600.2	0.94	0.06

Figure 5.12 and Table 5.4 confirms the shifting of the Raman modes to higher values with a decrease of temperature. However the degree of shifting is low as compared to similar measurements performed on other organic semiconductors[38]. The relative insensitivities of the measured Raman modes to the temperature are again a clear indication that the primary modes observed during the experiment are intramolecular in nature.

5.3.6 Electric field dependencies

In-situ measurements of the vibrational spectra of pentacene thin films under a transistor configuration have been pursued by a few groups[1, 39, 40]. This has proven to be a valuable tool in identifying microstructural changes in the pentacene layer on application of an electric field. Further effects of applied electric field on organic thin films include downshifts of the D and G modes and in reduction of their intensity based on carbon nanotubes.[41] On the application of a source drain electric field in pentacene transistors, Raman measurements indicated an enhacement of the intermolecular interactions. We have deposited gold electrodes through e-beam

evaporation on the surfaces of multiple rubrene crystals in order to apply an electric field across the top surface of the crystal. In order to apply voltages in the micro-Raman configuration, fine gold wires were delicately attached to the electrodes (typically spaced at 200μm) using silver paste. All the electrical voltages were applied using a Keithley 2612. The spacing between the electrodes were about 200 micron and voltages up to 200V were applied ($E \leq 10^6$ V/m). Again, there were no shifts on application of the voltage Raman peaks indicating the complete insularity of the measured spectra and the vibrational states of the rubrene molecule to applied electric fields.

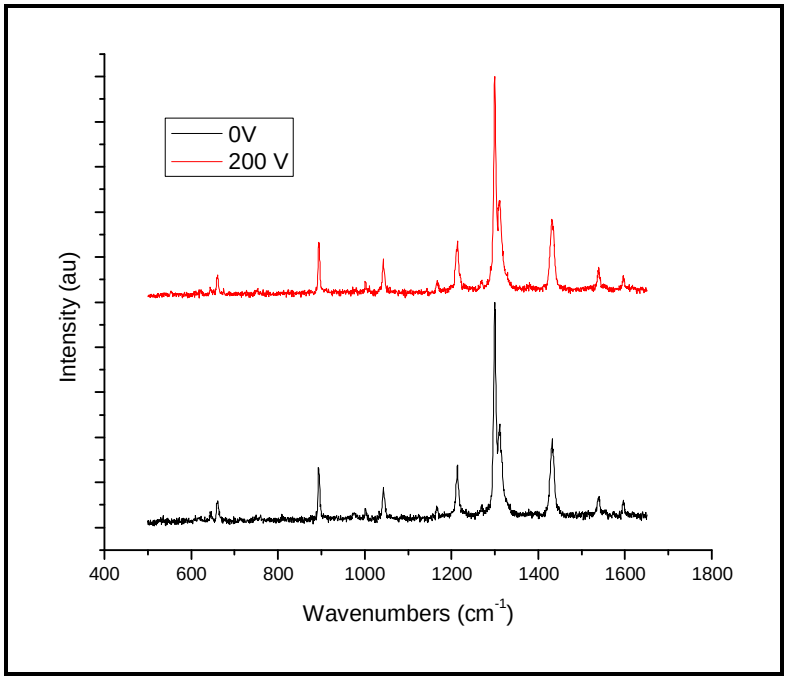

Figure 5.13: Insensitivity to applied electric field

In conclusion, this chapter discussed the various optical spectroscopies performed on rubrene during the extent of this thesis. Photoluminescence spectroscopy revealed the fundamental excitations of the rubrene molecule polarized along the different axes of the molecule. The photoluminescence data also reveals that the crystal field effects are very weak in rubrene with the absence of Davydov splitting and related effects.

Raman spectroscopy was performed on rubrene single crystals in order to probe the intermolecular coupling which is important for the existence of high charge carrier mobility. UV-Raman spectroscopy did not reveal the existence of Raman modes indicative of intermolecular coupling but instead revealed the possible presence of Raman modes associated with the presence of rubrene endoperoxide. These modes were not detected in the previous investigations due to the surface insensitive nature of the excitations used.

5.4 References

1. B. A. Paez, M. Bartzsch, G. Salvan, R. Scholz, T. U. Kampen and D. R. T. Zahn, Proceedings of SPIE - The International Society for Optical Engineering, 2003.
2. J. B. Birks, ed., *Organic Molecular Photophysics*, John Wiley & sons, London, 1973.
3. R. A. Baxter, E. A. Braude, B. Lythgoe, L. N. Owen, G. T. Newbold, F. S. Spring and W. A. Waters, *Annual Reports on the Progress of Chemistry*, 1945, **42**, 123.
4. A. K. Dutta, T. N. Misra and A. J. Pal, *Solid State Communications*, 1996, **99**, 767-771.
5. X. Zeng, D. Zhang, L. Duan, L. Wang, G. Dong and Y. Qiu, *Applied Surface Science*, 2007, **253**, 6047-6051.
6. H. G. Löhmannsröben, *Applied Physics B: Lasers and Optics*, 1988, **47**, 195-199.
7. G. M. Badger and R. S. Pearce, *Spectrochimica Acta*, 1951, **4**, 280-283.
8. R. Jankowiak, K. D. Rockwitz and H. Bassler, *Journal of Physical Chemistry*, 1983, **87**, 552-557.
9. M. Kytka, A. Gerlach, F. Schreiber and J. KovaC, *Applied Physics Letters*, 2007, **90**, 131911-131913.
10. L. Zhao, G. Yang, Z. Su, C. Qin and S. Yang, *Synthetic Metals*, 2006, **156**, 1218-1224.
11. S. Tavazzi, A. Borghesi, A. Papagni, P. Spearman, L. Silvestri, A. Yassar, A. Camposeo, M. Polo and D. Pisignano, *Physical Review B (Condensed Matter and Materials Physics)*, 2007, **75**, 245416-245415.
12. N. Sai, M. L. Tiago, J. R. Chelikowsky and F. A. Reboredo, *Physical Review B (Condensed Matter and Materials Physics)*, 2008, **77**, 161306-161304.
13. H. Najafov, I. Biaggio, V. Podzorov, M. F. Calhoun and M. E. Gershenson, *Physical Review Letters*, 2006, **96**, 056604.
14. S. Tavazzi, L. Silvestri, M. Campione, A. Borghesi, A. Papagni, P. Spearman, A. Yassar, A. Camposeo and D. Pisignano, *Journal of Applied Physics*, 2007, **102**, 023107.

15. T. T. Nakashima and H. W. Offen, *The Journal of Chemical Physics*, 1968, **48**, 4817-4821.
16. A. S. Davydov, *Theory of Molecular Excitons*, 1971.
17. J. L. Bredas, J. Cornil, D. Beljonne, D. A. dos Santos and Z. Shuai, *Acc. Chem. Res.*, 1999, **32**, 267-276.
18. Z. G. Soos, S. Ramasesha and D. S. Galvão, *Physical Review Letters*, 1993, **71**, 1609.
19. T. N. Singh-Rachford and F. N. Castellano, *J. Phys. Chem. A*, 2008, **112**, 3550-3556.
20. A. P. Darmanyan, *Bulletin of the Academy of Sciences of the USSR Division of Chemical Science*, 1983, **31**, 1679-1682.
21. M. Kaschke, N. P. Ernsting and F. P. Scha?fer, *Optics Communications*, 1988, **66**, 211-215.
22. H. G. Löhmannsröben, *Applied Physics B Photophysics and Laser Chemistry*, 1988, **47**, 195-199.
23. T. Wilson, *Journal of the American Chemical Society*, 1969, **91**, 2387-2388.
24. O. Mitrofanov, D. V. Lang, C. Kloc, J. M. Wikberg, T. Siegrist, W.-Y. So, M. A. Sergent and A. P. Ramirez, *Physical Review Letters*, 2006, **97**, 166601-166604.
25. N. E. Gruhn, D. A. da Silva Filho, T. G. Bill, M. Malagoli, V. Coropceanu, A. Kahn and J. L. Bredas, *Journal of American Chemical Society*, 2002, **124**, 7918-7919.
26. R. A. Marcus, *Reviews of Modern Physics*, 1993, **65**, 599-610.
27. R. Silbey, J. Jortner, S. A. Rice and J. M. T. Vala, *The Journal of Chemical Physics*, 1965, **42**, 733-737.
28. A. Smekal, *Die Naturwissenschaften*, 1923, **11**, 873-875.
29. C. V. Raman and K. S. Krishnan, *Nature*, 1928, **121**.
30. G. Smulevich and T. G. Spiro, *Methods in Enzymology*, 1993, **226**, 397-408.
31. O. D. Jurchescu, A. Meetsma and T. T. M. Palstra, *Acta Crystallographica Section B: Structural Science*, 2006, **62**, 330-334.
32. D. C. Harris and M. D. Bertolucci, *Symmetry and Spectroscopy*, Oxford University Press, New York, 1978.

33. D. E. Henn, W. G. Williams and D. J. Gibbons, *Journal of Applied Crystallography*, 1971, **4**, 256-&.
34. G. Turrell, *Infrared and Raman Spectra of Crystals*, Academic Press, London, 1972.
35. J. R weinberg-Wolf, L. E. McNeil, S. Liu and C. Kloc, *Journal of Physics-Condensed Matter*, 2007, **19**.
36. D. Kafer and G. Witte, *Physical Chemistry Chemical Physics*, 2005, **7**, 2850-2853.
37. P. Di Mascio, E. J. H. Bechara and J. C. Rubim, *Applied Spectroscopy*, 1992, **46**, 236-239.
38. A. D. Esposti, M. Fanti, M. Muccini, C. Taliani and G. Ruani, *The Journal of Chemical Physics*, 2000, **112**, 5957-5969.
39. H. L. Cheng, W. Y. Chou, C. W. Kuo, Y W. Wang, Y. S. Mai, F. C. Tang and S. W. Chu, *Advanced Functional Materials*, 2008, **18**, 285-293.
40. H. L. Cheng, W. Y. Chou, C. W. Kuo, F. C. Tang and Y. W. Wang, *Applied Physics Letters*, 2006, **88**, 161918-161913.
41. G. Fanchini, H. E. Unalan and M. Chhowalla, *Nano Lett.*, 2007, **7**, 1129-1133.

Chapter 6

Extrinsic effects on charge conducting properties of rubrene

In the discussion of the properties of organic molecular crystals in Chapter 2, only the intrinsic properties were focused on. The intrinsic properties of the molecular crystals are determined by the HOMO, LUMO levels of the molecule as well as the order and arrangement of these molecules in their lattices. While designing the practical application of organic semiconductors like rubrene, it is very important to consider extrinsic effects on their electrical properties. In chapter 3, we have briefly looked at the various defects that can be created on the surface of the molecular crystal during the formation of devices that could have a debilitating effect on their intrinsic properties. Chapter 4, which dealt with the photocurrent properties of the rubrene free space dielectric transistor, further drove in the importance of extrinsically created oxygen states which lead to the observation of phenomena like steady state photoconductivity associated with the localization of charge carriers in traps. This chapter consolidates various experiments done throughout this thesis which showed the influence of extrinsic factors (especially oxygen induced effects) on the charge conducting properties of rubrene.

6.1 Common extrinsic effects in organic devices

Molecules in organic solids interact weakly as a specific molecule's unoccupied molecular orbit (LUMO) and highest occupied molecular orbit (HOMO) are independent of the surrounding matrix. A trap is formed when the HOMO or LUMO of a dopant molecule is positioned in the gap of the host molecules. Structural defects occur when HOMO/LUMO levels vary from molecule to molecule of the same species and mismatch occurs. The exact

energy position is not only determined by the chemical structure but also by the electronic polarization of the surrounding molecules. An additional source of variation in the electronic properties of an organic solid is the structural imperfections that lead to fluctuations, causing the states in the tail ends of the distribution to form trap states. Chemical defects include incorporated impurities during fabrication process or thin film deposition.

An inhomogenity in the crystal lattice which leads to an electrical defect can lead to the localization of charge carriers. A passing charge carrier prefers to occupy this lower energy state and the trap localizes the charge carrier at its site. Considering the activation energy that is needed to free the charge carrier, traps can be split in shallow traps, when the activation energy is in the order of kT, and deep traps, when the activation energy is outside the range of thermal excitation. Shallow traps can capture a carrier for a time period shorter than the transit time. Deep traps capture carriers for a time period longer than the transit time. Shallow traps are formed by distribution of energy levels around the limits of the conduction and valence bands.

Another dimension of the extrinsic effects in organic semiconductor is doping. The presence of external chemical entities in the molecules constituting the film or the crystal can change the properties of the solid especially the conductivity. The utility of conventional inorganic semiconductors in the myriad devices depends critically on the ability to precisely dope these materials n-type (electron conducting) or p-type (hole conducting) with high spatial resolution. In contrast, the quantitative study of the doping (intended or unintended) of organic semiconductors is still growing [1-6]. The basic principles of chemical doping in organic semiconductors are similar to those in inorganic materials: Mobile carriers are generated by electron donors or acceptors. In organics, one has to add constituents, which either donate electrons to the lowest unoccupied orbital (LUMO) states (n-type doping) or remove electrons from the highest occupied orbital (HOMO) states to generate holes (p-type doping). Several results on molecular doping have been reported in literature in the last decades. For instance,

phthalocyanines have been doped by adding organic acceptor molecules like orthochloranil, tetracyano-quinodimethane (TCNQ), or dicyano-dichloroquinone (DDQ) among others[7-10]. In addition to doping by the mixing of molecular components, increases in the conductivity of organic layers have also been observed when molecules are exposed to strongly oxidising gases like bromine or iodine and metals like lithium, cesium or strontium[11-14]. A strong factor that prevents the utilisation of the gases or metals as dopants in order to create stable devices is their propensity to diffuse. In a p-n junction, with n-type dopants on one side and p-type on the other, there is a strong chemical gradient that tends to randomize the dopants. The electric field also drives the dopants towards intermixing. If the dopants are mobile, the electrical properties of the material will change with time, voltage and other factors resulting in the disappearance of pn junctions.

Very recently Podzorov et al[15] have shown that the conductivity on the surface of the rubrene crystal can be modulated by electronic functionalization with self-assembled monolayers. The reason behind this SAM-induced conductivity is not due to chemical doping, which would require mixing of dopants into the bulk of organic material, but rather it is due to a ground-state charge transfer at the interface between the organic semiconductor and the SAM. The degree of the charge transfer and, therefore, conductivity of SAM-functionalized samples depend on the electron-withdrawing ability of the monolayers with organosilanes of larger fluorine content inducing a higher conductivity. Strong surface binding in combination with the charge transfer creates a stable, well-aligned layer of negatively charged SAM molecules, immobilized above the SAM–crystal interface, and a corresponding layer of mobile holes below the interface.

Thus it can be clearly concluded that in addition to the intrinsic properties of the organic semiconductors, extrinsic factors especially the presence of foreign compounds in the bulk or the surface of the organic layers and crystals can modulate the measured properties significantly. This is particularly pertinent for devices like transistors based on the rubrene

single crystal, where the gate modulated channel exists on the surface of the crystal. From the point of view of utilising rubrene transistors in practical applications, the stability of the measured properties to atmosphere especially oxygen is important. In the succeeding pages, we show the presence of oxidation in rubrene solution monitored by optical spectra, the presence of rubrene peroxide on the surface of the crystals by photoluminescence measurements and X-ray photoelectron spectroscopy. The effect of the oxidation on the surface conductivity is described, followed by the effect of oxidising gases on surface conductivity.

6.2 Oxidation of rubrene in solution

Rubrene (Sigma Aldrich) was dissolved in cyclohexane at a concentration of about 0.01mg/ml. Prior to dissolution, the solvent was bubbled with argon in order to remove all dissolved oxygen. The absorption spectra and the fluorescence of the solution were measured and revealed characteristics detailed in chapter 5 of the thesis. The solution of rubrene was exposed to UV light at 365 nm for 2 hours and measured again with no change in optical absorption spectra. Injecting a few bubbles of air into the solution and exposing it again to the UV light for a similar period of time resulted in visible changes.

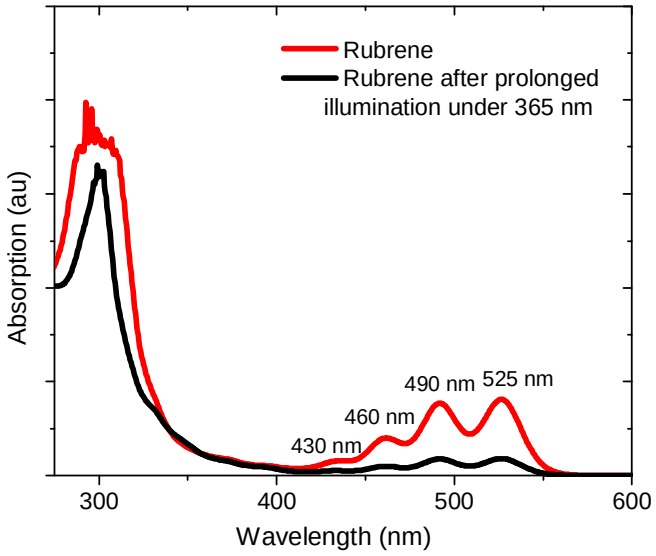

Figure 6.1: Absorption spectra of rubrene solution measured over time indicating the reduction in rubrene concentration over time due to oxidation

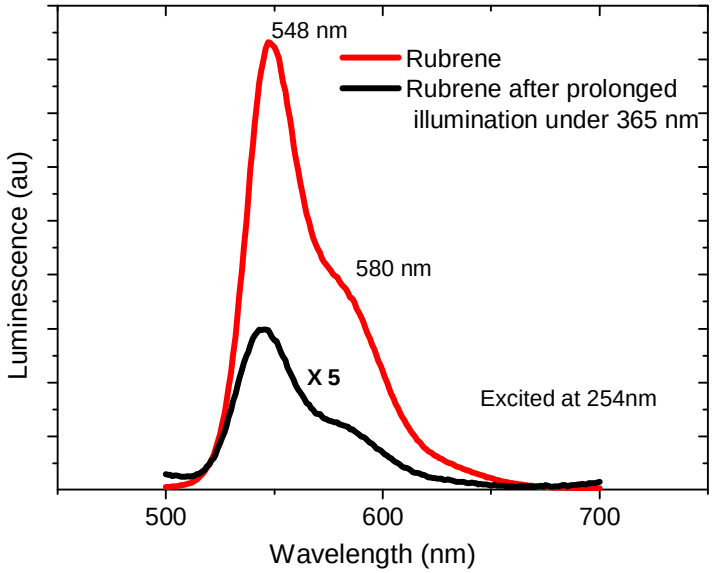

Figure 6.2: Fluorescence measurements indicative of the loss of conjugation associated with rubrene.

The changes are visible to the eye with the solution becoming colourless. The absorption peaks associated with the rubrene start to decrease indicating a reduction in the concentration of the rubrene in the solution. The luminescence reduces drastically as well. Both these results

indicate a loss of conjugation associated with the rubrene molecule. Previous researchers who have observed similar phenomenon with rubrene molecule attribute the changes to the formation of rubrene peroxide which is colourless in nature[16-19]. The reaction scheme has been given by[20]:

$$\mathbf{R} \xrightarrow{h\nu} {}^1\mathbf{R}$$

$${}^1\mathbf{R} + \mathbf{O}_2 \longrightarrow {}^3\mathbf{R} + {}^1\mathbf{O}_2(\mathbf{O}_2)$$

$${}^3\mathbf{R} + \mathbf{O}_2 \longrightarrow \mathbf{R} + {}^1\mathbf{O}_2$$

$$\mathbf{R} + {}^1\mathbf{O}_2 \longrightarrow \mathbf{RO}_2$$

Another possibility for the formation of stable rubrene endoperoxide is the direct photooxygenation of rubrene where two rubrene molecules take part in the reaction[21]. Having established the possibility of oxidation in rubrene solutions, it is now necessary to move the studies to the surface of rubrene crystal in order to detect oxidative effects.

6.3 Photoluminescence measurements on rubrene crystal surface

Chapter 5 has discussed in detail, the luminescence properties of the different rubrene crystal facets. The spectra measured in figure 5.7 are of freshly grown crystals when the possibility of oxidation is the least. Shown below is the photoluminescence spectrum of the ab plane of crystals which were stored in the ambient conditions. It is clear that the luminescence spectra shown below display an additional excitation at 650 nm absent from the ab spectra of the fresh crystals.

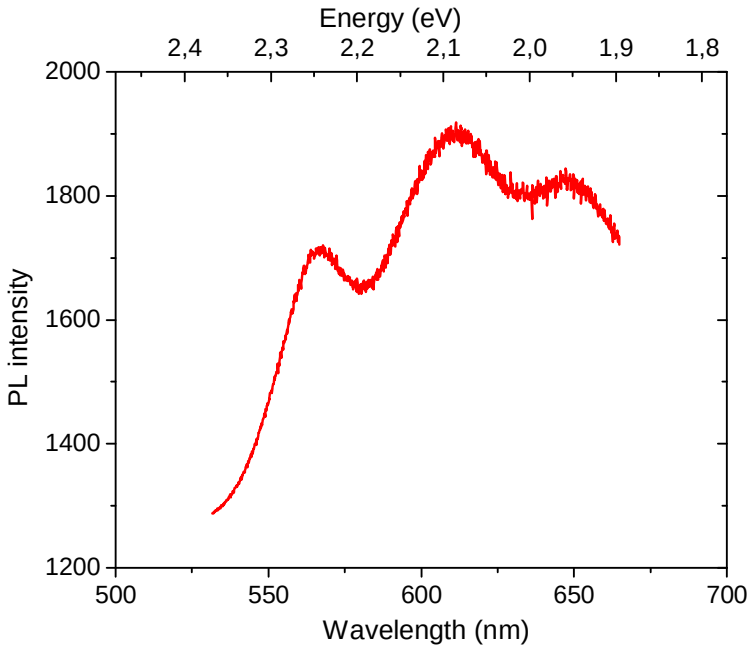

Figure 6.3: Photoluminescence spectra of rubrene crystals stored in ambient conditions indicating presence of an additional peak at 650nm

This confirms studies by Mitrofanov et al[22, 23], who have seen the development of this PL signature on heating freshly grown rubrene crystal in an atmosphere of oxygen. Two photon luminescence measurements which were able to sample the crystal at various depths showed that this oxygen induced peak is present only at the top surface. The authors have attributed this PL peak as induced by the formation of a rubrene endoperoxide on the rubrene crystal surface[24].

6.4 X-ray Photoelectron Spectroscopy

In a bid to investigate the effects of oxygen on the surface of rubrene crystal, surface analysis was performed using X-ray Photoelectron Spectroscopy (XPS). The phenomenon is based on the photoelectric effect outlined by Einstein in 1905 where the concept of the photon was used to describe the ejection of electrons from a surface when photons impinge upon it. When a high energy photon (in the X-ray region of the electromagnetic spectrum) strikes a surface,

photo-ionisation occurs. The beam of X-rays produce photo-ionisation and the kinetic energy of the ejected photoelectrons is measured by passing the electrons through some kind of energy analyser (either a time-of-flight or magnetic analyser or electrostatic energy analyser). The equation which describes the energetics of the photoionisation process is

$$h\nu = E_B + E_K$$

where hν is the incident X-ray photon energy, E_B is the binding (ionisation) energy of the electron from a particular energy level, and E_K is the kinetic energy of the ejected photoelectron. A measurement of the kinetic energy of the photoelectron allows for the determination of the binding energy and hence elemental identification and chemical information on the surface materials.

For the surface analysis, rubrene crystals which were stored in ambient conditons were selected to check for a naturally formed endoperoxide layer. This measurement was done by Kratos AXIS spectrometer (UK) with the monochromatic Al K-alpha X-ray radiation at 1486.71 eV. The base vacuum in XPS analysis chamber was about 1x10−9 Torr. All spectra were calibrated using C1s at 284.6 eV as a reference. Pass energy was kept at 40 eV and the step size 0.1eV. The O1s core level binding energy was monitored. Surface layers were etched using Ar^+ ions to conduct a depth study. Each etch cycle corresponds to a calibrated value of 3nm on silicon dioxide. Organic crystals being softer would have a higher etching depth. Figure 6.4 clearly indicates the strong O1s peak which is strongly observed on the top surface prior to etching, is still visible after the first etch cycle and is still visible weakly in the two subsequent etched surfaces. There are possibly two sources for this signal at 532.6 eV. It could correspond to surface adsorbed oxygen [25] with subsequent traces found on the layers below due to diffusion into the bulk. Diffusion of oxygen into C_{60} molecular crystals have been observed previously.[26] The other source for the signal could be the presence of the rubrene endoperoxide on reaction with oxygen. The binding energy of the O1s level present in a C-O bond (created during endoperoxide formation) is also located at 532.6 eV. [27]

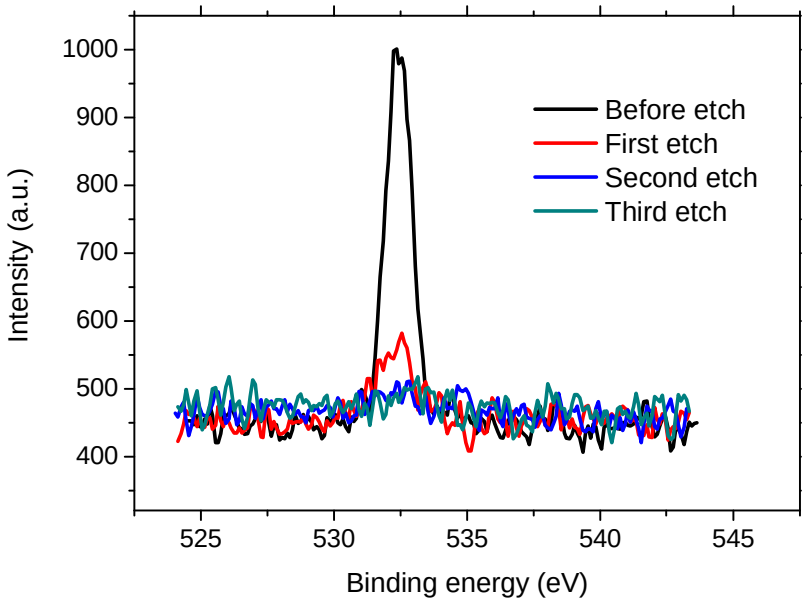

Figure 6.4: XPS spectrum of the rubrene crystal surface with an oxygen peak indicative of the presence of rubrene peroxide

Thus there are many indications to the presence of naturally formed rubrene peroxide on the surface of the rubrene crystals. Additional proof for the presence of rubrene endoperoxide has come from Witte et al who have detected the rubrene peroxide molecule (with concentration upto 1%) at a depth of 50nm through LDI-TOF-MS although it has to be noted that the process of crystal growth differs in this case.[28]. Due to the fact that the rubrene endoperoxide has a different conformation as compared to the rubrene molecule, the molecule cannot be easily accommodated in a crystalline network. This would mean that the sites for the creation of rubrene endoperoxide would be the defects like vacancies and dislocations in rubrene crystal. Now that the presence of rubrene endoperoxide has been established, its influence on charge conduction can be studied.

6.5 In-situ photo-oxidation measurements

As discussed previously, the mechanism for the formation of rubrene endoperoxide requires the input of photo-excitation. Utilising the same measurement setup previously employed for

raman measurement, we monitored the current flowing on the rubrene crystal surface. Gold electrodes were deposited through e-beam evaporation and fine 50 μm gold wires were attached to them using silver epoxy. The laser setup is equipped with an xy scanner that allows precise movements in the order of a micron. Laser exposures were made at points at a distance of 3 microns for from each other for 6 minutes each while scanning from one electrode to another.

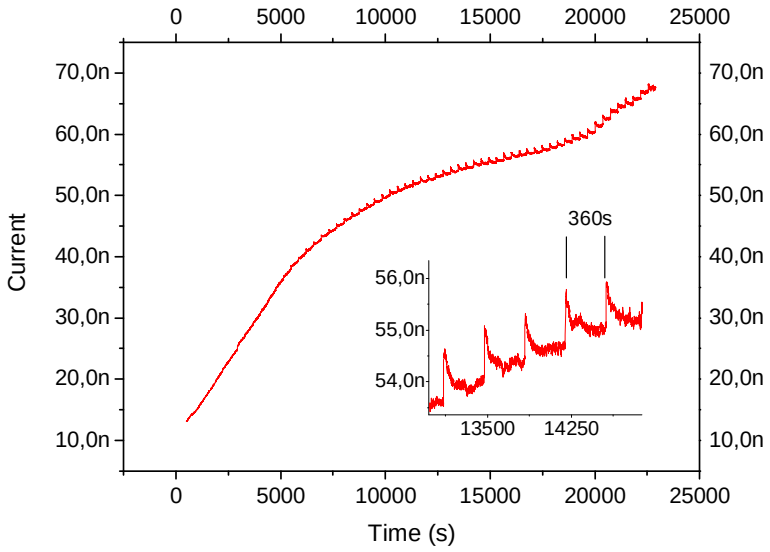

Figure 6.5: Surface current measured over time during spatial scan. Inset shows a blown up view of the current profile clearly identifying the time spent at each point.

Figure 6.5 shows the surface current measured on application of 100 V across a gap of 200 micron while continuously scanning the laser spot from one electrode to the other. Data from the electrodes are not displayed to avoid confusion. As is evident from the graph, the net current flowing on the rubrene surface increases with time. As the laser spot is scanned across the surface of the crystal, photo-oxidation occurs in the area beneath it. The photo-oxidised rubrene is more conductive than the unoxidised area. Since the overall area of the photo-oxidised rubrene in the sample is increasing with time, the current follows the trend and

increases as well. The inset of the graph clearly shows the current dynamics at each spot illustrating the sensitivity of the data to the location of the illumination.

6.6 Source of conductivity modulation induced by oxygen effects

The previous sections of this chapter have shown the existence of oxygen induced compounds on the surface of the rubrene crystal and that the result of these oxygen induced effects is an increase in the surface conductivity. The presence of the oxygen related photoluminescence band at 650nm is an indication of the presence of a state located 0.25 eV below the lowest 0-0 transition[22]. A study of the density of states in rubrene single crystals performed by temperature dependent space charge limited spectroscopy has also revealed the presence of a deep level acceptor state at 0.27 eV in agreement with the PL data[29]. Thus it can be tentatively stated that these acceptor centers capture electrons leaving free holes in the valence band. This increases the dark conductivity of rubrene and goes towards explaining the predominant number of reports of unipolar conductivity in rubrene crystals. Previously, our group had performed scanning tunnelling spectroscopy on the surface of the rubrene crystals and had revealed unipolar conduction[30]. Electron trapping in these deep acceptor states could be the reason for this observation. The presence of these states can also increase the photoconductivity by acting as centers for exciton splitting. In organic semiconductors, where the exciton binding energy is high, these deep level acceptor states can trap electrons resulting in a free hole that can contribute to the conductivity. This is consistent with the observation of persistent photoconductivity and related phenomenon discussed in Chapter 4.

6.7 Influence of nitrogen dioxide on rubrene transistors

In addition to the influence of oxygen on the electrical characteristics of the rubrene crystal, the exposure of an oxidising gas like NO_2 was also studied. These measurements were performed by Keke Zhang at Nanyang Technological University, Singapore. A modified air-

gap configuration was employed in these experiments whereby rubrene crystals were adhered on to gold electrodes which were a part of a bottom contact substrate with silicon dioxide as the dielectric. Nitrogen dioxide was introduced as a mixture with nitrogen with the concentration of nitrogen dioxide in the mixture precisely controlled using mass flow meters.

Figure 6.6 reveals the log-scale characteristics of the rubrene air gap transistor on exposure to ppm levels of nitrogen dioxide. The drain current increases by more than one order of magnitude at V_g=0 V from 4.4 X 10^{-10} A to 1.3X 10^{-8} A.

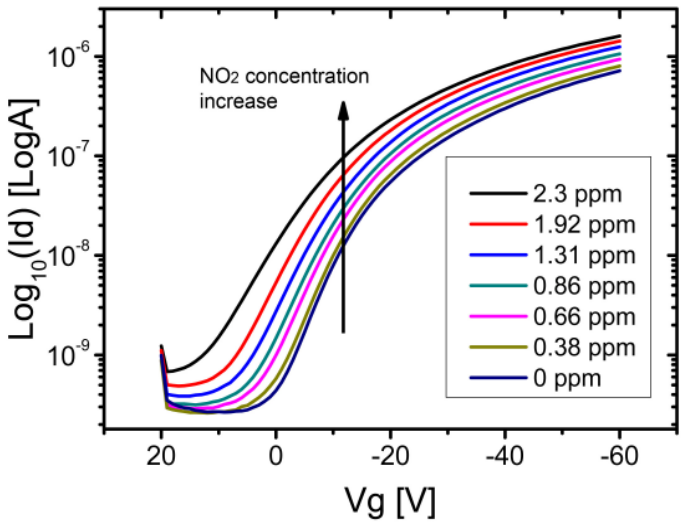

Figure 6.6:Log-scale transfer characteristic of the identical rubrene single crystal OFET under different NO_2 concentration at Vd=-60 V.

An important factor to note is that the shape and slope of the transfer curve does not change significantly on exposure to NO_2. This is a strong indication that the variations in the drain current are caused due to an increase in the charge carrier density rather than the mobility of the holes.

Time-resolved source-drain current under periodic NO_2 exposure and N_2 purge has also been studied. The transistor was in accumulation mode with an applied gate voltage of -50 V and

drain voltage of -40 V. Figure 6.7 shows three different NO_2 concentrations normalized at time = 0 s for comparison. As observed previously, the drain current dramatically increases under NO_2 exposure. However, for the lower NO_2 concentration (0.38 ppm), the current increase is slow and non-linear with time, while for the higher NO_2 concentration, the increase is almost linear. During the third exposure of the device to 1.92 ppm NO_2, the modulation is not linear anymore. It's also interesting to note that the effects of low NO_2 concentration exposure could almost be completely eliminated using N_2 purge, while the higher NO_2 concentrations have a longer recovery time.

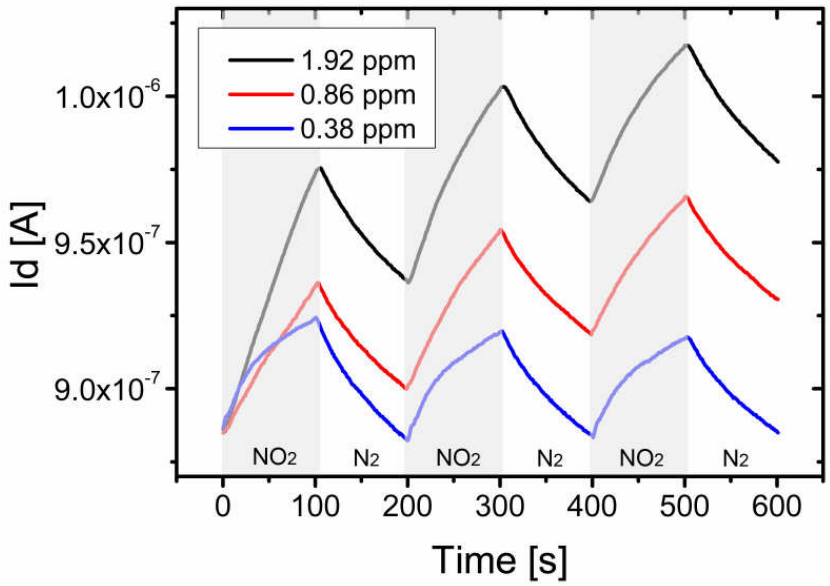

Figure 6.7: Variation of drain current with time on cyclic exposure to NO_2

The rapidity with which the conductivity modulations occur, makes a chemical reaction between the NO_2 gas and the rubrene molecule unlikely. The ability of N_2 purging to revert the rubrene back to its initial state further supports this. Thus the interaction of the NO_2 gas and the rubrene is a pure surface phenomenon associated with the adsorption of the NO_2 molecules on receptive sites. As discussed before, the presence of defects like vacancies and dislocations on the surface of the rubrene crystal could act as receptive centers. The purging of nitrogen removes the NO_2 molecules from the active sites, thus reducing the charge conductivity again. The surface adsorption of NO2 molecules may be enough to enable a

charge transfer between the rubrene surface and the nitrogen dioxide, resulting in charge carrier doping[31].

In summary, we have explored the extrinsic factors that modulate the charge carrier conductivity on the surface of the rubrene crystals. The presence of rubrene peroxide on the surface of the rubrene crystal is strongly indicated and is evidenced by photoluminescence and XPS measurements. In situ surface conductivity measurements during local photo-oxidation have confirmed that the oxidation results in the increase in charge carrier conductivity. The sensitivity of an oxidising gas like NO_2 to the surface conductivity of rubrene single crystals has also been explored, revealing dramatic increases in surface currents on exposure. An important factor to be noted among all these studies is that the factor that modulated the conductivities is the charge carrier concentration and not the mobility values. On the other hand, secondary effects like improvements in the charge injection efficiencies could lead to the conclusion of increased *apparent* charge carrier mobilities.

6.8 References

1. B. A. Gregg, S. G. Chen and H. M. Branz, *Applied Physics Letters*, 2004, **84**, 1707-1709.
2. B. A. Gregg and R. A. Cormier, *Journal of the American Chemical Society*, 2001, **123**, 7959-7960.
3. S. C. Jain, W. Geens, A. Mehra, V. Kumar, T. Aernouts, J. Poortmans, R. Mertens and M. Willander, *Journal of Applied Physics*, 2001, **89**, 3804-3810.
4. B. Maennig, M. Pfeiffer, A. Nollau, X. Zhou, K. Leo and P. Simon, *Physical Review B - Condensed Matter and Materials Physics*, 2001, **64**, 1952081-1952089.
5. M. Pfeiffer, A. Beyer, T. Fritz and K. Leo, *Applied Physics Letters*, 1998, **73**, 3202-3204.
6. M. Pfeiffer, A. Beyer, B. Plo?nnigs, A. Nollau, T. Fritz, K. Leo, D. Schlettwein, S. Hiller and D. Wöhrle, *Solar Energy Materials and Solar Cells*, 2000, **63**, 83-99.
7. P. Leempoel, F. R. F. Fan and A. J. Bard, *Journal of Physical Chemistry*, 1983, **87**, 2948-2955.
8. J. J. Andre, J. Simon, R. Even, B. Boudjema, G. Guillaud and M. Maitrot, *Synthetic Metals*, 1987, **18**, 683-688.
9. D. R. Kearns, G. Tollin and M. Calvin, *The Journal of Chemical Physics*, 1960, **32**, 1020-1025.
10. M. Maitrot, G. Guillaud, B. Boudjema, J. J. Andre and J. Simon, *Journal of Applied Physics*, 1986, **60**, 2396-2400.
11. J. Endo, T. Matsumoto and J. Kido, *Jpn. J. Appl. Phys., Part 2*, 2002, **41**.
12. J. Kido and T. Matsumoto, *Applied Physics Letters*, 1998, **73**, 2866-2868.
13. G. Parthasarathy, C. Shen, A. Kahn and S. R. Forrest, *Journal of Applied Physics*, 2001, **89**, 4986-4992.
14. Y. Yamamoto, K. Yoshino and Y. Inuishi, *Journal of the Physical Society of Japan*, 1979, **47**, 1887-1891.
15. M. F. Calhoun, J. Sanchez, D. Olaya, M. E. Gershenson and V. Podzorov, *Nature Materials*, 2008, **7**, 84-89.
16. T. N. Singh-Rachford and F. N. Castellano, *Journal of Physical Chemistry A*, 2008, **112**, 3550-3556.
17. E. L. Frankevich, M. M. Tribel and I. A. Sokolik, *Physica Status Solidi (B) Basic Research*, 1976, **77**, 265-276.

18. T. Wilson, *Journal of the American Chemical Society*, 1969, **91**, 2387-2388.
19. A. Yildiz, P. T. Kissinger and C. N. Reilley, *The Journal of Chemical Physics*, 1968, **49**, 1403-1406.
20. W. G. Herkstroeter and P. B. Merkel, *Journal of Photochemistry*, 1981, **16**, 331-341.
21. F. Bayrakceken, *Journal of Luminescence*, 1984, **29**, 111-118.
22. O. Mitrofanov, D. V. Lang, C. Kloc, J. M. Wikberg, T. Siegrist, W. So, M. A. Sergent and A. P. Ramirez, *Phys. Rev. Lett.*, 2006, **97**, 166601.
23. O. Mitrofanov, C. Kloc, T. Siegrist, D. V. Lang, W. Y. So and A. P. Ramirez, *Applied Physics Letters*, 2007, **91**.
24. V. Ramamurthy and K. Venkatesan, *Chemical Reviews*, 1987, **87**, 433-481.
25. H. Estrade-szwarckopf, B. Rousseau, C. Herold and P. Lagrange, *Molecular Crystals and Liquid Crystals*, 1998, **310**, 231 - 236.
26. E. Halac, E. Burgos and H. Bonadeo, *Physical Review B*, 1995, **52**, 4764.
27. R. Bertoncello, A. Casagrande, M. Casarin, A. Glisenti, E. Lanzoni, L. Mirenghi and E. Tondello, *Surface and Interface Analysis*, 1992, **18**, 525-531.
28. D. Kafer and G. Witte, *Physical Chemistry Chemical Physics*, 2005, **7**, 2850-2853.
29. C. Krellner, S. Haas, C. Goldmann, K. P. Pernstich, D. J. Gundlach and B. Batlogg, *Physical Review B - Condensed Matter and Materials Physics*, 2007, **75**.
30. E. Menard, A. Marchenko, V. Podzorov, M. E. Gershenson, D. Fichou and J. A. Rogers, *Advanced Materials*, 2006, **18**, 1552-1556.
31. M. Bouvet, *Analytical and Bioanalytical Chemistry*, 2006, **384**, 366-373.

Chapter 6

Conclusions and Perspectives

In this thesis report, the properties of rubrene single crystals have been explored in a variety of ways. Air-gap transistors have been fabricated during this thesis which allows for study of the rubrene single crystal without the influence of the dielectric. The advantages of the air-gap transistors have been used in the exploration of optical charge generation in rubrene single crystals. The excitation of rubrene transistor directly in the channel region has allowed us to explore intrinsic properties.

Rubrene transistors show a strong photocurrent response which is seen as a shift in the threshold voltage on the measurement of transfer characteristics. The steady state measurements of rubrene phototransistors has revealed the presence of persistent photoconductivity caused due to the slow relaxation of charge carriers from oxygen induced traps. Pulsed laser illumination of the rubrene crystal on the other hand revealed details about the dynamics of the photo-injected holes and electrons. A bimolecular recombination of the charge carriers has been observed in these crystals.

In addition to the photocurrent measurements, optical characterization of the rubrene crystal was performed using Photoluminescence and Raman measurements. Exhaustive Raman scattering measurements were performed on the rubrene crystal in a bid to probe the weak intermolecular interactions between the molecules in the crystal. No significant intermolecular coupling was found but additional modes associated with the presence of rubrene peroxide on the surface of the crystal. Photoluminescence measurements of the different facets of the rubrene crystal were used to characterize the different transitions occurring in the molecule and the dependence of the crystal axes on these excitations.

Extrinsic factors that can modify the electrical properties of the rubrene crystal surface were also studied. The presence of rubrene peroxide on the surface of the crystal was confirmed by XPS and photoluminescence measurements. A novel experiment whereby the surface of the rubrene crystal was locally photo-oxidised while monitoring the surface current has revealed that the photo-oxidised areas are more conductive than the original rubrene surface. The photoluminescence measurements indicate the presence of a deep acceptor state that can trap electrons. Thus it can be postulated that the electrical properties of the rubrene surface like high unipolar p-type conductivity and photoconductivity may be significantly modulated by the presence of these oxygen induced states.

The experimental techniques explored in this thesis as well as the results allow for a further exploration of rubrene single crystal transistors. A careful study of persistent photocurrent effects in the rubrene single crystal transistors can be used to study the profile of traps existing on the crystal surface. Since persistent photoconductivity is a general phenomenon, such studies can be extended to organic thin film based transistors as well. The use of the air-gap transistor configuration also allows us to envision a horizontal time-of –flight measurement with the aid of superior laser positioning and fast electronics.

The data regarding the interaction of NO_2 with the rubrene crystal opens the possibility of exploring the interaction between the rubrene semiconductor surface and other types of analytes. The possibility of locally and stably doping the rubrene crystal can lead to the fabrication of pn junctions and pnp transistors. Coupled with recent developments regarding the arrayed growth of organic crystals from the gas and the bulk, it could lead to the practical utilization of these high performance organic crystals.

Publications

‘Steady-state and transient photocurrents in rubrene single crystal free-space dielectric transistors’ N. Mathews, D. Fichou, E. Menard, V. Podzorov, and S. G. Mhaisalkar, Appl. Phys. Lett. 91, 212108 (2007)

‘Transient photocurrent related phenomena in rubrene single crystal transistors’ N. Mathews, D. Fichou, E. Menard, V. Podzorov, and S. G. Mhaisalkar- Under submission

‘Nitrogen Dioxide induced doping in rubrene single crystal field-effect transistors’ Keke Zhang, N. Mathews, Lain-Jong Li, S. G. Mhaisalkar, V. Podzorov and D.Fichou-Under submission

‘UV-Raman measurements on rubrene single crystals’ N. Mathews, S. Tripathi, S.G. Mhaisalkar and D. Fichou- Under preparation